Dissertation

Advanced Diffraction Techniques for Microstructure and Stress Characterisation at Multiple Scales

Mario Stefenelli

Montanuniversität Leoben
Department of Materials Physics

August 2014

Materials Center Leoben Forschung GmbH
Roseggerstraße 12
8700 Leoben
Austria

Affidavit

I declare in lieu of oath, that I wrote this thesis and performed the associated research myself, using only literature cited in this volume.

Leoben, August 2014

Acknowledgements

This work would not have been possible without the great support of co-workers, colleagues from Erich Schmid Institute and Materials Center Leoben, my family and friends. In particular I would like to express my gratitude to the following persons:

- Jozef Keckes, my supervisor, for his guidance through the world of X-ray diffraction. I am grateful for his advices, support and the always open door, that were a great support throughout my Ph.D. His passion for science is really inspiring.
- Angelika Zeilinger and Juraj Todt for countless discussions leading to continuous growth and improvements as well as for the hours we spent watching "X-ray Detector-TV" fun. It was great time we had working together.
- Christian Mitterer and Rostislav Daniel for providing samples and for the kind sharing of their expertise on thin films.
- The staff from the beamlines ID13 (ESRF), P03 and P07 (PETRA III), EDDI (BESSY) and Stress-Spec (FRM II) for providing ideal experimental conditions and their help and support.
- My girlfriend Nora Leodolter for her love and support.

And since the research for this thesis would not have possible without funding:

Financial support by the Austrian Federal Government (in particular from Bundesministerium für Verkehr, Innovation und Technologie and Bundesministerium für Wissenschaft, Forschung und Wirtschaft) represented by Österreichische Forschungsförderungsgesellschaft mbH and the Styrian and the Tyrolean Provincial Government, represented by Steirische Wirtschaftsförderungsgesellschaft mbH and Standortagentur Tirol, within the framework of the COMET Funding Programme is gratefully acknowledged.

Abstract

Mechanical integrity, functional properties and lifetime of engineering components are predetermined by the residual stress state and structural properties of the applied materials. Nowadays, the development of novel materials with tailored functionality requires a detailed knowledge of their structural and mechanical properties at the centimetre down to the nanometre length-scales. For this reason, advanced analytical techniques allowing volume-averaged as well as very local characterisation of phases, residual stresses and microstructure have to be applied to reveal the complex mutli-scale structure-function relationships in technological materials.

In this thesis, advanced high-energy X-ray and neutron diffraction techniques operating at various scales are presented and used to analyse three types of structures, nanocrystalline thin films, seamless steel tubes and railway rails, applying always the appropriate spatial resolution.

(i) Nanocrystalline thin films are characterised using cross-sectional X-ray nanodiffraction with a spatial resolution as low as 100 nm. In the first study the residual stress gradient in a shot-peened 11.5 µm thick TiN film is characterised and the results are compared to a Laplace space approach characterisation. Additionally the effect of stress relaxation in the thin lamella required as a sample for the nanobeam experiments is addressed. In the second study the residual stress fields across the imprint in a wedge-indented 3 µm CrN-Cr multilayer film are characterised. The results reveal a complex residual stress distribution across the film cross-section with stress peaks ranging from −10 to 2 GPa being in good agreement with a finite element model. It is shown how the ductile Cr sublayers act as a stabilizing component preserving the mechanical integrity of the structure by the encapsulation of the regions with tensile stress peaks in the brittle CrN sublayers. In the third study the fracture properties of 3 µm CrN thin films are examined by coupling four-point bending and energy dispersive X-ray diffraction. Two thin film types, deposited by applying −40 V and −120 V bias voltage, are compared in the as-deposited and annealed state. It is found that the change in the bias voltage modified the observed fracture behaviour in favour for the −120 V film, which however deteriorates upon

annealing, whereas the $-40\,\mathrm{V}$ film is not affected by the heat treatment.

(ii) The residual stress distribution inside a roller-straightened railway rail is characterised with neutron diffraction using a gauge volume of $5 \times 5 \times 5\,\mathrm{mm}^3$. The longitudinal, vertical and transversal components of the stress tensor are determined and compared with the results from the contour method and finite element modelling.

(iii) Three dimensional distributions of triaxial residual stress in seamless steel tubes are studied by high energy synchrotron X-ray diffraction coupled with a conical slit system providing a spatial resolution along the X-ray beam of $0.8\,\mathrm{mm}$. The identified steep residual gradients across the tube walls are correlated with applied cooling conditions and the resulting microstructure.

Kurzfassung

Strukturelle Integrität, funktionelle Eigenschaften und Lebensdauer technischer Bauteile werden durch Eigenspannungen und Mikrostruktur der verwendeten Materialien bestimmt. Für die Entwicklung neuartiger Materialien mit zielgerichteten Eigenschaften bedarf es oftmals eines detaillierten Wissens über deren strukturelle und mechanische Eigenschaften auf Zentimeter- bis Nanometerebene. Daher bedarf es Analysetechniken zur Bestimmung von Phasen, Eigenspannungen und Mikrostruktur auf globaler, aber auch sehr lokaler Ebene um die komplexen, über mehrere Größenordnungen reichenden Struktur-Eigenschafts-Beziehungen moderner Werkstoffe zu bestimmen zu können.

Im Rahmen dieser Arbeit werden hochentwickelte Techniken der Hochenergie-Röntgen- und Neutronenbeugung mit unterschiedlicher Ortsauflösung vorgestellt und damit drei verschiedene Strukturen, nanokristalline dünne Schichten, nahtlose Stahlrohre und Eisenbahnschienen, mit entsprechender Auflösung charakterisiert.

(i) Nanokristalline dünne Schichten werden mittels Röntgen-Nanobeugung, deren Ortsauflösung bei 100 nm liegt, untersucht. In der ersten Studie werden Eigenspannungsgradienten in einer kugelbestrahlten 11,5 µm dicken TiN Schicht bestimmt und die Ergebnisse mit denen einer Laplace-Methode verglichen. Zusätzlich wird die Relaxation von Spannungen in der als Probe verwendeten Lamelle thematisiert. In der zweiten Studie werden die Eigenspannungen in einer CrN-Cr Multilagenschicht mit einem Wedge-Eindruck bestimmt. Das Ergebnis zeigt, in guter Übereinstimmung mit einem Finite-Elemente-Model, eine komplexe Spannungsverteilung über den Lamellenquerschnitt mit Spitzenwerten von −10 bis 2 GPa. Es wird dargelegt, wie die Integrität der Struktur durch Einschluss der Zugspannungsspitzen in den CrN Schichten zwischen den Cr Schichten gewahrt bleibt. In der dritten Studie werden Brucheigenschaften von 3 µm dicken CrN Schichten mittels Vier-Punkt-Biegung kombiniert mit energiedispersiver Röntgenbeugung bestimmt. Zwei Schichttypen, abgeschieden bei −120 V und −40 V Bias-Spannung, werden im abgeschiedenen und geglühten Zustand verglichen. Die beobachteten Brucheigenschaften verbessern sich durch Änderung der Bias-Spannung zugunsten der −120 V Schicht. Diese verschlech-

tern sich allerdings durch die Glühbehandlung, während jene der $-40\,\mathrm{V}$ Schicht unverändert bleiben.

(ii) Der Eigenspannungszustand in einer rollen-gerichteten Eisenbahnschiene wird mittels Neutronenbeugung mit einem Messvolumen von $5 \times 5 \times 5\,\mathrm{mm}^3$ charakterisiert. Die longitudinalen, vertikalen und transversalen Komponenten des Spannungstensors werden ermittelt und mit den Ergebnissen der Konturmethode und eines Finite-Elemente-Modells verglichen

(iii) In nahtlosen Stahlrohren wird die dreidimensionale Verteilung des triaxialen Eigenspannungszustandes mit hochenergetischer Synchronrotstrahlung in Verbindung mit einer konischen Blende bei einer Ortsauflösung von $0{,}8\,\mathrm{mm}$ untersucht. Die ermittelten, starken Spannungsgradienten in den Rohrwänden werden mit den angewandten Abkühlbedingungen und der daraus resultierenden Mikrostruktur korreliert.

Contents

1 Introduction

Materials used in modern engineering components usually exhibit complex gradients of phases, grain sizes, residual stresses and texture, which have a decisive influence on their functional properties, mechanical integrity and lifetime. In order to enhance the lifetime and service performance by an improved materials design, it is crucial to understand how manufacturing and service influence these gradients. This is only possible by using analytical techniques allowing for a local characterisation with a spatial resolution ranging from centimetres down to the nanometre regime – depending on the size of the studied structure. Diffraction techniques, here especially high energy synchrotron X-ray diffraction combined with an area detector, allow to determine representative properties like phases, grain sizes, residual stresses and texture information for relatively small gauge volumes. With modern focussing techniques it is possible to tailor X-ray beams with sizes down to 100 nm [1–4], that can be used to locally characterise small structures like thin films or microelectronic components. In the case of larger structures the photon high energies available at modern synchrotron sources [5] are sufficient to penetrate a few centimetres of steel, while still maintaining a relatively high spatial resolution. Very large structures such as rails can be characterised using neutron diffraction, which offers the largest penetration depths [5].

Within this thesis three types of structures, namely thin films, seamless steel tubes

and railway rails, are characterised by applying appropriate experimental approaches with a spatial resolution in the range from 5 to 10^{-4} mm. The experimental results on microstructure and residual stress provided by different experimental techniques are correlated with the production parameters and/or specific sample preparation conditions. A special focus is laid on cross-sectional X-ray nanodiffraction [6] as this is a new, very promising method offering a wide range of applications. A new method for efficient data treatment allowing to process a large number of diffraction images from high resolution, two-dimensional scans or in-situ experiments is presented, as this is a prerequisite to couple X-ray nanodiffraction with indentation experiments. New approaches for the quantitative evaluation of residual stress and texture from a singe diffraction image are proposed.

In this chapter the diffraction methods applied in the appended publications are briefly introduced and discussed.

1.1. X-ray Nanodiffraction Analysis of Residual Stresses in Thin Films

Cross-sectional X-ray nanodiffraction as introduced by Keckes et al. [6] is a versatile tool, which enables to locally characterise nanocrystalline materials with a spatial resolution down to 100 nm. The approach can be used to map the cross-sectional distributions of phases, crystallite sizes, stresses and crystallographic texture in thin films, where all the information can be retrieved from a set of two dimensional diffraction patterns collected in transmission geometry across the film cross-section. The technique has thus led to a range of new insights in the structure-property relationships of nanocrystalline thin films [7–10]. Especially the characterisation of stress gradients provides an important contribution to the understanding of structure-property relationships in thin films, when correlating functional properties and lifetime with applied deposition recipes, actual film architectures and/or post deposition treatments such as annealing or blasting. The characterisation of the local stress gradients is a prerequisite to identify and understand failure mechanisms in mechanically loaded thin films (*cf.* Paper B). Therefore in this thesis the focus was laid on the improvement of characterisation techniques for complex stress distributions across thin films.

A vital step to achieve this goal was to improve the workflow of synchrotron data treatment. As smaller beam sizes allow for even higher spatial resolution and new, more complex experiments demand not just a simple line profiling but two-

dimensional (2D) scanning of the sample at the cross-section (*cf.* Paper B), large amounts of diffraction data are produced, that need to be evaluated and stored efficiently. This is even more the case if synchrotron experiments are performed in-situ when large amounts of data are collected repeatedly. The processing of the diffraction data using the standard Fit2D software package [11] could not fulfil those demands, especially in the case of 2D mapping (*cf.* Paper B) and in-situ experiments [12]. Therefore a new workflow using the recently developed PyFAI package [13, 14] for integration and the Hierarchical Data Format HDF5 [15] for data storage was implemented.

1.1.1. Experimental Setup

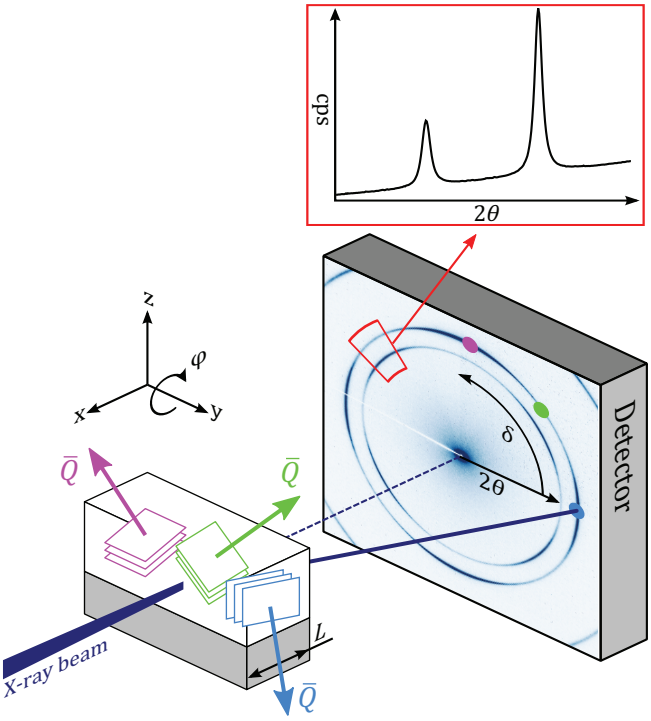

Figure 1.1.: A schematic description of the cross-sectional X-ray nanodiffraction setup. The sample with the thickness L is analysed with a nanofocused X-ray beam in transmission geometry. The diffraction of the beam on the crystallographic lattice planes (hkl) results in the formation of characteristic Debye-Scherrer rings on the 2D detector. Every diffraction spot described by the diffraction angle 2θ and the azimuthal angle δ corresponds to a specific set of lattice planes, which orientation is given by the diffraction vector $\bar{Q}$, as indicated here exemplary through different colours.

The principal layout and geometric relationships of the experimental setup with the corresponding variables and conventions as described in [6, 10] are recapitulated hereafter. For the details the reader is referred to the respective publications as they are specific to the individual experiments.

Fig 1.1 depicts the schematic setup of the cross-sectional X-ray nanodiffraction experiment. As a sample, a thin lamella with the thickness of $L = 10 - 100\,\mu m$ is used, which is analysed by the nanofocused X-ray beam in transmission geometry. The beam is diffracted by the crystallographic lattice planes (hkl) of the sample material according to Bragg's law resulting in Debye-Scherrer rings on the detector. The position of each detector pixel with the recorded intensity $I(\theta, \delta)$ is specified by the diffraction angle 2θ and the azimuthal angle δ and corresponds to a specific diffraction vector $\bar{Q}$, being the normal on the diffracting lattice planes. This is exemplary indicated through different colours in Fig 1.1.

For the alignment and during the position-resolved experiments, the sample is moved along the y or z-axis using piezo cubes by a simultaneous collecting of diffraction data using the 2D detector.

At present such experiments can be performed at the nanofocus extensions of the ID13 beamline at the ESRF in Grenoble, France [16] and the P03 beamline at PETRA III of DESY, Germany [17].

1.1.2. Data Treatment

For a long time the software package Fit2D [11] has been a well-recognized standard used for the treatment of 2D diffraction data in order to obtain a series of powder patters $I_\delta(\theta)$ which can be then used for quantitative diffraction analysis. However the scripting capabilities of Fit2D are quite limited and the only way of data output is generating a text file for every powder diffraction pattern $I_\delta(\theta)$. These drawbacks make the data treatment for high resolution scans very difficult, as there is a large number of frames that needs to be integrated. The mesh scan in Paper B for example consists of 7171 2D detector images with a resolution 2048×2048 pixels each. A recently developed alternative that overcomes these limitations is PyFAI [13, 14], which is an open source Python library for azimuthal integration of 2D diffraction data. Its great advantage is, that it can be implemented in any Python code thus all features of Python can be used for pre- and post-integration data treatment. For the storage of the integrated powder patters, the Hierarchical Data Format HDF5 [15] was chosen as it is was designed to store large amounts of data. Additionally it can be directly accessed from Python, offers good connectivity to other software

packages, is platform independent and offers the possibility of data compression.

A Graphical User Interface for PyFAI

As PyFAI is designed as a library for Python it has no native graphical user interface (GUI). There are some scripts and a GUI that come with the distribution but their usability for evaluating large amounts of X-ray data is limited. Therefore a GUI dedicated to the evaluation of X-ray nanobeam experiments was set up within this thesis. The major goals were (i) to optimise the workflow for the evaluation of line (1D) and mesh scans (2D) and (ii) to standardise the data structures for saving to integrated data in HDF5.

The GUI was designed using PyQt4 [18] and the packages *guiqwt* [19] and *matplotlib* [20] were used to display the data. In Fig. 1.2 the "Integration" interface of the GUI is presented, where all necessary parameters for the integration can be set. However for a better usability not all options of the PyFAI library were implemented. The selected files can be either integrated as a "Powder Pattern" or for "Texture", where the number of radial points is set to 1 in order to generate intensity profiles of one peak in azimuthal direction. The list of files in the "Files" section can be processed in three different ways:

Single Frame: Here only one selected frame specified in the "Frame" field is integrated. This is mainly for preview purposes and no data is stored.

File Series: Here all files listed in the "Files" section are processed in the displayed order and stored as one dataset in the HDF5 file. The integrated data can be displayed in one coloured 2D plot.

Mesh: Here the whole sequence of the listed files, usually from a 2D mesh scan, is divided into sections by the number set in the "Frames per line" field. The data of each line is stored in an individual dataset, where each can be displayed as a coloured 2D plot. There is also an option to show these plots sequentially.

In Fig. 1.3 an exemplary evaluation of one diffraction image taken from the TiN thin film of Paper A is presented. The diffraction image (a) is analysed in the given 2θ-range and the TiN 111 and 200 peaks are presented in the powder pattern (b). From varying intensities in azimuthal direction (c) the presence of a texture can be deduced. In the "Display Data" tab the results of the integration can be directly displayed in 2D colour plots. The integrated data and the necessary information to reproduce the integration are stored in a HDF5 file, which consists of the following datasets:

cakes: Is a 2D array containing the upper and lower bounds of the cakes.

frames: Is a 1D array containing the path and file name of each frame processed.

line: Is a 2D array where the actual integration results are stored. It has a special data type, where each cell contains two 1D arrays, one with the 2θ-values and one with the intensities. The data are ordered in such way, that all cakes of a frame are stored in one row. If a "Mesh" evaluation is performed one such dataset is generated for every line. In this case the name is extended by a three digit number.

parameters: is a 2D array with all parameters necessary to reproduce the evaluation.

poni_file: Here the calibration is saved as a text file.

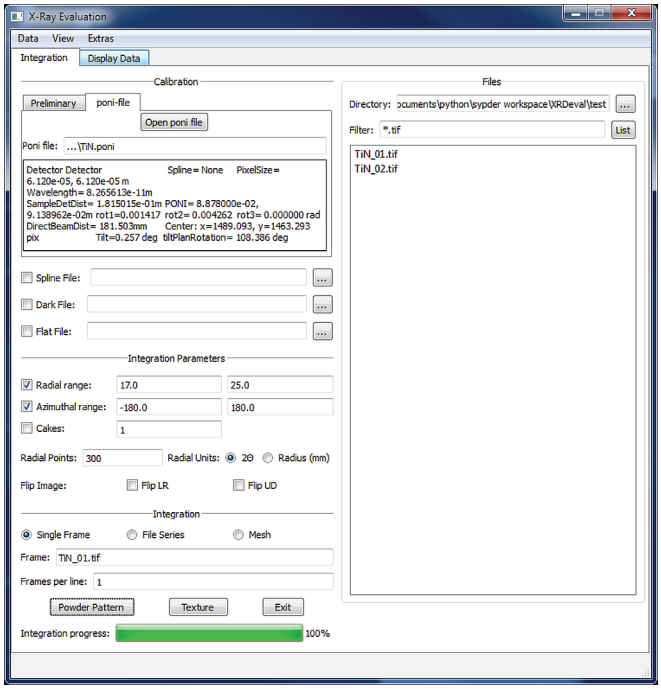

Figure 1.2.: The "Integration" interface of the GUI, where all relevant settings for integration can be made. The settings are made in order to integrate the data for Fig. 1.3.

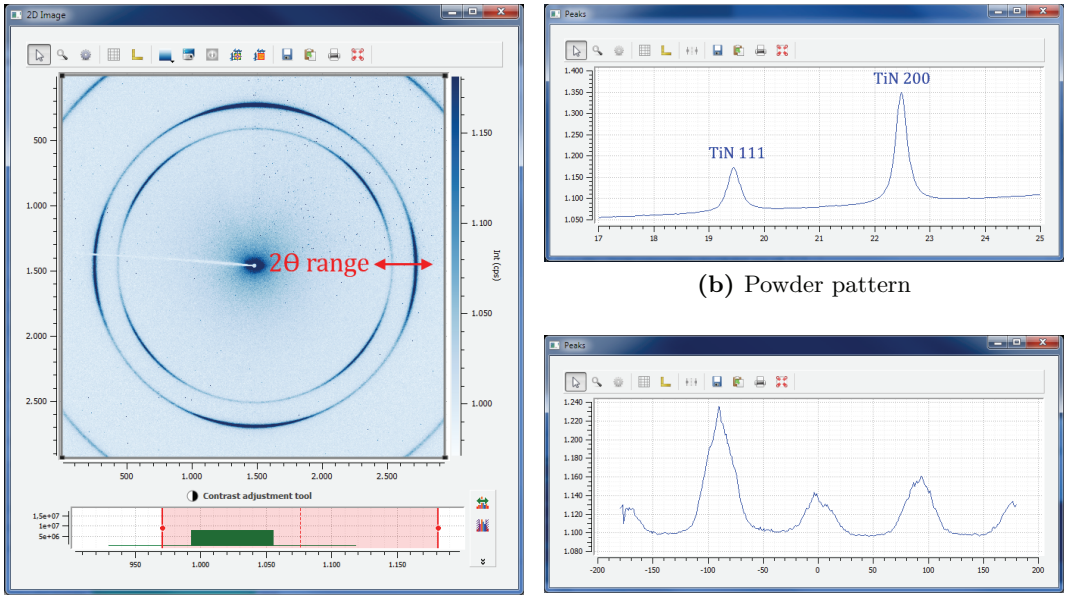

(a) Analysed frame

(b) Powder pattern

(c) Azimuthal intensity distribution

Figure 1.3.: An exemplary evaluation of the diffraction pattern (a) from a TiN thin film. The powder pattern (b) with 111 and 200 peaks represents intensity distribution as a function of Bragg's angle 2θ along the red arrow in (a). The azimuthal intensity distribution along the 200 Debye-Scherrer ring, which comprise crystallographic texture information (*cf.* Paper A) is shown in (c).

1.1.3. Residual Stress Evaluation

The presence of stress in the diffracting gauge volume element causes an elliptical distortion of the Debye-Scherrer rings [21]. If the unstrained lattice parameter D_0^{hkl} of the material is known, the elastic strain as a function δ can be directly determined according to Eq. (1.1). As D_0^{hkl} is not known exactly in general other approaches have been developed to determine stress from X-ray diffraction experiments, with the most common being probably the $\sin^2\psi$–approach [22, 23]. Under the condition of the plane stress (i. e. $\sigma_z \approxeq 0$) it allows to determine stress without the exact knowledge of D_0^{hkl}. In order to evaluate stress from the 2D diffraction data the azimuthal angle δ needs to be converted into ψ which can be done using the transformation proposed by Heidelbach et. al [24].

$$\varepsilon^{hkl}(\delta) = \frac{D^{hkl}(\delta) - D_0^{hkl}}{D_0^{hkl}} \tag{1.1}$$

It is however possible to establish a direct relationship between the measured strain component $(\varepsilon'_{22})^{hkl}_{\theta,\delta}$ in the direction of the diffraction vector $\bar{Q}$ (*cf.* Fig. 1.1)

and the strain tensor in the sample. This can be achieved by means of tensor algebra applying the same approach as for the $\sin^2\psi$–method [22, 23]. Therefore the strain tensor in the sample coordinate system $S(x', y', z')$, where $\bar{Q} = y'$ needs to be transformed into the laboratory coordinate system $L(x, y, z)$. The transformation between these two systems is a two-fold rotation of θ around the z-axis and δ around the x-axis as shown in Fig. 1.4. This can be described by the transformation matrix A as given in Eq. (1.2).

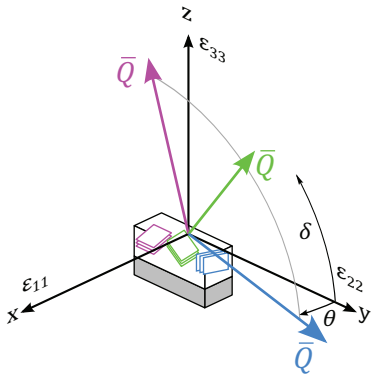

Figure 1.4.: In order to link the measured strain component $(\varepsilon'_{22})^{hkl}_{\theta,\delta}$ in the direction of $\bar{Q} = y'$ with the strain tensor in the sample coordinate system coordinate system ε^{hkl}, a tensor transformation based on the relationship between the sample coordinate system $S(x', y', z')$ and the laboratory coordinate system $L(x, y, z)$, being a two-fold rotation of θ around the z-axis and δ around the x-axis, leading to the transformation matrix A given in Eq. (1.2), has to be applied.

$$A = \begin{bmatrix} \cos\theta & \cos\delta\sin\theta & -\sin\delta\sin\theta \\ -\sin\theta & \cos\delta\cos\theta & -\cos\theta\sin\delta \\ 0 & \sin\delta & \cos\delta \end{bmatrix} \tag{1.2}$$

Now the tensor transformation between $(\varepsilon'_{22})^{hkl}_{\theta,\delta}$ and the strain tensor in the sample coordinate system ε^{hkl} according to Eq. (1.3), gives the relationship between the measured strain along $\bar{Q}$ and the unknown strain in the sample coordinate system as in Eq. (1.4).

$$(\varepsilon'_{22})^{hkl}_{\theta,\delta} = \frac{D^{hkl}_{\theta,\delta} - D^{hkl}_0}{D^{hkl}_0} = a_{2i}a_{2j}\varepsilon^{hkl}_{ij} \tag{1.3}$$

$$\begin{aligned}(\varepsilon'_{22})^{hkl}_{\theta,\delta} &= \sin^2\theta\,\varepsilon^{hkl}_{11} - 2\cos\delta\cos\theta\sin\theta\,\varepsilon^{hkl}_{12} \\ &+ \cos^2\delta\cos^2\theta\,\varepsilon^{hkl}_{22} + \cos^2\theta\sin^2\delta\,\varepsilon^{hkl}_{33} \\ &+ 2\cos\theta\sin\delta\sin\theta\,\varepsilon^{hkl}_{13} - 2\cos\delta\cos^2\theta\sin\delta\,\varepsilon^{hkl}_{23} \end{aligned} \tag{1.4}$$

Biaxial Case

In the case of only σ_{11} and σ_{22} being present in the sample and all other components being either zero or negligible Eq. (1.4) can be simplified and rewritten as follows (*cf.* Paper A):

$$\begin{aligned}(\varepsilon'_{22})^{hkl}_{\theta,\delta} &= \sigma_{11}\left[\tfrac{1}{2}S^{hkl}_2\sin^2\theta + S^{hkl}_1\right] \\ &+ \sigma_{22}\left[\tfrac{1}{2}S^{hkl}_2\cos^2\delta\cos^2\theta + S^{hkl}_1\right] \end{aligned} \tag{1.5}$$

where S^{hkl}_1 and $\frac{1}{2}S^{hkl}_2$ are the materials X-ray elastic constants. If a new azimuthal angle $\gamma = \delta - 90°$ is introduced Eq. (1.5) can then be simplified and transformed to directly determine σ_{22} from the slope of the D vs. $\sin^2\gamma$ dependencies (Eq. (1.6)). Here it is assumed that for small Bragg angles $\cos^2\theta \approxeq 1$. The unstrained lattice parameter D^{hkl}_0 can be determined from $(D^*)^{hkl}$ at the strain free direction $\sin^2\gamma^*$ [23].

$$\frac{\partial D_{\theta,\gamma}}{\partial\sin^2\gamma} = \sigma_{22}\,\tfrac{1}{2}S^{hkl}_2\,D^{hkl}_0 \tag{1.6}$$

General Case

In the case of a more complex stress state, Eq. (1.4) can be rewritten to become Eq. (1.7) containing all six components of the stress tensor and completely describing the distorted diffraction ring. The influence of the individual stress components on the diffraction ring distortion is shown in Fig. 1.3.

$$\begin{aligned}(\varepsilon'_{22})^{hkl}_{\theta,\delta} &= \sigma_{11}\left[\tfrac{1}{2}S^{hkl}_2\sin^2\theta + S^{hkl}_1\right] \\ &+ \sigma_{22}\left[\tfrac{1}{2}S^{hkl}_2\cos^2\delta\cos^2\theta + S^{hkl}_1\right] \\ &+ \sigma_{33}\left[\tfrac{1}{2}S^{hkl}_2\cos^2\theta\sin^2\delta + S^{hkl}_1\right] \\ &- \sigma_{12}\left[S^{hkl}_2\cos\delta\cos\theta\sin\theta\right] \\ &+ \sigma_{13}\left[S^{hkl}_2\cos\theta\sin\delta\sin\theta\right] \\ &- \sigma_{23}\left[S^{hkl}_2\cos\delta\cos^2\theta\sin\delta\right] \end{aligned} \tag{1.7}$$

Under the condition that there are data from at least two different peaks available, it is possible to determine all six components of the stress tensor from Eq. (1.7). This is archived by generating a system of equations holding the data from all measured peaks which can be solved for σ_{ii} and σ_{ij}. For this approach it is however necessary to have a correct value for the unstrained lattice parameter D_0^{hkl} as it is required to determine $(\varepsilon'_{22})_{\theta,\delta}^{hkl}$ from the diffraction data according to Eq. (1.1). The requirement of having data from at least two different peaks originates from the fact, that the influence of σ_{11} on the deformation of the diffraction ring does not depend on δ but merely acts as a linear offset to the curve, as it can be seen in Fig. 1.3 a. Therefore, if diffraction data from only one peak are available, the problem becomes ill-conditioned resulting in incorrect results for the σ_{ii} components. If the data from only one peak is to be evaluated, it is also possible to fit Eq. (1.7) to the $(\varepsilon'_{22})_{\theta,\delta}^{hkl}$ data, but in this case σ_{11} needs to be determined by other means and given as an input parameter.

Care should also be taken in the interpretation of the shear components as their effect on the distortion of the Debye-Scherrer rings is equivalent to the effects of an error in the calibration of the beam centre or the detector tilt.

In the case of a plane stress state any result for σ_{33} in the solution of Eq. (1.7) can be interpreted as a pseudo hydrostatic stress σ_{ph} originating in a incorrect value used for D_0^{hkl}. Therefore changing D_0^{hkl} until σ_{ph} becomes zero in an iterative process can be used to refine D_0^{hkl} [21, 25].

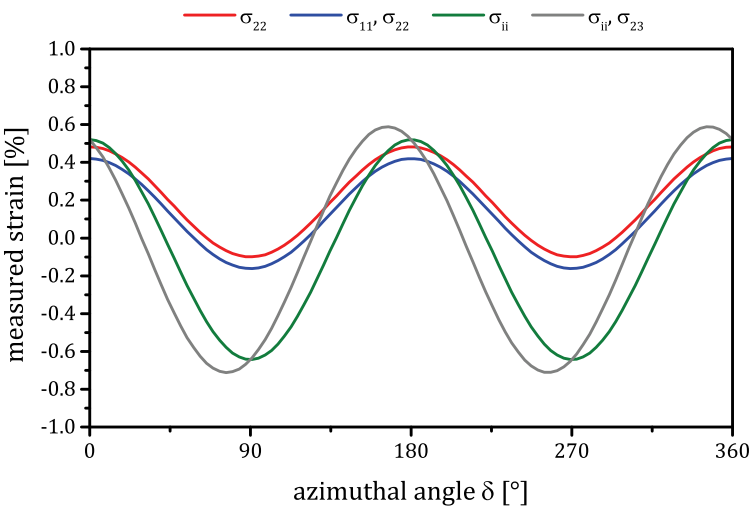

(a)

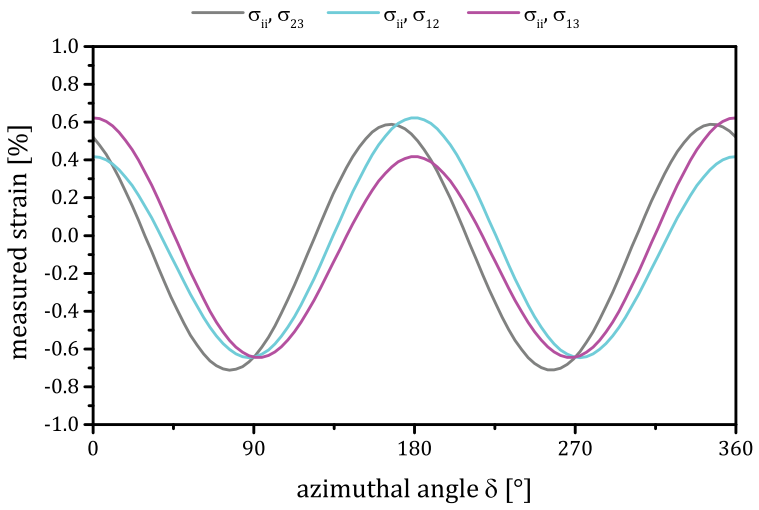

(b)

Figure 1.3.: Measured strain $(\varepsilon'_{22})_{\theta,\delta}$ plotted as a function of the azimuthal angle δ. Six loading cases with different stress components present demonstrate the effect of the individual components on the deformation of the Debye-Scherrer ring. The principal components σ_{ii} scale the amplitude of the wave and the shear components σ_{ij} alter the wavelength (a). Additionally the in-plane shear components σ_{1i} induce a non-uniform amplitude (b).

1.1.4. Relaxation of Stresses due to Sample Preparation

When a thin lamella with the thickness L is cut from the sample the stress component σ_{11} can relax due to the expansion of the film in x-direction, as shown in Fig. 1.4. Depending on the ratio between L and the film thickness D and the stiffness of the substrate material, three cases can be distinguished:

L $\gg$ D: The volume fraction with a relaxed σ_{11} is very small and the effect can be neglected.

L $\approxeq$ D, soft substrate: This will cause a constant relaxation across the thin film, i.e. $\Delta\sigma_{11} = \text{constant}$.

L $\approxeq$ D, stiff substrate: In this case there will be a depth dependent expansion of the film in x-direction, as the substrate will confine the thin film on the interface.

For the last case in Paper A finite element modelling (FEM) has been applied to assess the effect of the relaxation of σ_{11} on σ_{22} obtained from the X-ray diffraction data evaluation. It is found that for $L \approxeq D$ the effect is significant and needs to be accounted for. Therefore in Paper A a procedure is proposed that allows for the

recursive evaluation of the original equi-biaxial stress state in the sample from the measured data of partly relaxed sample.

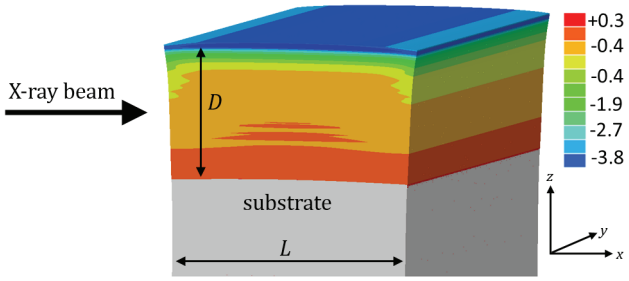

Figure 1.4.: A FEM model documents the relaxation of the stress component σ_{11} due to the expansion of the lamella in x-direction. One can observe that the relaxation is almost 0 at the interface and increases towards the surface (*cf.* Paper A).

1.1.5. Summary and Outlook

In Paper A the residual stress gradient in a shot-peened nanocrystalline TiN film is mapped using cross-sectional X-ray nanodiffraction and the results are compared with a Laplace space approach. It is shown that the residual stresses evaluated using Eq. (1.6) and corrected as described in section 1.1.4 are in agreement with the results from the Laplace space approach characterisation. This proves that the assumptions required to apply Eq. (1.6) are justified in this case.

In Paper B the residual stress distribution in a wedge-indented nanocrystalline CrN-Cr thin film with a respective layer thickness of 500 nm and 250 nm is characterised using cross-sectional synchrotron X-ray nanodiffraction with a spatial resolution of 100 nm. At present this is the first experiment revealing a complex distribution of tensile and compressive residual stresses across the imprint. With the aid of FEM the formation of these stresses is explained and it is shown how the soft Cr sublayers acts as a stabilising component preserving the integrity of the structure during the indentation.

For the future three major trends can be expected:

(i) Experiments to characterise the stress distribution under an indenter in-situ have already been conducted and the results will be presented in future publications [12]. For these complex load cases the ability to evaluate the full stress tensor will add a new quality to the results, as in this case the assumption of plane stress does not hold true any more and shear stresses appear to play an important role in the deformation and failure behaviour. The possibility to study the effects taking place within a thin film under mechanical load will provide new insights into the deform-

ation and failure mechanisms of thin films and lead way to improve the architecture of nanocomposites.

(ii) Recently developed Multilayer Laue Lenses (MLLs) [4] are promising to become the next quantum leap in reducing beams sizes and improving spatial resolution. Within an application test the CrN-Cr multilayer film from Paper B was characterised by Dr. Sven Niese, Fraunhofer IKTS-MD, Dresden at the ID13 beamline of ESRF in Grenoble, France [16] archiving a spatial resolution of 50 nm. The phase plot evaluated from the diffraction data is depicted in Fig 1.5. The large overlapping of the CrN and Cr phases can be attributed to the interfaces not being aligned parallel to the x-y-plane.

(iii) The concept of cross-sectional X-ray diffraction is not limited to nanodiffraction and nanocrystalline materials but has already been successfully applied to characterise the near surface region of nitrided Fe alloys with the resolution and beam-sizes in the micrometer range [26].

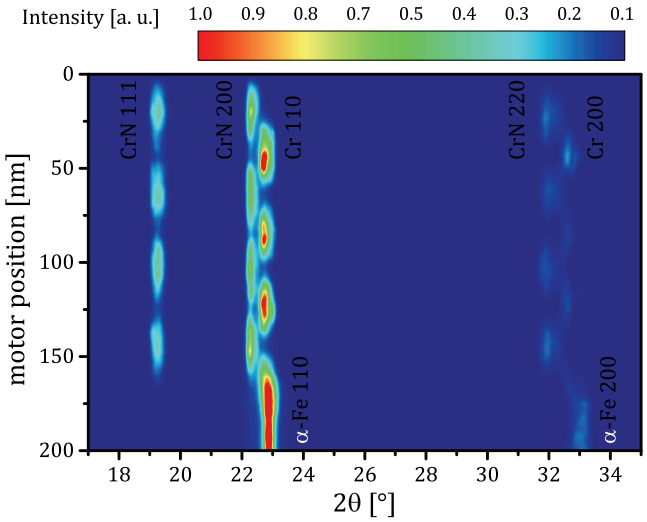

Figure 1.5.: Application test of newly developed MLLs, where the CrN-Cr multilayer film from Paper B was scanned at ID13 with a beamsize of 50 nm.

1.2. Texture Evaluation using the MTEX Software Package

Crystallographic texture, the preferred orientation of crystallites in the material, decisively influences physical properties of materials. Since most crystalline materials are not isotropic, i. e. the crystal exhibits different physical properties along various crystallographic directions, the presence of texture results in the macroscopic anisotropy of physical properties. Therefore the ability to understand the relationship

between production parameters and final material texture is crucial for the design of new materials with controlled anisotropy, i. e. properties [7, 27–30]. Furthermore the knowledge about texture is also an important input parameter for the evaluation of other characteristics such as residual stresses (*cf.* Paper A) [31].

Texture evaluation in a tensely loaded sample during an in-situ experiment allows to study deformation mechanisms such as reorientation of grains or twinning [32–34], which play in important role in defining the nature of the elasto-plastic material response.

Therefore it is important to have tools ready that (i) allow local characterisation of texture with high spatial resolution and (ii) can efficiently evaluate texture from a large number of measurements. The first criterion is particularly important for materials with small dimensions such as nanocrystalline thin films and can be met using the X-ray nanodiffraction technique described in section 1.1. The second criterion can be satisfied by using MTEX [35], which is a Matlab toolbox allowing to directly quantify the orientation distribution function (ODF) from a single 2D X-ray diffraction image [36].

1.2.1. Construction of Raw Pole Figures from 2D Diffraction Data

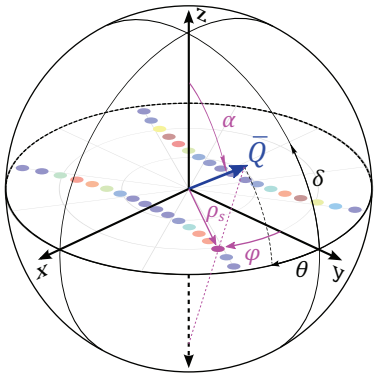

Figure 1.6.: Coordinate system and angles used to describe the position of the diffraction vector $\bar{Q}(\theta, \delta)$, where θ is the Bragg angle and δ is the azimuthal angle on the diffraction image. To plot $\bar{Q}(\theta, \delta)$ into a stereographic projection, θ and δ are converted into ρ_s and φ using Eqs. (1.8) to (1.11). In the x, y-plane the raw pole figure of the TiN 111 reflection is shown, where the lower half of the Debye-Scherrer ring ($\delta = [180°, 360°]$) is projected to the southern hemisphere of the pole figure ($\varphi = [180°, 360°]$). For a better illustration θ was scaled by a factor of 3.

To perform the ODF estimation with MTEX, raw pole figures need to be constructed from the 2D diffraction data as shown in Fig. 1.6 [21]. This is done in three

consecutive steps.

First the 2D diffraction images are integrated for "Texture" as described in section 1.1.2 obtaining datasets of the form $(\theta\ \delta\ I)^{hkl}$ for each reflection hkl. Alternatively the 2D patterns can be integrated cake-wise (*cf.* section 1.1.2) with subsequent fitting of the diffraction peaks hkl of interest. The diffraction vectors $\bar{Q}(\theta, \delta)$ corresponding to each dataset are defined as follows:

$$\bar{Q}(\theta, \delta) = \begin{bmatrix} \sin\theta \\ \cos\theta\cos\delta \\ \cos\theta\sin\delta \end{bmatrix}. \tag{1.8}$$

Second, the $\bar{Q}(\theta, \delta)$ are converted into spherical coordinates $\bar{Q}(\alpha, \varphi)$ using Eqs. (1.9) and (1.10), where α is the inclination angle with the positive z-axis and φ the azimuthal angle in the x-y-plane.

$$\alpha = \arctan\left(\frac{r}{\bar{Q}_z}\right) \tag{1.9}$$

$$\varphi = \arccos\left(\frac{\bar{Q}_y}{r}\right) \quad \text{with } r = \sqrt{\bar{Q}_x{}^2 + \bar{Q}_y{}^2} \tag{1.10}$$

In in the third step the data for each hkl are plotted in a stereographic projection as shown in Fig. 1.6. Thereto the polar angle ρ_s needs to be calculated according to Eq. (1.11) and the data of the the lower half of the Debye-Scherrer ring ($\delta = [180°, 360°]$) are projected to the southern hemisphere of the pole figure ($\varphi = [180°, 360°]$). The new dataset $(\rho_s\ \varphi\ I)^{hkl}$ can now be imported by MTEX as a raw pole figure for the respective reflection (*cf.* Fig. 1.7 a, b).

$$\rho_s = \tan\left(\frac{\alpha}{2}\right) \cdot 90° \tag{1.11}$$

1.2.2. Texture Analysis of a Nanocrystalline TiN Thin Film

Nanocrystalline thin films often exhibit pronounced textures due to competitive columnar grain evolution during the film growth [27, 37, 38]. Texture gradients across the thickness or its local variations are usually attributable to the changes in conditions during the film growth [6–9, 39], to template effects [27, 40] or to self-organization phenomena. Making use of these effects allows to synthesise thin films or nanocomposites with superior physical properties.

Up to now texture of nanocrystalline thin films has been mostly characterised as a volume averaged property and only few studies (e. g. [6, 9] and Paper A) report results on texture variation across the film thickness. But also here the ODF were only evaluated at selected positions or the texture was deduced indirectly.

The aim of using MTEX to calculate ODF from X-ray nanodiffraction data is to implement it as a method to process a large number of diffraction images, in order to produce texture maps or study texture evolution in-situ.

In this section the combination of cross-sectional X-ray nanodiffraction and MTEX is tested on a diffraction image of the TiN film from Paper A, which exhibits a pronounced {100} fibre texture. The results are compared to Rietveld evaluation with MAUD [41] and laboratory measurements using a Rigaku SmartLab.

The diffraction image used for the ODF analysis is shown in Fig. 1.7 a. Here the presence of the texture is already clearly visible from the varying intensity distribution along the diffraction ring. The corresponding raw pole figures for the 111 and 200 reflection are shown in Fig. 1.7 b and c respectively. In Fig. 1.8 the recalculated pole figures for the 111 and 200 reflection produced using MTEX are shown. The ring shaped zones of high and low intensities for the 111 and 200 reflections respectively, which are characteristic for the {100} fibre texture are not fully reproduced, which is probably due to the limited coverage of the raw pole figures. As a comparison the data were also analysed using the Rietveld software MAUD and the EWIMV [42] algorithm for ODF estimation. In Fig. 1.9 the recalculated pole figures are presented. Here the {100} fibre texture is clearly visible, however it has to be noted that cylindrical specimen symmetry was selected to obtain these results. Fig. 1.10 depicts the pole figures measured in the laboratory, which were used as a benchmark for the software tools.

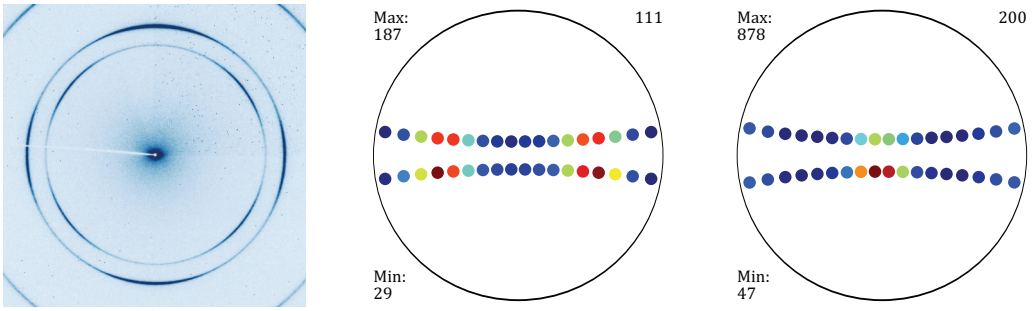

Figure 1.7.: Diffraction image (a) and the corresponding raw pole figures for the TiN 111 (b) and 200 (c) reflection.

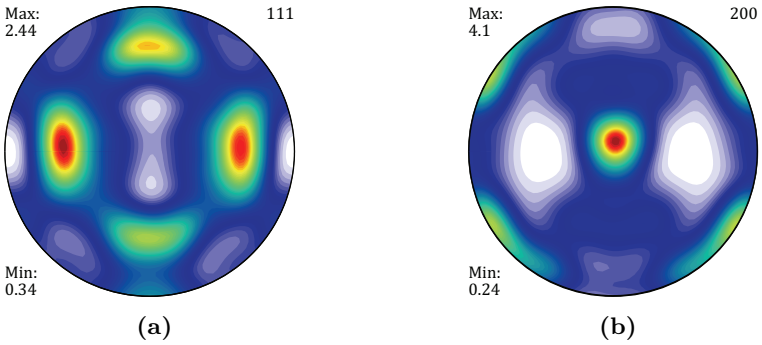

Figure 1.8.: Recalculated pole figures by MTEX for the TiN 111 (a) and 200 (b) reflection.

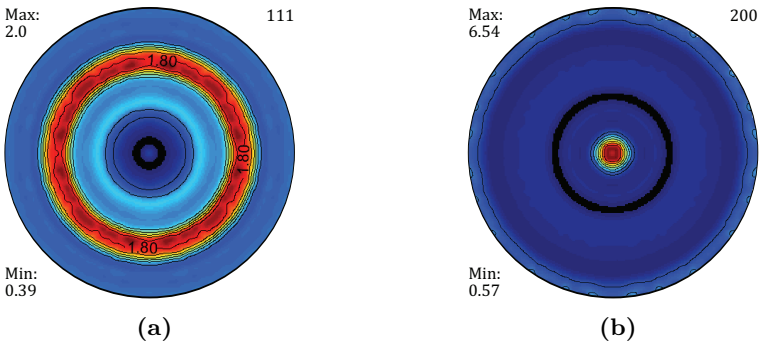

Figure 1.9.: Recalculated pole figures by MAUD for the TiN 111 (a) and 200 (b) reflection.

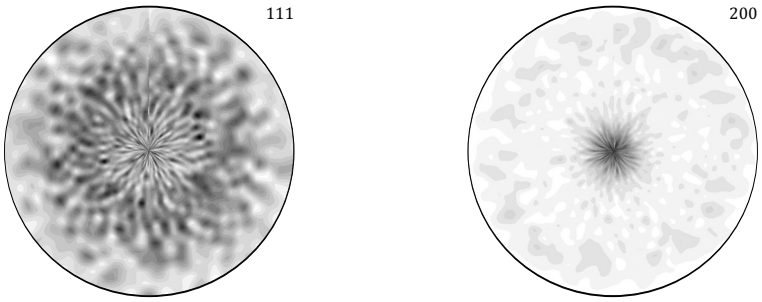

Figure 1.10.: Pole figures for the TiN 111 (a) and 200 (b) reflection measured in the laboratory with a Rigaku SmartLab diffractometer.

1.2.3. Conclusions

Both software packages were able to reproduce the {100} fibre texture of TiN thin film. In the case of MTEX this was not as exact due to the limited coverage of the raw pole figures. Since MTEX does not offer the option of cylindrical specimen symmetry, triclinic was chosen. Manuel symmetry operations when preparing the data, like virtually rotating the sample around the z-axis, could improve the result if a fibre texture is present [21] but it has to be decided in every particular case weather this assumption is applicable. The same applies for the selection of the specimen symmetry in MAUD. In the case of the studied TiN film the assumption seems justified. However in both cases, MTEX and MAUD, it should be kept in mind that a single diffraction frame contains only a part of the texture information. Therefore the plausibility of the results needs to be carefully judged, especially for more complex or less distinct textures as in the presented case.

The great advantage of using MTEX to process large quantities of data is, that no Rietveld analysis has to be performed prior to the ODF calculation and since MTEX is Matlab based it can easily be implemented into evaluation routines. Combining X-ray nanodiffraction and MTEX makes it now possible to estimate the ODF for every diffraction image of a measurement. So texture, strain and phases can now be characterised with a spatial resolution down to 100 nm with one single diffraction experiment.

1.3. Stress Gradients in Thin Films determined using a Laplace Space Approach

Nanocrystalline thin films often exhibit a non-uniform distribution of residual stresses $\sigma(z)$ across their thickness z, which can originate (i) from the varying deposition conditions, (ii) from a self-organization phenomena like competitive grain growth [6–9, 43–45] resulting usually in a complex microstructure and/or (iii) from a post-deposition treatment such as blasting [46] (*cf.* Paper A) or heat treatment [47]. X-ray diffraction in combination with an inverse Laplace transformation of the measured data $\sigma(\tau)$ is a common approach to evaluate residual stress gradients $\sigma(z)$ along the surface normal z of thin films [22, 23, 31, 48–50]. There is a variety of X-ray experimental techniques, such as grazing incidence diffraction [31, 51], the $\sin^2\psi$–technique [22, 23, 31, 48, 49, 52, 53] or energy dispersive X-ray diffraction [54–57], that can be employed to determine $\sigma(\tau)$. But in all cases the main principle is to vary the penetration depth τ of the X-ray beam into the material, which is governed by Eq. (1.12), where τ is defined as the thickness of the layer contributing to 63 % of the measured intensity [31]. In Eq. (1.12), τ can be controlled by either changing the angles α and β, that depend on the Bragg angle θ and the orientation of the scattering vector $\bar{Q}$, or the wavelength as this will influence the mass attenuation coefficient μ. In case the calculated penetration depth of the X-ray beam exceeds the thickness of the thin film D, the origin of the measured information is given by the "information depth" τ_{eff} according to Eq. (A.5) [23, 48], where the maximum possible value for τ_{eff} is $\frac{D}{2}$ [51].

$$\tau = \frac{1}{\mu}\frac{\sin\alpha\,\sin\beta}{\sin\alpha+\sin\beta} \tag{1.12}$$

$$\tau_{eff} = \tau - \frac{D\,e^{-D/\tau}}{1-e^{-D/\tau}} \tag{1.13}$$

In the case of in-plane equi-biaxial stress with zero shear stress components, i.e. $\sigma_{11}=\sigma_{22}=\sigma_{\parallel}$ and $\sigma_{33}=\sigma_{ij}=0$, the residual stress in the Laplace space $\sigma_{\parallel}(\tau)$ can be determined from the measured lattice strain $\varepsilon_{\psi}(hkl,\tau)$ according to Eq. (A.3), where ψ is the tilt angle of the diffraction vector and $F_{\parallel}(hkl,\psi)$ is the stress factor [31]. The correlation between the data in the Laplace space and the data in the real space is given in Eq. (1.15), which has the form of a Laplace transformation (if the integral would extend to infinity) [31]. Since it is very difficult to calculate an inverse Laplace transformation from a measured profile $\sigma_{\parallel}(\tau)$ numerically, relatively

simple analytical functions with known Laplace transformations are fit to $\sigma_{\parallel}(\tau)$ and the obtained (usually polynomial) coefficients determine $\sigma_{\parallel}(z)$ [31, 48, 53], as demonstrated also in Paper A.

$$\sigma_{\parallel}(\tau) = \frac{\varepsilon_{\psi}(hkl, \tau)}{F_{\parallel}(hkl, \psi)} \tag{1.14}$$

$$\sigma(\tau) = \frac{\int_0^D \sigma(z)\, e^{-z/\tau} dz}{\int_0^D e^{-z/\tau} dz} \tag{1.15}$$

1.3.1. Limitation for the Application to Thin Films with Complex Stress Gradients

In Paper A the results from a Laplace approach applied to diffraction data collected in laboratory conditions and at the energy dispersive synchrotron beamline EDDI (at BESSY in Berlin) are compared with the results from a cross-sectional X-ray nanodiffraction experiment, that allows resolving stress gradients directly in real space. It is demonstrated that a monotonous gradient can be reproduced well with the Laplace approach if an appropriate model function for $\sigma(z)$ is chosen. In Fig. A.6 results from Paper A on the stress state in the TiN thin film are shown, where $\sigma(z)$ stays for the data form the nanodiffraction experiment, $\sigma(\tau_{eff})$ are the Laplace space data from the laboratory (Lab) and synchrotron (EDDI) measurements and $\sigma_L(z)$ is the calculated real space profile. It can be seen that $\sigma_L(z)$ is in a good agreement with $\sigma(z)$. Additionally the calculated Laplace space profile (Calc.), obtained by applying Eq. (1.15) to the nanodiffraction data, is presented.

In Fig. A.6 b the Laplace space data $\sigma(\tau_{eff})$ are calculated for a CrN thin film with a complex stress state as reported in [6, 8]. In a second step different functions were used to fit the $\sigma(\tau_{eff})$ data and the obtained real space profile $\sigma_L(z)$ was compared with the nanodiffraction data $\sigma(z)$. The best result obtained using a 5^{th} degree polynomial is shown in Fig. A.6 b. From the comparison between $\sigma_L(z)$ and $\sigma(z)$ it can be seen, that the stress gradient can be reproduced very well in the surface region of the CrN film but not in the other film regions. It has to be noted that this result was obtained by supposing a very good data quality (0.5 µm spatial resolution and no scattering) and by selecting the best result after considering the real space profile, which is generally not known. Hence this can be considered as an idealised case. This confirms the conclusion already drawn in Paper A, that cross-sectional X-ray nanodiffraction is the only technique that allows to accurately resolve residual stress gradients in complex thin films. This applies even more to

thin films having a multilayer architecture, with layer thicknesses in the sub-µm regime as in Paper B.

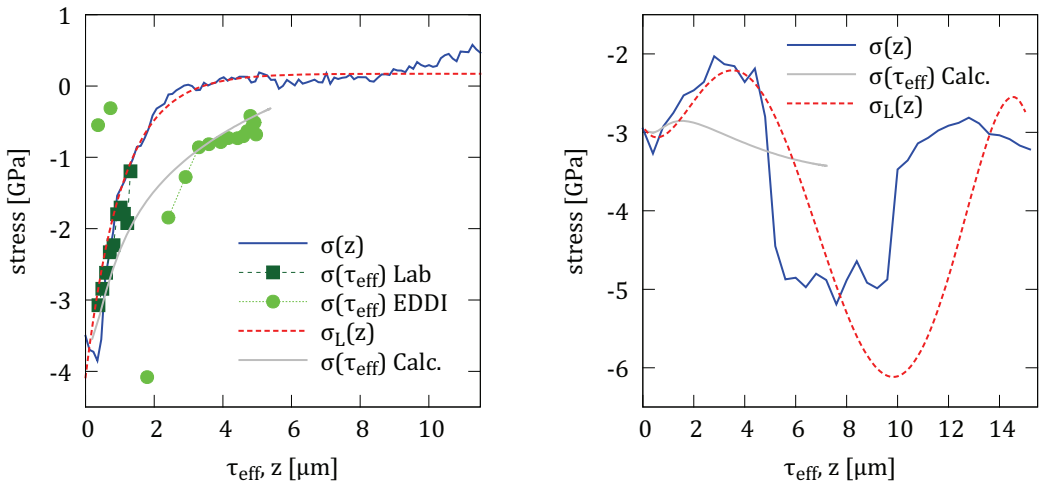

(a) Simple gradient **(b)** Complex gradient

Figure 1.11.: Here the recalculation of the real space stress gradient $\sigma_L(z)$ from Laplace space data $\sigma(\tau_{eff})$ are compared to data obtained from X-ray nanodiffraction $\sigma(z)$. This is done for (a) a simple and (b) a complex stress gradient in a TiN and a CrN thin film respectively. $\sigma(\tau_{eff})$ Lab and EDDI represent data collected from the measurements in the lab and at the synchrotron respectively whereas Calc. denotes the data calculated from $\sigma(z)$ using Eq. (1.15).

1.4. In-situ X-ray Diffraction on Nanocrystalline Thin Films coupled with Four-Point Bending

The influence of deposition parameters and post-deposition treatment of thin films on their mechanical properties has been predominantly characterised using indentation techniques, mechanical tests and X-ray analysis of residual stresses [10, 45, 58, 59]. There are however very few studies that analyse the influence of dedicated deposition recipes and/or post-deposition treatment on the fracture properties of thin films. This kind of correlation can be done using four-point bending tests coupled with X-ray diffraction analysis of stresses, as they offer the possibility to study the fracture behaviour of thin films during macroscopic bending.

When a thin film on a substrate is subjected to an external tensile strain, the stress in the film along the tensile direction σ_{11} can be predicted by Hooke's law Eq. (1.16) [60, 61], where E_f, ν_f, ν_s are the macroscopic elastic constants of the film

and the substrate respectively, $\varepsilon_{f,res}$ is the strain caused be the residual stress in the film and ε_a is the applied strain. It has been found [61], that at a certain point the stress in a thin film on a substrate σ_{11} diverges from the prediction (Eq. (1.16)) and reaches a plateau value as it can be seen in the experimental data shown in Fig 1.12. The formation of the plateau value can be attributed to the formation of parallel cracks which are oriented perpendicular to the loading direction of the film [62–64].

$$\sigma_{11} = \frac{E_f}{1-\nu_f}\left(\varepsilon_{f,res} + \frac{1-\nu_f\nu_S}{1-\nu_f}\varepsilon_a\right) \tag{1.16}$$

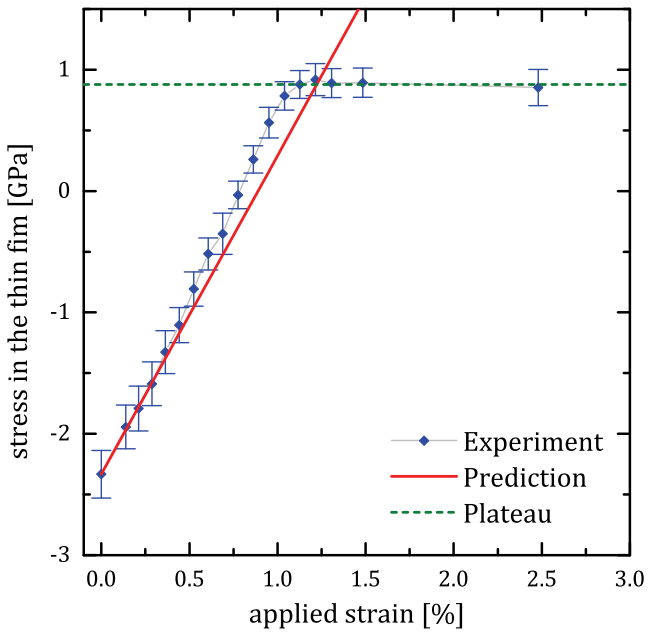

Figure 1.12.: Experimental data for the −40 V CrN film from Paper C in comparison to the prediction given in Eq. (1.16). The plateau provides an estimate of the film fracture stress.

The shear-lag model allows to predict the stress distribution $\sigma(x, \lambda, \varepsilon_a)$ [62] (*cf.* Paper C) at a given applied strain ε_a and a crack spacing λ as shown in Fig. 1.13. Ahmed et al. [62] could show that if $\sigma(x)$ exceeds the fracture stress of the film σ_F, a new crack is formed and the stress drops to $\sigma\left(x, \frac{\lambda}{2}\right)$ (*cf.* Fig. 1.13). Since $\sigma(x)$ also depends on the crack length λ, below a certain crack length $\sigma(x)$ does not exceed the fracture stress of the film any more, therefore the observed plateau is formed in the measured stress dependence on the applied strain [62, 63]. This goes along with crack spacing reaching a saturation value $\bar{\lambda}$. The plateau value can now be used as an estimate for the fracture properties of the film. To determine an exact

value of σ_F, in-situ straining experiments as in [62] would be required. The crack spacing λ can be correlated with the fracture toughness of the film, it is however over-estimated if $\bar{\lambda}$ is applied [63].

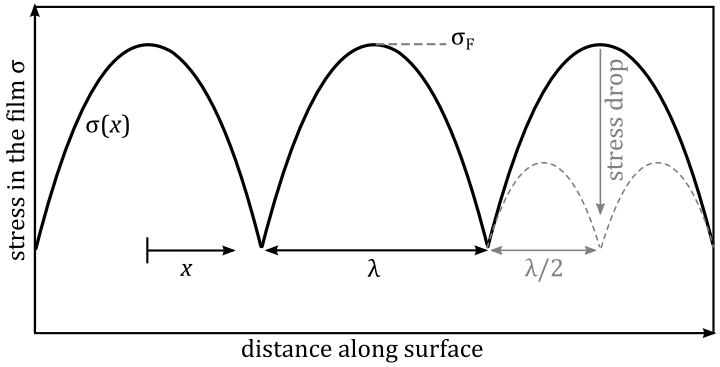

Figure 1.13.: Scheme of theoretic stress distribution $\sigma(x)$ in a film with multiple cracks that space with λ and formation of a new crack with spacing $\frac{\lambda}{2}$ when the stress in a segment exceeds the fracture stress of the film σ_F. Image adapted from Paper C.

In Paper C, four-point bending coupled with X-ray diffraction has been applied to study the effects of the applied bias voltage during deposition and the post deposition heat treatment on fracture behaviour of magnetron sputtered CrN thin films. It was shown, that the change in the bias voltage from $-40\,\mathrm{V}$ to $-120\,\mathrm{V}$ modified the observed fracture behaviour and the observed plateau stresses changed from about 1 GPa tensile to just below 0 GPa. Since the $-120\,\mathrm{V}$ thin film exhibits higher compressive residual stresses after the deposition, the overall stress change during bending was larger. The evaluation of $\bar{\lambda}$ from SEM images also indicates a higher fracture toughness for the $-120\,\mathrm{V}$ film. Upon heat treatment above the deposition temperature the initial residual stresses in the film are relaxed due to the recovery of defects [45, 58]. This is very pronounced for the $-120\,\mathrm{V}$ film as it carries more defects from the deposition process [65, 66]. Heat treatment thus decreases fracture stress and toughness of the $-120\,\mathrm{V}$ film whereas there is practically no change in the $-40\,\mathrm{V}$ film.

In conclusion it can be said that four-point bending coupled with X-ray diffraction can be effectively used to assess the fracture properties of thin films especially when it is used comparatively. In order to determine fracture stress and toughness quantitatively in-situ X-ray diffraction experiments with µm-resolution coupled with an optical observation of the crack development across the film surface would be have to be applied.

1.5. Mapping Three-Dimensional Residual Stresses in Engineering Components

X-ray analysis is often referred to as a non-destructive characterisation technique. But for large bulky samples, cutting the sample is often inevitable (e. g. for railway rails) and usually results in stress relaxation. Consequently, for large engineering components there is a need to use techniques which allow for non-destructive characterization of uncut sample pieces with the preserved initial stress state.

Diffraction experiments used for 3D residual stress characterization are usually performed in reflection geometry, as the measurement in transmission implies averaging in beam direction which usually results in an undesirable peak broadening. The probed volume element and hence the spatial resolution is defined by the gauge volume, which is defined by the apertures as shown in Fig. 1.14 [67]. Strain mapping in bulk samples is performed by a controlled sample movement in the beam. In order to determine the diagonal components of the stress tensor σ_{ii} using Eq. (1.17) [23], at least three independent lattice parameter measurements have to be carried out for every measurement point to determine the principal components of the strain tensor ε_{ii}^{hkl}. This is under the assumption that the principal components are oriented in direction of the coordinate axis, otherwise at least six independent lattice parameter measurements are required [23, 67]. Here E^{kl} and ν^{hkl} are X-ray elastic constants for the reflection hkl.

Especially for large components the long beam pathways in the material demand the use of high X-ray energies which are only available at synchrotron sources. If the components are very large, neutron diffraction becomes favourable as the penetration depth is larger and the wavelength in the Angstrom regime allows for diffraction angles of about 90°, whereas the Bragg's angle of high energy synchrotron radiation is usually only a few degrees [5, 67]. Therefore neutron diffraction will allow shorter pathways in the material. But on the other hand the neutron flux is a few orders of magnitude lower, thus resulting in longer counting times [5] and offering lower spatial resolution as larger gauge volumes need to be chosen.

$$\sigma_{ii} = \frac{E^{hkl}}{(1+\nu^{hkl})}\left[\varepsilon_{ii}^{hkl} + \frac{\nu^{hkl}}{(1-2\nu^{hkl})}\left(\varepsilon_{11}^{hkl} + \varepsilon_{22}^{hkl} + \varepsilon_{33}^{hkl}\right)\right] \quad \text{where } i = 1,2,3 \tag{1.17}$$

Another approach that overcomes the limitation to the reflection geometry is the

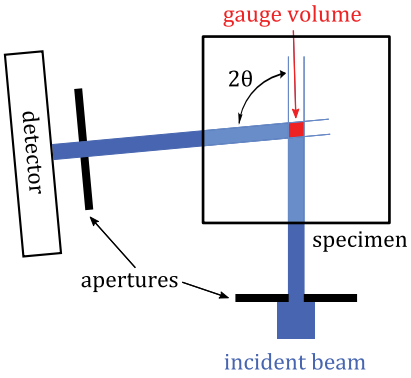

Figure 1.14.: Diffraction setup in reflection geometry. The probed volume element in the sample is defined by the gauge volume, which can be controlled by the apertures. Here the 2θ-angle is drawn for neutron diffraction, where it is about 90°. In the case of high energy synchrotron diffraction 2θ is only a few degrees resulting in longer path ways in the material.

use of a conical slit cell (CSC) [68] as shown in Fig. 1.15. The CSC is a plate with several very thin conical slits, that have a common focus point. This permits to select a specific sample volume element in transmission geometry. In this case it is possible to collect full Debye-Scherrer rings, which already contain the strain information of two principal directions, so only two measurements in different orientations are required to evaluate three principal stress components according to Eq. (1.17) . Alternatively the stress components can be also evaluated using Eq. 1.7, if diffraction data from two reflections are available. Additionally information about texture and size and shape of the grains can be extracted from the Debye-Scherrer ring intensity profile and broadening [6, 10].

In any case it is necessary to obtain D_0^{hkl} from a reference measurement for the quantification of ε^{hkl} according to Eq. 1.1.

Within this thesis, neutron diffraction in reflection geometry and the CSC are used to characterise 3D residual stress fields in large engineering components.

In Paper D neutron diffraction is applied to determine the 3D residual stress distribution in a roller straightened railway rail at the Stress-Spec neutron diffractometer of the FRMII facility in Garching, Germany using a gauge volume of $5 \times 5 \times 5\,\mathrm{mm}^3$ [69] The focus is laid on the characterisation of the longitudinal residual stresses as these are a standardised quality criterion. Neutron diffraction is chosen because it is the only technique allowing to measure in the head of a 0.5 m long piece of rail with beam path lengths in the material up to 7 cm. The data correlates well with the results of the contour method and finite element modelling. Using the neutron measurement as a benchmark it can be concluded that the two other methods can

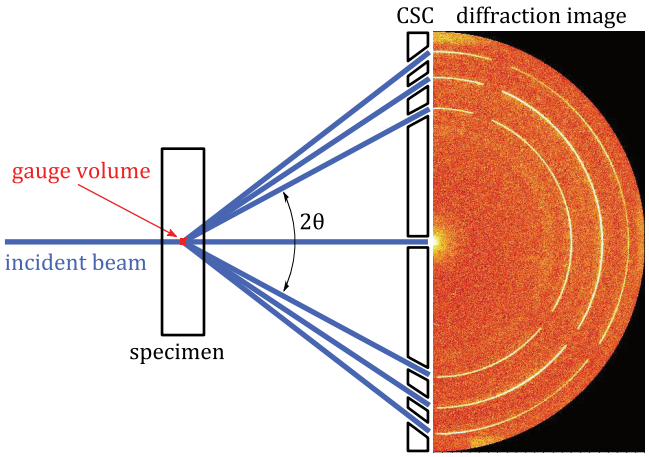

Figure 1.15.: Experimental setup for a measurement using the CSC. Here the probed volume is defined by the beamsize of the incident beam and the focus point of the CSC. Diffraction image taken from from Paper E.

be used to effectively predict and determine the residual stress state in straightened railway rails.

In Paper E the CSC is applied at the HEMS (P07) beamline of PETRA III at DESY, Germany to locally map residual stress gradients in seamless rolled steel tubes with high energy synchrotron diffraction. It is shown that the CSC can be effectively used to map the residual stresses in the tube wall, having a thickness of 9.8 cm, with a spatial resolution of 0.8 mm. In this way, it was possible to resolve the very steep stress gradients in the tube walls, documenting the importance of the cooling process control during the production as it has a decisive influence on the final residual stress state.

Bibliography

[1] S. Gorelick, V. A. Guzenko, J. Vila-Comamala, and C. David. *P Soc Photo-opt Ins*, 21(29), 2010. doi:10.1088/0957-4484/21/29/295303.

[2] C. G. Schroer, M. Kuhlmann, U. T. Hunger, T. F. Gunzler, O. Kurapova, S. Feste, F. Frehse, B. Lengeler, M. Drakopoulos, A. Somogyi, A. S. Simionovici, A. Snigirev, I. Snigireva, C. Schug, and W. H. Schroder. *Appl Phys Lett*, 82(9): 1485–1487, 2003. doi:10.1063/1.1556960.

[3] C. Krywka, H. Neubauer, M. Priebe, T. Salditt, J. Keckes, A. Buffet, S. V. Roth, R. Doehrmann, and M. Mueller. *J Appl Crystallogr*, 45:85–92, February 2012. doi:10.1107/S0021889811049132.

[4] S. Niese, P. Krüger, A. Kubec, R. Laas, P. Gawlitza, S. Melzer, K. c.and Braun, and E. Zschech. *Thin Solid Films*, 2014. doi:10.1016/j.tsf.2014.02.095.

[5] P. J. Withers. *J Appl Crystallogr*, 37(4):596 – 606, 2004. doi:10.1107/S0021889804012737.

[6] J. Keckes, M. Bartosik, R. Daniel, C. Mitterer, G. Maier, W. Ecker, J. Vila-Comamala, C. David, S. Schoeder, and M. Burghammer. *Scripta Mater*, 67(9): 748–751, 2012. doi:10.1016/j.scriptamat.2012.07.034.

[7] R. Daniel, E. Jäger, J. Todt, B. Sartory, C. Mitterer, and J. Keckes. *J Appl Phys*, 115(20), 2014. doi:10.1063/1.4879243.

[8] R. Daniel, J. Keckes, I. Matko, M. Burghammer, and C. Mitterer. *Acta Mater*, 61(16):6255–6266, 2013. doi:10.1016/j.actamat.2013.07.009.

[9] M. Bartosik, R. Daniel, C. Mitterer, I. Matko, M. Burghammer, P. Mayrhofer, and J. Keckes. *Thin Solid Films*, 542:1–4, 2013. doi:10.1016/j.tsf.2013.05.102.

[10] M. Bartosik. *Non-homogeneous structural and mechanical properties of nanocrystalline thin films characterized by advanced X-ray diffraction techniques*. PhD thesis, Montanuniversität Leoben, 2012.

[11] A. P. Hammersley, S. O. Svensson, M. Hanfland, A. N. Fitch, and D. Häusermann. *High Pressure Res*, 14:235–248, 1996.

[12] A. Zeilinger, M. Stefenelli, J. Todt, C. Krywka, R. Daniel, C. Mitterer, and J. Keckes. In-situ X-ray nanodiffraction reveals stress and microstructure changes in TiN thin film during indentation (tenative title). manuscript in preparation.

[13] J. Kieffer and D. Karkoulis. *J Phys Conf Ser*, 425(202012), 2013. doi:10.1088/1742-6596/425/20/202012.

[14] J. Kieffer and J. P. Wright. *Powder Diffr*, 28:339–350, September 2013. doi:10.1017/S0885715613000924.

[15] The HDF Group. Hierarchical Data Format, version 5, 1997–2014. URL `http://www.hdfgroup.org/HDF5/`.

[16] C. Riekel, M. Burghammer, and R. Davies. *IOP C Ser Mat Sci Eng*, 14(012013), 2010. doi:10.1088/1757-899x/14/1/012013.

[17] C. Krywka, J. Keckes, S. Storm, A. Buffet, S. Roth, R. Döhrmann, and M. Müller. *J Phys Conf Ser*, 425(072021), 2013. doi:10.1088/1742-6596/425/7/072021.

[18] Riverbank Computing Limited. PyQt4 reference guide. URL `http://pyqt.sourceforge.net/Docs/PyQt4/#`.

[19] quiqwt. URL `http://pythonhosted.org/guiqwt/index.html`.

[20] J. D. Hunter. *Computing In Science & Engineering*, 9(3):90–95, 2007. doi:10.1109/MCSE.2007.55.

[21] B. B. He. *Two-Dimensional X-Ray Diffraction*. Wiley, 2009.

[22] I. C. Noyan and J. B. Cohen. *Measurement by Diffraction and Interpretation*. Springer, 1987.

[23] V. Hauk. *Structural and Residual Stress Analysis by Nondesdestructive Methods*. Elsevier, 1997.

[24] F. Heidelbach, C. Riekel, and H. R. Wenk. *J Appl Crystallogr*, 32:841–849, 1999. doi:10.1107/s0021889899004999.

[25] B. B. He. *Powder Diffraction*, 18(2):71–85, June 2003. doi:10.1154/1.1577355.

[26] S. J. B. Kurz, S. R. Meka, N. Schell, W. Ecker, J. Keckes, and E. J. Mittemeijer. Microstructural depth gradients in nitrided iron-based alloys revealed by cross-sectional high-energy X-ray microdiffraction (tenative title). manuscript in preparation.

[27] R. Daniel, K. Martinschitz, J. Keckes, and C. Mitterer. *J. Phys. D: Appl. Phys.*, 42(7):075401, 2009. doi:10.1088/0022-3727/42/7/075401.

[28] M. Ahlgren and H. Blomqvist. *Surf. Coat. Technol.*, 200(1-4):157–160, 2005. doi:10.1016/j.surfcoat.2005.02.078.

[29] D. Rafaja, M. Šíma, V. Klemm, G. Schreiber, D. Heger, L. Havela, and R. Kužel. *J Alloy Compd*, 378(1-2):107–111, 2004. doi:10.1016/j.jallcom.2003.10.087.

[30] C. Falub, A. Karimi, M. Ante, and W. Kalss. *Surf. Coat. Technol.*, 201(12): 5891–5898, 2007. doi:10.1016/j.surfcoat.2006.10.046.

[31] M. Birkholz. *Thin Film Analysis by X-Ray Scattering*. WILEY-VCH, 2006.

[32] H. Joo, J. Kim, K. Kim, N. Tamura, and Y. Koo. *Scripta Mater*, 51(12): 1183–1186, 2004. doi:10.1016/j.scriptamat.2004.07.003.

[33] A. P. Stebner, S. C. Vogel, R. D. Noebe, T. A. Sisneros, B. Clausen, D. W. Brown, A. Garg, and L. C. Brinson. *J Mech Phys Solids*, 61(11):2302–2330, November 2013. doi:10.1016/j.jmps.2013.05.008.

[34] S. Cai, J. E. Schaffer, Y. Ren, and C. Yu. *Appl Phys Lett*, 103(24):241909, December 2013. doi:10.1063/1.4846495.

[35] R. Hielscher and H. Schaeben. *J Appl Crystallogr*, 41(6):1024–1037, Nov 2008. doi:10.1107/s0021889808030112.

[36] M. Y. Xie, N. Baimpas, C. Reinhard, and A. M. Korsunsky. *J Appl Phys*, 114 (16):163502, 2013. doi:10.1063/1.4825120.

[37] U. Oh and J. Je. *J Appl Phys*, 74(3):1692–1696, 1993. doi:10.1063/1.355297.

[38] J. Zhao, X. Wang, Z. Chen, S. Yang, T. Shi, and X. Liu. *J. Phys. D: Appl. Phys.*, 30(1):5–12, 1997. doi:10.1088/0022-3727/30/1/002.

[39] J. A. Thornton. *Annu Rev Mater Sci*, 7(1):239–260, 1977. doi:10.1146/annurev.ms.07.080177.001323.

[40] J.-S. Chun, I. Petrov, and J. Greene. *J Appl Phys*, 86(7):3633–3641, 1999. doi:10.1063/1.371271.

[41] L. Lutterotti, R. Vasin, and H.-R. Wenk. *Powder Diffr*, 29(1):76–84, 2014. doi:10.1017/S0885715613001346.

[42] L. Lutterotti, D. Chateigner, S. Ferrari, and J. Ricote. *Thin Solid Films*, 450 (1):34–41, 2004. doi:10.1016/j.tsf.2003.10.150.

[43] M. Ohring. *Materials Science of Thin Films. Deposition and Structure*. Academic Press, London, 2nd edition, 2002.

[44] A. Cavaleiro and J. T. M. De Hosson, editors. *Nanostructured Coatings*. Springer, New York, 2006.

[45] P. H. Mayrhofer, C. Mitterer, L. Hultman, and H. Clemens. *Prog Mater Sci*, 51(8):1032–1114, 2006. doi:10.1016/j.pmatsci.2006.02.002.

[46] M. Bartosik, R. Pitonak, and J. Keckes. *Adv Eng Mater*, 13(8):705–711, 2011. doi:10.1002/adem.201000299.

[47] J. Todt, R. Pitonak, A. Köpf, R. Weißenbacher, B. Sartory, M. Burghammer, R. Daniel, T. Schöberl, and J. Keckes. *Surf. Coat. Technol.*, Article in Press, 2014. doi:10.1016/j.surfcoat.2014.07.022.

[48] C. Genzel. *Phys Status Solidi A*, 159(2):283–296, 1997.

[49] H. Dölle. *J Appl Crystallogr*, 12(6):489–501, 1979. doi:10.1107/s0021889879013169.

[50] C. Genzel. *Phys Status Solidi A*, 156(2):353–363, 1996. doi:10.1002/pssa.2211560213.

[51] C. Genzel. *Mater Sci Technol*, 21(1):10–18, 2005. doi:10.1179/174328405X14100.

[52] D. Faurie, O. Castelnau, P.-O. Renault, G. Patriarche, R. Brenner, E. Le Bourhis, and P. Goudeau. *Surf. Coat. Technol.*, 201(7):4300–4304, 2006. doi:10.1016/j.surfcoat.2006.08.037.

[53] P. Scardi and Y. H. Dong. *J Mater Res*, 16:233–242, 2001. doi:10.1557/JMR.2001.0036.

[54] C. Genzel, I. A. Denks, J. Gibmeler, M. Klaus, and G. Wagener. *Nucl Instrum Meth A*, 578(1):23–33, 2007. doi:10.1016/j.nima.2007.05.209.

[55] C. Genzel, C. Stock, and W. Reimers. *Mat Sci Eng A*, 372(1-2):28–43, May 2004. doi:10.1016/j.msea.2003.09.073.

[56] M. Klaus and C. Genzel. *J Appl Crystallogr*, 46:1266–1276, October 2013. doi:10.1107/S0021889813018517.

[57] M. Meixner, M. Klaus, and C. Genzel. *J Appl Crystallogr*, 46:610–618, June 2013. doi:10.1107/S0021889813008340.

[58] K. Martinschitz, R. Daniel, C. Mitterer, and J. Keckes. *Thin Solid Films*, 516 (8):1972–1976, 2008. doi:10.1016/j.tsf.2007.10.106.

[59] A. Riedl, R. Daniel, M. Stefenelli, T. Schöberl, O. Kolednik, C. Mitterer, and J. Keckes. *Scr. Mater.*, 67(7-8):708–711, 2012. doi:10.1016/j.scriptamat.2012.06.034.

[60] U. Wiklund, M. Bromark, M. Larsson, P. Hedenqvist, and S. Hogmark. *Surf. Coat. Technol.*, 91(1-2):57 – 63, 1997. doi:10.1016/S0257-8972(96)03123-4.

[61] T. Ito, K. Tanaka, Y. Akiniwa, T. Ishii, and Y. Miki. *JSME Int J A-Solid M*, 46(1):86–92, 2003. doi:10.1299/jsmea.46.86.

[62] F. Ahmed, K. Bayerlein, S. Rosiwal, M. Göken, and K. Durst. *Acta Mater.*, 59 (14):5422–5433, 2011. doi:10.1016/j.actamat.2011.05.015.

[63] S. Frank, U. A. Handge, S. Olliges, and R. Spolenak. *Acta Mater*, 57(5):1442–1453, 2009. doi:10.1016/j.actamat.2008.11.023.

[64] C. Hsueh and M. Yanaka. *J Mater Sci*, 38(8):1809–1817, 2003. doi:10.1023/A:1023200415364.

[65] D. M. Mattox. *J Vac Sci Technol A*, 7(3):1105–1114, 1989. doi:10.1116/1.576238.

[66] R. Daniel, K. Martinschitz, J. Keckes, and C. Mitterer. *Acta Mater*, 58(7): 2621–2633, 2010. doi:10.1016/j.actamat.2009.12.048.

[67] M. T. Hutchings, P. J. Withers, T. M. Holden, and T. Lorentzen. *Introduction to the characterization of residual by neutron diffraction*. CRC Press / Taylor & Francis, Boca Raton, FL, 2005.

[68] S. Nielsen, A. Wolf, H. Poulsen, M. Ohler, U. Lienert, and R. Owen. *J Synchrotron Radiat*, 7(2):103–109, 2000. doi:10.1107/S0909049500000625.

[69] M. Hofmann, R. Schneider, G. A. Seidl, J. Rebelo-Kornmeier, R. C. Wimpory, U. Garbe, and H.-G. Brokmeier. *Physica B*, 385-386(Part 2):1035–1037, 2006. doi:10.1016/j.physb.2006.05.331.

2

List of Appended Publications

2.1. First Author Papers

Paper A

M. Stefenelli, J. Todt, A. Riedl, W. Ecker, T. Müller, R. Daniel, M. Burghammer and J. Keckes

X-ray analysis of residual stress gradients in TiN coatings by a Laplace space approach and cross-sectional nanodiffraction: A critical comparison

Journal of Applied Crystallography 46 (5):1378–1385, 2013

doi:10.1107/S0021889813019535

Paper B

M. Stefenelli, R. Daniel, W. Ecker, D. Kiener, J. Todt, A. Zeilinger, C. Mitterer, M. Burghammer and J. Keckes

X-ray Nanodiffraction reveals Stress Distribution across an Indented Multilayered CrN-Cr Thin Film

submitted manuscript

Paper C
M. Stefenelli, A. Riedl, J. Todt, M. Bartosik, R. Daniel, C. Mitterer and J. Keckes
Macroscopic fracture behaviour of CrN hard coatings evaluated by X-ray diffraction coupled with four-point bending
Materials Science Forum 768–769 :272–279, 2014
doi:10.4028/www.scientific.net/MSF.768-769.272

2.2. Co-author Papers

Paper D
R. Kaiser, M. Stefenelli, T. Hatzenbichler, T. Antretter, M. Hofmann, J. Keckes and B. Buchmayr
Experimental Characterization and Modelling of Triaxial Residual Stresses in Straightened Railway Rails
submitted manuscript

Paper E
G. Winter, M. Stefenelli, J. Klarner, P. Staron, T. Fischer, J. Keckes and B. Buchmayr
Triaxial residual stresses in thermomechanically rolled seamless tubes characterized by high-energy synchrotron x-ray diffraction
American Society of Mechanical Engineers, Pressure Vessels and Piping Division (Publication) PVP 3 2013
doi:10.1115/PVP2013-97963

2.3. Contribution of the author to the papers

Table 2.1.: Contribution of the Author to the appended publications in percent.

	Conception and planning	Experiments	Analysis and interpretation	Manuscript preparation
Paper A	100	90	80	80
Paper B	100	85	75	80
Paper C	100	95	95	90
Paper D	50	40	40	40
Paper E	20	30	20	20

A

X-Ray Analysis of Residual Stress Gradients in TiN Coatings by a Laplace Space Approach and Cross-Sectional Nanodiffraction: A Critical Comparison

Mario Stefenelli[a], Juraj Todt[b,c], Angelika Riedl[a], Werner Ecker[a], Thomas Müller[d], Rostislav Daniel[e], Manfred Burghammer[f], Jozef Keckes[b,c]

[a]Materials Center Leoben Forschung GmbH, Leoben, Austria

[b]Department of Materials Physics, Montanuniversität Leoben, Austria

[c]Erich Schmid Institute of Materials Science, Austrian Academy of Sciences, Leoben, Austria

[d]Rübig GmbH&CoKG, Durisolstraße 12, Wels, Austria

[e]Department of Physical Metallurgy and Materials Testing, Montanuniversität Leoben, Austria

[f]ESRF, 38043 Grenoble Cedex 9, France

Abstract

Novel scanning synchrotron cross-sectional nanobeam and conventional laboratory as well as synchrotron Laplace X-ray diffraction methods are used to characterize residual stresses in exemplary 11.5 µm thick TiN coatings. Both real and Laplace space approaches reveal a homogeneous tensile stress state and a very pronounced compressive stress gradient in as-deposited and blasted coatings, respectively. The unique capabilities of the cross-sectional approach operating with a beam size of 100 nm in diameter allow to analyse stress variation with sub-micron resolution at arbitrary depths and to correlate the stress evolution with the local coating microstructure. Finally advantages and disadvantages of both approaches are extensively discussed.

A.1. Introduction

Protective hard coatings used for high-speed applications in the metal working industry possess complex depth gradients of phases, microstructure and residual stresses. Those gradients can be related to the effects of varying deposition conditions, self-organization phenomena like competitive grain growth and/or post-deposition mechanical and thermal loads caused e.g. by friction between coating and counterpart [1, 2].

X-ray diffraction (XRD) represents a common technique to evaluate residual stress gradients $\sigma(z)$ along the surface normal z in polycrystalline thin films and coatings from measured X-ray elastic strains using the $\sin^2\psi$ technique [3–6]. The inclination of the diffraction vector with respect to the sample normal is given by the angle ψ. The measured lattice spacing $d\,(hkl,\tau,\psi)$ and X-ray elastic strains $\varepsilon\,(hkl,\tau,\psi)$ represent volume-average quantities which depend on the actual stress depth profile $\sigma(z)$, X-ray penetration depth τ, reflection hkl and experiment geometry. In general, $d\,(hkl,\tau,\psi)$ and $\varepsilon\,(hkl,\tau,\psi)$ can be related as follows [7, 8]

$$\varepsilon(hkl,\tau,\psi)=\frac{d\,(hkl,\tau,\psi)-d_0\,(hkl)}{d_0\,(hkl)}=\frac{1}{d_0\,(hkl)}\frac{\int_0^D d\,(hkl,\tau,\psi)\,e^{-z/\tau}dz}{\int_0^D e^{-z/\tau}dz} \tag{A.1}$$

where D is the coating thickness and $d_0\,(hkl)$ is the unstressed lattice parameter. By varying τ during a diffraction experiment it is possible to evaluate $\varepsilon\,(hkl,\tau,\psi)$ and $\sigma(\tau)$ dependencies experimentally in the so-called Laplace space. For the quantification of the stress gradient $\sigma(z)$ from experimental $\sigma(\tau)$ as a function of z in real space, however, it is necessary to solve a complex inverse problem similar to

inverse Laplace transformation. Since the transformation between $\sigma(\tau)$ and $\sigma(z)$ is not ambiguously defined, it is necessary to make very strong assumptions about the actual nature of $\sigma(z)$ profile in the real space [5].

Recently, a novel XRD approach based on the cross-sectional nanodiffraction was introduced [9, 10]. The new technique uses synchrotron point (or pencil) X-ray nanobeams with a diameter (or a thickness) down to 100 nm or even less to scan thin films at the cross-section in transmission or in reflection geometries. The advantage of the new scanning method is that the depth gradients of microstructure, residual stresses and phases can be determined directly in the real space as a function of the coating depth z. The approach opens the possibility to analyse stresses in graded thin films [10] and correlate them with texture, crystallite size and phase gradients. The characterization of fibre texture is trivial, including also full orientation distribution function calculation, especially in the case of in-plane isotropic thin films with a fibre axis oriented perpendicular to the substrate surface [9, 11].

In this work residual stress gradients in exemplary as-deposited and blasted nanocrystalline TiN coatings were analysed (i) using the "classical" Laplace method based on the diffraction in reflection geometry and performed in laboratory and synchrotron conditions and (ii) using the recently-developed cross-sectional X-ray nanodiffraction approach providing the structural information in the real space. The main aim of this work is to compare both techniques and to discuss their advantages and disadvantages.

A.2. Experimental

A.2.1. Sample Preparation

For the deposition of the TiN coating with a final thickness of 11.5 µm on monocrystalline Si(100) substrates, an industrial sized plasma-assisted chemical vapour deposition and nitriding plant was used. The central piece is a hot wall reactor featuring wall temperatures up to 600 °C. The reactor is supplied with the process gases ($TiCl_4$, H_2, N_2, Ar) by a standard gas mixing system using mass flow controllers. The plasma is sustained by applying d.c. pulses to the substrates. For the deposition a pressure of 200 Pa was applied. The deposition was carried out in two steps. The first 5 µm of the coating were grown using a substrate temperature of 540 °C, then the temperature was set to 580 °C until the final thickness was reached. After the deposition, one coated substrate was blasted using Al_2O_3 particles with a diameter of 50 µm applying a pressure of 4.0×10^5 Pa. The morphology of the

as-deposited and blasted coatings was examined using scanning electron microscopy (SEM) (*cf.* Fig. A.3).

A.2.2. Laboratory Monochromatic XRD

As-deposited and blasted coatings were characterized using a Rigaku SmartLab 5-axis X-ray diffractometer equipped with Cu-K$_\alpha$ radiation, parallel beam optics and a secondary graphite monochromator. The measurements were conducted in side-inclination mode scanning TiN 200 reflections at different sample tilt angles ψ in the $\sin^2\psi$ range of 0–0.98 in reflection geometry (Fig. A.1). By tilting the samples around the ψ-axis it was possible to vary the X-ray penetration depth τ. The $\sin^2\psi$ range corresponds to a τ range of approximately 0–1.9 µm according to [4, 5]

$$\tau = \frac{1}{2\mu}\sin\theta\cos\psi \tag{A.2}$$

when considering a Bragg angle of about 42.6 ° as well as TiN mass attenuation coefficient of $\mu = 835\,\mathrm{cm}^{-1}$ [12] for Cu-K$_\alpha$ radiation. The lattice spacing $d(hkl, \tau, \psi)$ as a function of τ was evaluated with an error smaller than 10 %.

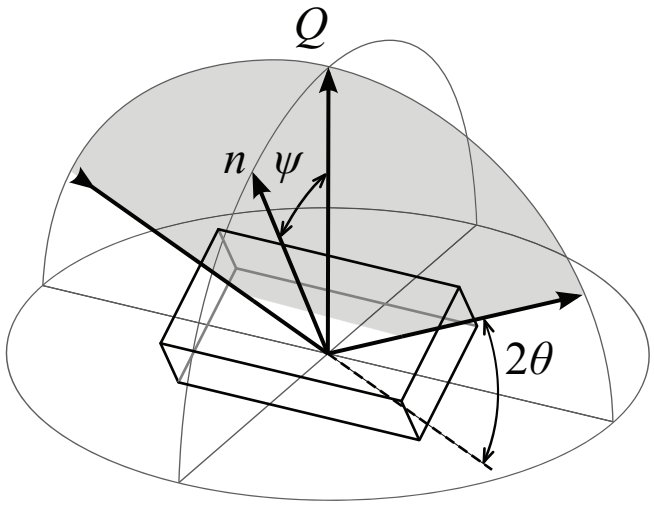

Figure A.1.: X-ray elastic strains were characterized using the $\sin^2\psi$ method by measuring lattice spacing $d(hkl)$ at different sample tilt angles ψ along the direction of the diffraction vector $\boldsymbol{Q}$. The angle ψ represents the angle between the sample normal $\boldsymbol{n}$ and $\boldsymbol{Q}$. By varying the angle ψ, the X-ray penetration depth τ was tuned [4, 5].

A.2.3. Synchrotron Energy Dispersive XRD

Both TiN samples were characterized also at the Energy Dispersive Diffraction (EDDI) beamline of Helmholtz-Zentrum Berlin (BESSY), Germany [13]. The diffraction experiments were carried out using a white X-ray beam in the energy range of 20–100 keV and beam dimensions of 500×500 µm in reflection geometry (Fig. A.1). For the data acquisition, a N_2 cooled LEGe detector system from Canberry with a resolution of 160 eV at 10 keV and 420 eV at 100 keV was used. The acquisition was performed in a symmetric $\theta/2\theta$ configuration at a constant Bragg angle of $2\theta = 12\,^\circ$ using a counting time of 60 s per recorded spectrum. The measurements were used to evaluate the lattice spacing $d(hkl, \tau, \psi)$ by measuring the positions of TiN 200 reflections at an energy of about 28 keV as a function of the sample tilt angle ψ (Fig. A.1) [14]. The lattice spacing $d(200, \tau, \psi)$ dependence on τ was determined (with an error smaller than 10%) using Eq. (A.1) by applying a mass attenuation coefficient of $\mu = 25.14\,\mathrm{cm}^{-1}$ [12].

A.2.4. Cross-Sectional Synchrotron X-ray Nanobeam Experiment

The strain mapping experiment was conducted at the nanofocus extension of the ID13 beamline of the European synchrotron radiation facility (ESRF) in Grenoble, France [15]. A schematic description of the experimental setup is presented in Fig. A.2. A monochromatic X-ray beam of the energy $E = 13$ keV was focused using a Fresnel zone plate [16] providing a beam of 100 nm in diameter. Alternatively, using a nanofocusing parabolic refractive X-ray lenses [17], a (pencil-like) beam with dimensions of about 0.2×5 µm was applied. Both types of setups were tested in order to assess the influence of the beam shape on the diffraction statistics. Due to the nanocrystalline nature of the coatings, there were however no significant differences in the diffraction quality. In the following only results from experiments performed using a point focus will be presented.

The thin sample slice (with a thickness in the beam direction of $L = 20$ µm) was aligned with the film/substrate interface oriented parallel to the beam (Fig. A.2) by using the φ-axis. A charge-coupled device (CCD) area detector with a resolution of 2048×2048 pixels and a pixel size of about 50×50 µm was positioned behind the sample with a sample–detector distance of 102 mm. In order to vertically scan the film cross-section, the sample was moved in the beam along the z-axis with a step width of 100 nm. For each position, the CCD detector acquired a Debye-Scherrer diffraction frame with a counting time of 0.5 s per frame. The two-dimensional diffraction data were processed using the program package Fit2D [18].

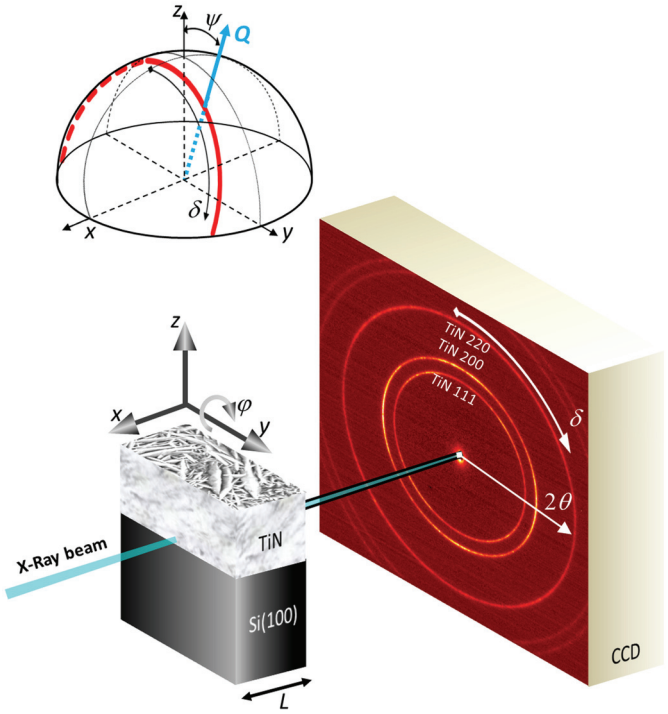

Figure A.2.: A schematic view of the position-resolved XRD experiment carried out in transmission diffraction geometry using a monochromatic X-ray beam of 100 nm in a diameter. The TiN coating on Si(100) substrate (with a thickness $L = 20\,\mu m$ in the beam direction) was moved along the z-axis with a step size of 100 nm and the diffraction data were collected using a CCD detector at the distance of 102 mm from the sample. The beam was aligned parallel to the sample interface using the ϕ-axis movement. The TiN 111, 200 and 220 Debye-Scherrer rings represent diffraction from TiN crystallites. For a Debye-Scherrer ring, the diffraction vectors $\boldsymbol{Q}$ are located on a bold line depicted schematically in the stereographic projection in the top. Please, note that for $\delta = 0$, $\psi = \theta$.

A.3. Results and Discussion

A.3.1. Sample Surface Morphology

Morphologies and cross-sections of as-deposited and blasted TiN coatings were analysed using scanning electron microscopy (SEM) (*cf.* Fig. A.3). The blasting caused an increase in the surface roughness. The SEM cross-sections reveal a nanocrystalline character of the coatings.

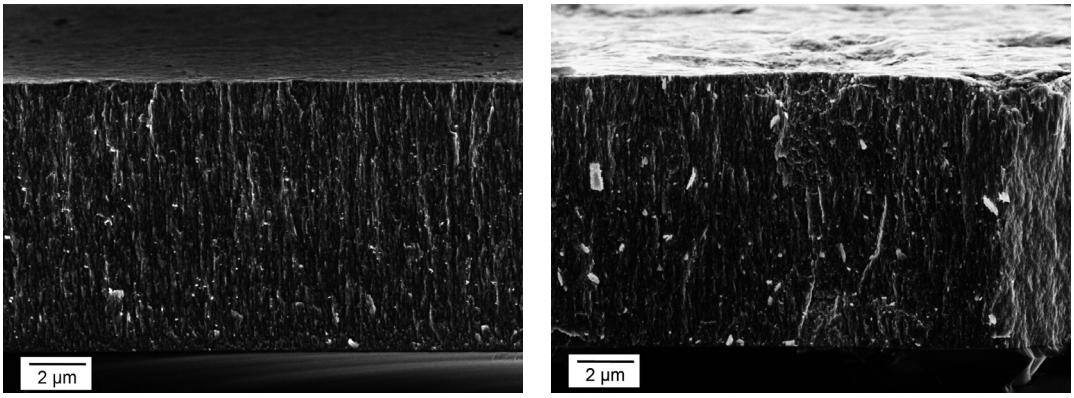

(a) **(b)**

Figure A.3.: Surface and cross-section morphologies of as-deposited (a) and blasted (b) TiN hard coatings reveal a nanocrystalline nature of the coatings and an increase of surface roughness of the blasted coating (b).

A.3.2. Residual Stress Analysis in Laplace Space

For the analysis of residual stresses as a function of coating depth z in as-deposited and blasted coatings, it was assumed that the stresses are equi-biaxial with $\sigma_{11}(z) = \sigma_{22}(z) = \sigma(z)$ and $\sigma_{i3}(z) = 0\,(\mathrm{i}{=}1,2,3)$ and can be expressed by a parameter $\sigma(z)$. Similar for strains, it was supposed that only in-plane $\varepsilon_{11}(z) = \varepsilon_{22}(z) = \varepsilon(z)$ and out-of-plane $\varepsilon_{33}(z)$ strain components are non-zero [3, 19, 20].
As-deposited and blasted TiN coatings were characterized in the laboratory and at the synchrotron source by analysing the positions of TiN 200 reflections (Fig. A.4). The nearly linear $\sin^2\psi$ dependencies with positive slopes collected from the as-deposited coating indicate relatively small tensile residual stresses. The different slopes of the dependencies obtained from the as-deposited coating can be interpreted by the presence of a stress gradient and/or by a different penetration depth of X-rays in both experiments.

The $\sin^2\psi$ dependencies collected from the blasted coating in both experiments show very pronounced curvatures which can be interpreted by the strong gradients of residual stress $\sigma(z)$ [4, 5, 21]. The X-ray elastic strains $\varepsilon(200, \tau, \psi)$ in the coatings were evaluated from $d(200, \tau, \psi)$ values from Fig. A.4 whereby the unstressed lattice parameter d_0 was determined from the intercepts in the $\sin^2\psi$ plots. The biaxial rotational symmetric in-plane residual stress in the Laplace space $\sigma(\tau)$ was

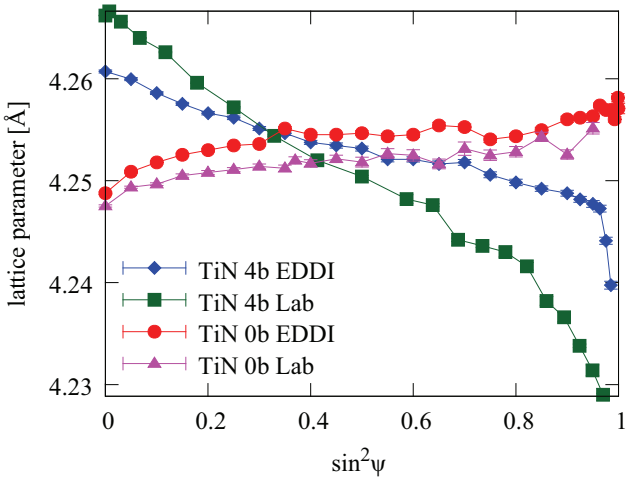

Figure A.4.: Lattice parameters as a function of $\sin^2\psi$ for as-deposited (0b) and blasted (4b) TiN coatings characterized in the laboratory (Lab) and at EDDI beamline (EDDI). The data were obtained by evaluating the positions of TiN 200 reflections.

determined from $\varepsilon(200, \tau, \psi)$ using X-ray diffraction Hooke's law according to [5, 22]

$$\sigma(\tau) = \frac{\varepsilon(200, \tau, \psi)}{F(200, \psi)} \tag{A.3}$$

where $F(200, \psi)$ represents X-ray stress factors which depend on the material texture, single crystal elastic constants, grain interaction, TiN 200 reflection and orientation of the diffraction vector [23, 24]. Since, the TiN thin films were in-plane isotropic and possessed a {100} fibre texture (Fig. A.5), the stress factors $F(200, \psi)$ were for simplicity calculated according to [22]

$$F(hkl, \psi) = 2s_{12} + \left(s_{11} - s_{12} - \frac{1}{4}s_{44}\right)\frac{h^2 + k^2}{h^2 + k^2 + l^2} + \frac{1}{4}s_{44}\sin^2\psi \tag{A.4}$$

whereby, $s_{11} = 2.17$, $s_{12} = -0.38$ and $s_{44} = 5.96 \times 10^{-6}\,\mathrm{MPa}^{-1}$ and $hkl = 200$ [25]. Finally, lattice spacing data obtained from laboratory and synchrotron experiments (Fig. A.4) were used to quantify residual stresses $\sigma(\tau)$ in as-deposited and blasted samples in the Laplace space using Eqs. (A.2–A.4) (Fig. A.6). Since in the case of the synchrotron experiment performed using relatively hard X-rays, the maximal penetration depth τ exceeds significantly the coating thickness D, the "information depth" τ_{eff} is defined in order to express the origin of the measured information

[4, 22]

$$\tau_{eff} = \tau - \frac{D\, e^{-D/\tau}}{1 - e^{-D/\tau}} \tag{A.5}$$

The results from Fig. A.6 document different penetration depths accessible at different facilities. In the case of laboratory measurements performed using Cu-K_α radiation, the maximal penetration depth is about 2 µm and for synchrotron experiments with much harder X-rays the maximal information depth τ_{eff}, approaches the half of the coating thickness ($\tau_{eff} \to D/2$) [26]. For the as-deposited coating $\sigma(\tau)$ data from Fig. A.6 indicate a relatively constant tensile stress state of approximately 0.5 ± 0.1 GPa across the coating. Unfortunately, the stress dependence in the interval $[D/2, D]$ is not accessible [26].

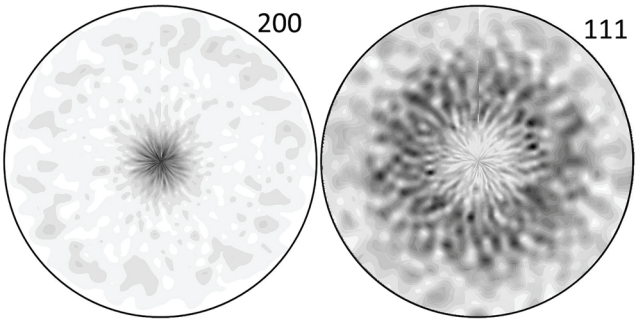

Figure A.5.: TiN 200 and 111 pole figures collected using a laboratory Rigaku X-ray diffractometer indicate a {100} fibre texture of the TiN coatings.

In case of the blasted coating, both laboratory as well as synchrotron $\sigma(\tau)$ data (Fig. A.6) indicate a stress decrease with the τ increase. In order to obtain residual stress dependencies $\sigma(z)$ in the real space for the blasted coating, it was assumed that the stress depth dependence can be approximately expressed by the exponential function [27]

$$\sigma(z) = (a + bz)e^{-cz} + d \tag{A.6}$$

where a, b, c and d are numerical constants. The transformation of Eq. (A.6) into Laplace space can be expressed as [5, 21, 22]

$$\sigma(\tau) = \frac{\int_0^D \sigma(z) e^{-z/\tau} dz}{\int_0^D e^{-z/\tau} dz} \tag{A.7}$$

By fitting the numerical parameters a, b, c and d from Eq. (A.7) to the data of the blasted sample from Fig. A.6, it was possible to evaluate residual stress profiles $\sigma(\tau)$ in Laplace space and also $\sigma_{\mathrm{L}}(z)$ in real space (Fig. A.6). $\sigma_{\mathrm{L}}(z)$ dependence was

determined by using both laboratory as well as synchrotron data (except for the three measurement points from the synchrotron experiment on the blasted sample at τ in the range of 0–2 µm). Finally both $\sigma(\tau)$ and $\sigma_{\mathrm{L}}(z)$ dependencies document an (expected) exponential decrease of the compressive residual stresses as a function of z in the blasted TiN.

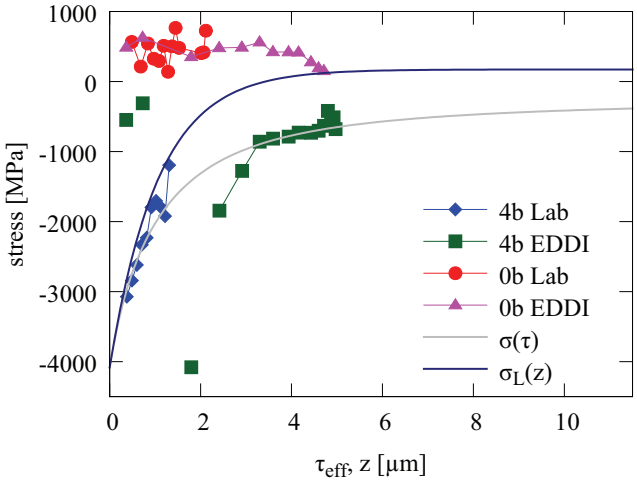

Figure A.6.: Residual stress values calculated from laboratory (Lab) and synchrotron (EDDI) data (Fig. A.4) using Eqs. (A.3–A.5) for non-blasted (0b) and blasted (4b) coatings. $\sigma(\tau)$ represents the fitted stress dependence (Eq. (A.7)) in the Laplace space in the blasted coating as a function of τ_{eff}. $\sigma(z)$ represents recalculated stress profile (Eq. (A.6)) in the real space. $\sigma_{\mathrm{L}}(z)$ and $\sigma(z)$ were determined by using both Lab and EDDI data except for the three EDDI measurement points at τ_{eff} in the range of 0–2 µm. For the non-blasted sample the stresses are relatively homogeneous across the coating.

A.3.3. Residual Stress Analysis in Real Space

Two dimensional diffraction patterns obtained from the scanning X-ray nanodiffraction experiment (Fig. A.2) were used to evaluate lattice spacing as a function of the diffraction vector $\boldsymbol{Q}(\delta)$ orientation and the coating depth. At first the Debye-Scherrer rings were integrated using the software Fit2D in order to analyse the positions of the TiN 200 reflection collected at different δ angles. In Fig. A.7, the depth development of the reflection positions $2\theta(\delta, z)$ for $\delta = 0$ and 90 ° is presented. In the case of the as-deposited (unblasted) sample, Figs. A.7 a and c document that the peak positions do not change significantly across the entire coating thickness what can be interpreted as an absence of a pronounced stress gradient. For the blasted sample, however, the peak positions move towards higher diffraction angles

for $\delta = 90\,°$ (Fig. A.7 d) and smaller diffraction angles for $\delta = 0\,°$ (Fig. A.7 b) for coating depths in the range of about 0–2 µm. This is caused by a pronounced in-plane (near surface) compressive stress which induces a coating contraction in the in-plane direction, that is a decrease of lattice spacing of crystallographic planes oriented with their normals parallel to the interface. However, the same stress causes an increase of lattice spacing of crystallographic planes oriented with their normals an angle θ with respect to the sample normal. The weak $2\theta(0, 0.5)$ increase (*cf.* Fig. A.7 b) and $2\theta(90, 0.5)$ decrease (*cf.* Fig. A.7 d) at the depths of about 0.5 µm indicate the presence of a weak stress relaxation which will be discussed further. Different broadening of the TiN 200 reflections for $\delta = 0\,°$ and $\delta = 90\,°$ indicates an anisotropic grain morphology (with needle-like crystallite shapes) and/or anisotropic strains of II. and III. order (Fig. A.7). The abrupt changes in the peaks width at depths of about 5.5 µm were caused by the change in the deposition temperature which resulted in the growth of larger crystallites at depth of about 0–5.5 µm.

In order to analyse the depth variation of crystallographic texture in the samples, intensities along TiN Debye-Scherrer rings $I(\delta, z)$ were evaluated. The three dimensional (3D) $I(\delta, z)$ data were transformed into $I(\psi, z)$ dependencies using a simple transformation from [11] linking δ and ψ angles (*cf.* Fig. A.2)

$$\cos\psi = \cos\theta\cos\delta \tag{A.8}$$

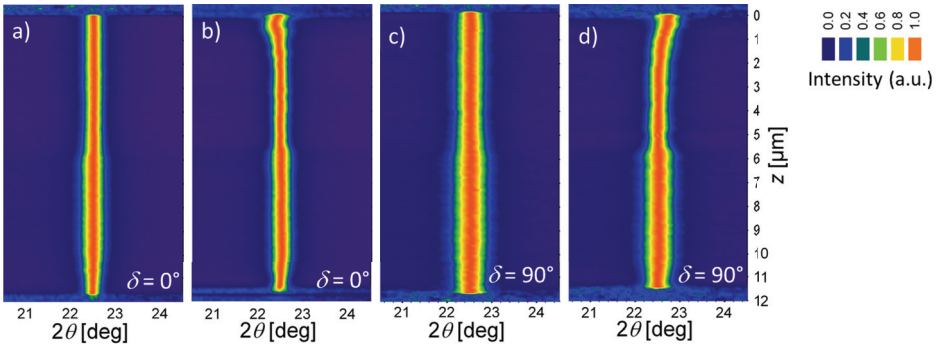

Figure A.7.: TiN 200 reflections collected at different depths from as deposited (a,c) and blasted (b,d) coatings depicted for two diffraction vector orientations $\delta = 0\,°(\psi = \theta)$ and $90\,°$(*cf.* Fig. A.2). The diffraction peak width variation across the depth is cased (i) by the blasting for depth of 0-2µm in (b,d) and (ii) by the deposition temperature change at about 5.5 µm in both samples.

Since the coatings were in-plane isotropic (Fig. A.5), the 3D data collected from the blasted sample (Fig. A.8) indicate a presence of a {100} fibre texture, in agreement with the laboratory measurements from Fig. A.5, where texture intensity

changes slightly as a function of the coating depth z. In principle, the 3D data can be used to reconstruct the orientation distribution function (ODF) for every z-position [like in [9]], what is however is out of the scope of this work.

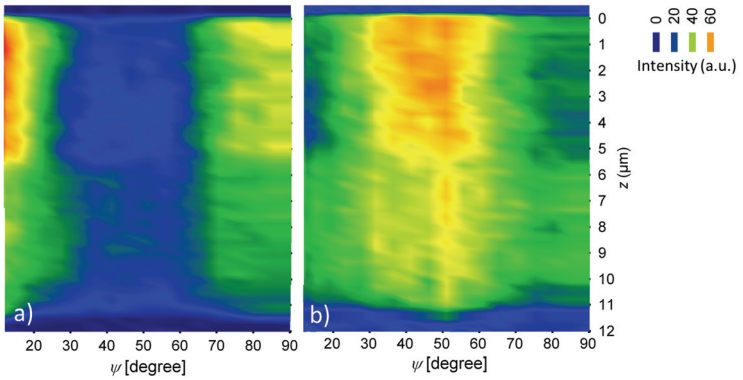

Figure A.8.: Depth variation of intensities along TiN 200 and 111 Debye-Scherrer rings in the blasted sample. In agreement with the data from Fig. A.5, the relatively strong intensities at $\psi = 10\,^\circ$ and $90\,^\circ$ for TiN 200 and $\psi \approxeq 50\,^\circ$ for TiN 111 document a presence of a $\{100\}$ fibre texture whose intensity changes as a function of the depth. The increase in the texture sharpness at depths of about 0-5.5 µm was caused by the temperature increase during the deposition.

In order to analyse residual stresses in both coatings, 3D dependencies of the lattice parameter $a(\delta, z)$ were evaluated from the position of TiN 200 reflections (Fig. A.9). The results indicate that, in the as-deposited coating, the lattice parameter does not change significantly as a function of δ at distinct depths z. In other words the slope $\partial a(\delta, z)/\partial\delta$ is relatively small. In the case of the blasted coating, however, the slope $\partial a(\delta, z)/\partial\delta$ is very pronounced for $z \to 0$ which indicates pronounced stresses in the blasted coating surface.

The 3D $a(\delta, z)$ dependencies (Fig. A.9) cannot be however automatically used to evaluate residual stresses $\sigma_{ij}(z)$ in the coatings. Due to the sample cutting, the residual stresses in the lamellae [with an intentionally selected small thickness of only 20 µm (Fig. A.2)] were partly relaxed and are not equi-biaxial any more and therefore $\sigma_{11}(z) \neq \sigma_{22}(z)$ as well as $\varepsilon_{11}(z) \neq \varepsilon_{22}(z)$. Generally when for simplicity assuming only a biaxial stress state with negligible $\sigma_{ij}(z)$, $\sigma_{33}(z)$ and $\varepsilon_{ij}(z)$ (evaluated from the TiN 200 reflections) it can be shown that for the measured $a(\delta, z)$ lattice parameters

$$\frac{a(\delta, z) - a_0(z)}{a_0(z)} = \sin^2\theta\varepsilon_{11}(z) + \cos^2\theta\,\sin\delta\,\varepsilon_{22}(z) + \cos^2\theta\cos^2\delta\,\varepsilon_{33}(z) \qquad \text{(A.9)}$$

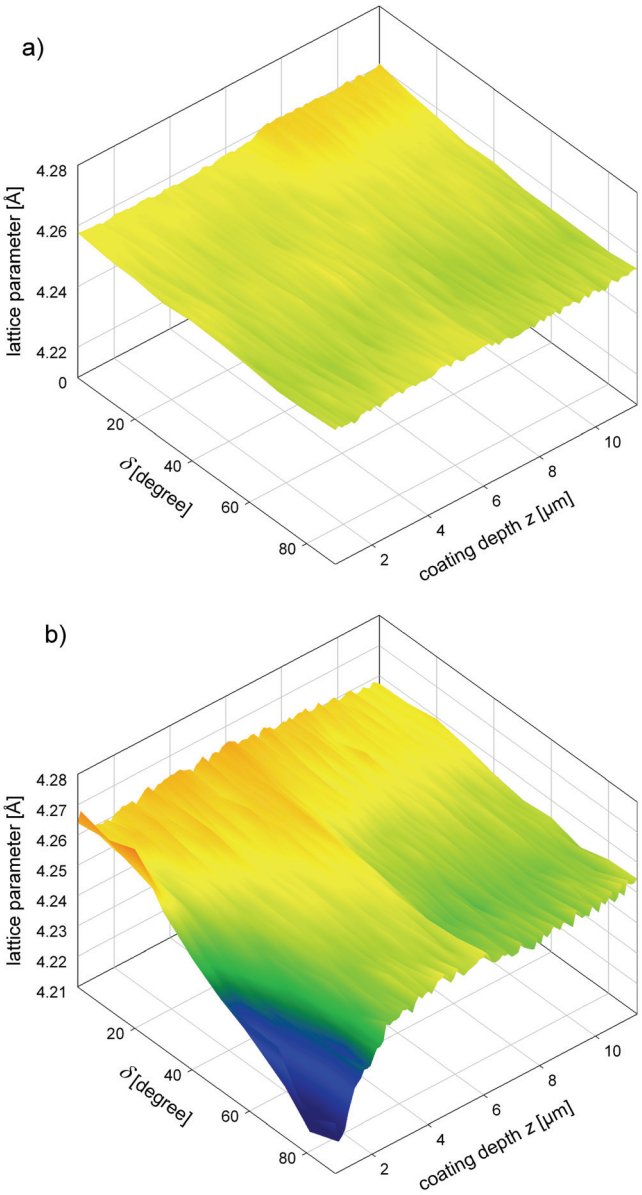

Figure A.9.: The variations of the lattice spacing $a(\delta, z)$ (evaluated from TiN 200 reflections) as a function of the coating depth and the angle δ indicate a relatively homogeneous stress state in as-deposited coating (a) and pronounced residual stresses in the blasted coating surface (b).

and

$$\frac{a(\delta,z)-a_0(z)}{a_0(z)} = \sigma_{11}\left[\frac{1}{2}S_2(hkl)\sin^2\theta + S_1(hkl)\right] + \sigma_{22}\left[\frac{1}{2}S_2(hkl)\cos^2\theta\,\sin^2\delta + S_1(hkl)\right] \quad \text{(A.10)}$$

where $a_0(z)$ are unstressed lattice parameters. For X-ray elastic constants $S_1(hkl)$ and $\frac{1}{2}S_2(hkl)$ applies in the case of a $\{100\}$ fibre texture [22]

$$\frac{1}{2}S_2 = \frac{1}{2}s_{44} \text{ and } S_1 = 2s_{12} + \left(s_{11} - s_{12} - \frac{1}{4}s_{44}\right)\frac{h^2+k^2}{h^2+k^2+l^2} \quad \text{(A.11)}$$

For small Bragg angles θ, the term $\sin^2\theta$ goes to zero and therefore Eqs. (A.9) and (A.10) can be simplified significantly. Moreover Eq. (A.10) can be converted as follows

$$\frac{\partial a(\delta,z)}{\partial \sin^2\delta} = \sigma_{22}(z)\frac{1}{2}S_2(hkl)\,a_0(z) \quad \text{(A.12)}$$

The term $\sigma_{22}(z)$ from Eq. (A.12) represents in this case the "measured" residual stress component (parallel to the long lamella y-axis Fig. A.2) which can be evaluated easily from the distortion of Debye-Scherrer rings expressed by the term $\partial a(\delta,z)/\partial\sin^2\delta$. In the case of relatively thick lamellas, where the lamella thickness L is few times of the coating thickness D, $\sigma_{22}(z)$ represents actually the depth dependence of the original equi-biaxial stress component $\sigma(z)$, which was present in the coating before cutting and therefore $\sigma_{22}(z) = \sigma(z)$ for $L \gg D$. For $L \cong D$, Eq. (A.12) can be used straightforward to evaluate original stresses in the coatings with $\sigma_{22}(z) = \sigma(z)$ only for samples where the stress relaxation across the coatings is constant, i.e. $\Delta\sigma_{11} = const.$ This is the case for coatings and thin films on ductile and soft substrates.

In the specific present case, of a lamella on stiff substrate with the thickness L comparable to the coating thickness D ($L \cong D$), strain components $\varepsilon_{ij}(z)$ as well as stress component $\Delta\sigma_{11}$ change inhomogeneously due to cutting as a function of the coating depth z. In other words, $\sigma_{11}(z)$ residual stresses relax in a considerable volume fraction of the lamella and cause a depth-dependent strain release. As a result also $\sigma_{22}(z)$ changes due to this relaxation, especially at the lamella borders (Fig. A.10).

In order to investigate the effect of the residual stress relaxation due to sample cutting and to reconstruct the original stress state $\sigma(z)$ in the blasted sample from $\sigma_{22}(z)$ obtained from the nanodiffraction experiment (Eq. (A.12)), a finite element

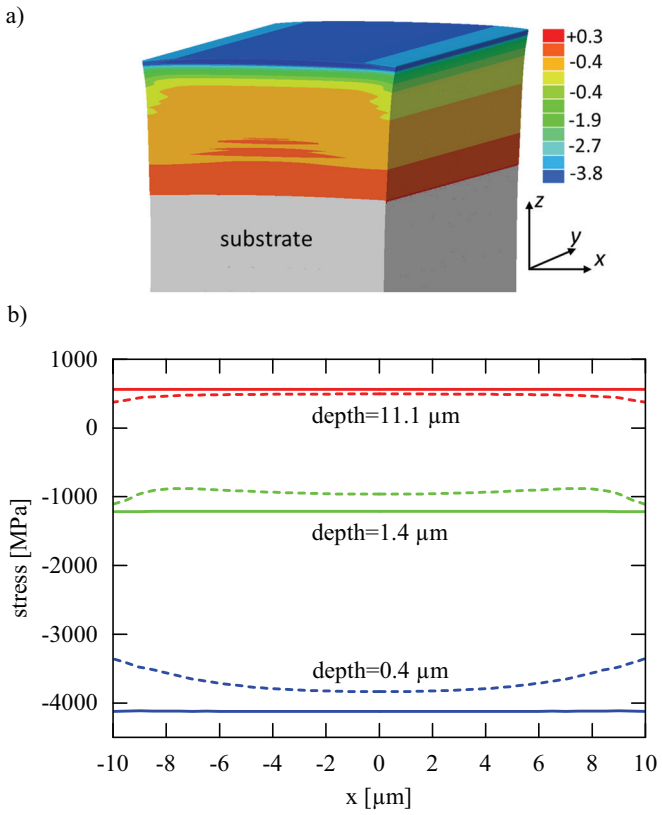

Figure A.10.: A FEM model documents a relaxation of $\sigma_{11}(z)$ residual stresses (in GPa) at the lamella cross-section due to sample cutting (a). In (b) solid and dashed lines document the $\sigma_{11}(z)$ stress magnitude along the x-axis at different coating depths for uncut and relaxed lamellae. One can observe that at the interface the relaxation is minimal whereby at the surface the relaxation at the lamellae borders is very pronounced.

model (FEM) was set up in the software package ABAQUS. The model in which the equi-biaxial residual stress profile was applied to the coating as predefined field consisted of two steps. In the first step the boundary conditions were chosen in a way so that the coated sample behaved like having infinite extension in the x and y-directions. The sample was allowed to expand and curve in order to find its mechanical equilibrium. In the second step the boundary conditions were modified so that in the model a sample with 20 µm thickness in the x-direction, like in the nanobeam experiment, was formed. In a first simulation, the stress profile obtained from the nanobeam experiment was applied to the uncut sample and the relaxation after the cut was simulated. This gave a first impression of the relaxation taking place when the lamella is cut. After that the simulation was integrated in an iterative

optimization procedure altering the stress state applied as predefined field until the stress state in the 20 µm thick lamella matched with $\sigma_{22}(z)$ obtained from the nanobeam experiment. Finally the corrected biaxial stress distribution $\sigma_{\mathrm{FEM}}(z)$ was obtained from the simulation step modelling the uncut sample. The mechanical behaviour of the TiN coating was modelled using Young's modulus and Poisson's number of 428 GPa and 0.2 from [25].

In Fig. A.11, evaluated residual stresses $\sigma_{22}(z)$ obtained from the X-ray nanobeam experiment, stresses obtained from FEM procedure $\sigma_{\mathrm{FEM}}(z)$ and stresses obtained from the Laplace technique $\sigma_{\mathrm{L}}(z)$ (Fig. A.6) are presented for the blasted coating. Qualitatively, $\sigma_{22}(z)$, $\sigma_{\mathrm{FEM}}(z)$ and $\sigma_{\mathrm{L}}(z)$ indicate a relatively large magnitude of compressive residual stresses in the blasted coating near the surface and an exponential stress decrease towards the substrate. The comparison of $\sigma_{\mathrm{FEM}}(z)$ and $\sigma_{22}(z)$ documents the intensity of the stress relaxation which is significant especially in the coating upper region, in agreement with Fig. A.10. Remarkably, the nanodiffraction data indicate a compressive stress maximum at $z = 0.5$ µm. Its presence is also visible also in the raw data from Fig. A.7 and A.9. This type of stress gradient has also been reported from simulations of the shoot peening process [27]. For the as-deposited coating, the stresses are tensile and relatively constant at about 0.5 ± 0.1 GPa.

In the $\sigma_{\mathrm{L}}(z)$ dependence such local stress variation obviously cannot be resolved, which is due to the form of Eq. (A.6) as well as due to the principle of the method itself. The remarkable scattering of the first three points in the τ range of 0–2 µm obtained from the synchrotron experiment on the blasted sample (Fig. A.6) however indicates some irregular stress-depth behaviour, which could be caused by the compressive stress maximum at $z = 0.5$ µm (Fig. A.11).

A.4. Discussion

The aim of this chapter is to discuss advantages and disadvantages of Laplace and cross-sectional XRD approaches. Intentionally, a coating with a relatively simple stress depth profile was chosen in order to compare both approaches.

The main advantage of the Laplace approach is obviously no sample preparation and a possibility to perform the experiments in the laboratory. The main restriction of the Laplace technique is the necessity to perform an inverse Laplace transformation of the measured $\sigma(\tau)$ profile. For the transformation, the functional dependence of the residual stress in the real space $\sigma(z)$ must pre-selected. In general, there are infinitely many $\sigma(z)$ profiles in real space which would result in the same

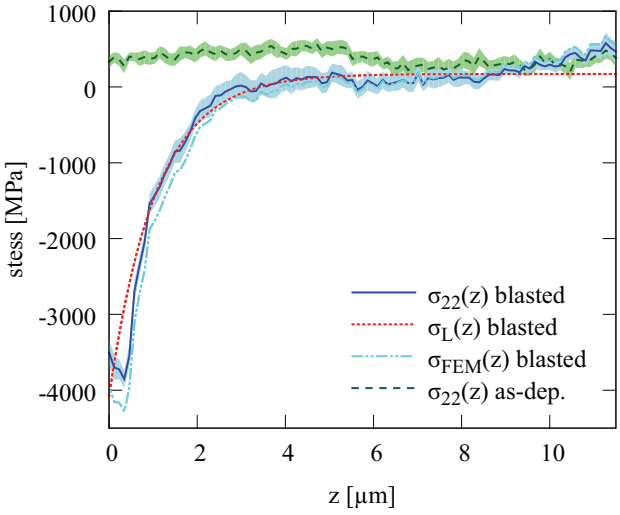

Figure A.11.: Residual stress gradients in the blasted coating evaluated using the X-ray nanodiffraction approch $\sigma_{22}(z)$ and Laplace method $\sigma_{\mathrm{L}}(z)$. $\sigma_{\mathrm{FEM}}(z)$ represents the recalculated stress profile using the FEM model. The stresses $\sigma_{22}(z)$ in the as-deposited coating show a small variation across the thickness. The filled bands behind $\sigma_{22}(z)$ experimental dependencies document the measurement errors. The relatively small tensile stress increase in both samples at the depth of about 5.5 µm was caused by the temperature increase during the deposition and by the subsequent thermal tensile stress increase.

$\sigma(\tau)$ dependence in the Laplace space and vice versa. Moreover the often unknown depth dependence of unstressed lattice parameter $d_0(hkl, z)$ and/or mass attenuation coefficient μ, caused e.g. by chemical gradients, coating grain morphology and/or density variations, present also a serious problem for the $\sigma(z)$ recalculation. The experimental determination of $d_0(hkl, z)$ in nanocrystalline and/or graded thin films and coatings from X-ray elastic constants is very questionable. Practically, the Laplace technique can be used to analyse only relatively simple (monotonous) stress profiles $\sigma(z)$ and is not sensitive to local stress variation. Given by the method nature, an analysis of oscillating or step-like stress fields [9] is practically impossible.

In the case of the cross-sectional nanobeam approach, no assumptions about the existing stress profile have to be made. The novel technique allows the characterization of very complex stress gradients with step-like or even oscillating depth profiles. Moreover, the powerful approach can be used to evaluate for the first time not only stress but also representative microstructure (texture, crystallite size and defect density) and phase gradients in thin films and coatings. In this way, also origins of stress evolution across the thickness can be studied and correlated with the

deposition conditions (as in the present case) or with the thin film thermal and/or loading history. It can be expected that the novel approach will allow the development of depth-dependent grain interaction models for thin films and coatings whose application will be necessary in order to evaluate stresses in samples with strong texture gradients [9].

The main disadvantages of the novel approach are sample preparation, the need for a synchrotron beamline providing a X-ray nanobeam, a relatively extensive data treatment and a necessity to use a FEM model to recalculate the original stresses from the measured data in the case of thin lamellae structures, as in the present case. Currently, however, it is not necessary to perform the residual stress characterization only on thin lamellae with $L \cong D$. High-energy synchrotron X-ray beams and their high brilliance allow performing the measurements also on lamellae with thickness L in the rage of 100 µm or even more where the stress relaxation on both sides of the lamella (Fig. A.10) is practically negligible.

In future it can be expected that novel developments in focusing X-ray optics and beamline instrumentation with beam sizes in the sub-100 nm range will result in the possibility of performing even more local characterization of stress gradients. In that case, the application of pencil X-ray nano-beams for coatings and thin films with plain interfaces [28, 29] will rapidly increase in importance in order to guarantee the sufficient diffraction statistics, especially when looking for representative microstructure data.

A.5. Acknowledgements

We acknowledge the Helmholtz-Zentrum Berlin – Electron storage ring BESSY II for allocation and provision of synchrotron radiation at the beamline EDDI. We are very grateful to Prof. Christoph Genzel and Dr. Manuela Klaus for the assistance The research leading to these results has received also a funding from the European Community's Seventh Framework Programme (FP7/2007-2013) under grant agreement № 226716. Financial support by the Austrian Federal Government and the Styrian Provincial Government within the research activities of the K2 Competence Centre on "Integrated Research in Materials, Processing and Product Engineering" operated by the Materials Center Leoben Forschung GmbH in the framework of the Austrian COMET Competence Centre Programme, is gratefully acknowledged.

Bibliography to paper A

[1] M. Ohring. *Materials Science of Thin Films. Deposition and Structure.* Academic Press, London, 2nd edition, 2002.

[2] A. Cavaleiro and J. T. M. De Hosson, editors. *Nanostructured Coatings.* Springer, New York, 2006.

[3] I. C. Noyan and J. B. Cohen. *Measurement by Diffraction and Interpretation.* Springer, 1987.

[4] V. Hauk. *Structural and Residual Stress Analysis by Nondesdestructive Methods.* Elsevier, 1997.

[5] M. Birkholz. *Thin Film Analysis by X-Ray Scattering.* WILEY-VCH, 2006.

[6] D. Faurie, O. Castelnau, R. Brenner, P. O. Renault, E. Le Bourhis, and P. Goudeau. *J Appl Crystallogr*, 42(6):1073–1084, DEC 2009. doi:10.1107/S0021889809037376.

[7] V. Hauk and H. Dölle. *Härterei-Techn. Mitt.*, 34:272, 1979.

[8] C. Genzel. *Phys Status Solidi A*, 156(2):353–363, 1996. doi:10.1002/pssa.2211560213.

[9] J. Keckes, M. Bartosik, R. Daniel, C. Mitterer, G. Maier, W. Ecker, J. Vila-Comamala, C. David, S. Schoeder, and M. Burghammer. *Scripta Mater*, 67(9): 748–751, 2012. doi:10.1016/j.scriptamat.2012.07.034.

[10] M. Bartosik, R. Daniel, C. Mitterer, I. Matko, M. Burghammer, P. Mayrhofer, and J. Keckes. *Thin Solid Films*, 542:1–4, 2013. doi:10.1016/j.tsf.2013.05.102.

[11] F. Heidelbach, C. Riekel, and H. R. Wenk. *J Appl Crystallogr*, 32:841–849, 1999. doi:10.1107/s0021889899004999.

[12] Nist: National institute of standards and technology http://physics.nist.gov/physrefdata/ffast/html/form.html. URL `http://physics.nist.gov/PhysRefData/FFast/html/form.html`.

[13] C. Genzel, I. A. Denks, J. Gibmeler, M. Klaus, and G. Wagener. *Nucl Instrum Meth A*, 578(1):23–33, 2007. doi:10.1016/j.nima.2007.05.209.

[14] C. Genzel, C. Stock, and W. Reimers. *Mat Sci Eng A*, 372(1-2):28–43, May 2004. doi:10.1016/j.msea.2003.09.073.

[15] C. Riekel, M. Burghammer, and R. Davies. *IOP C Ser Mat Sci Eng*, 14(012013), 2010. doi:10.1088/1757-899x/14/1/012013.

[16] S. Gorelick, V. A. Guzenko, J. Vila-Comamala, and C. David. *P Soc Photo-opt Ins*, 21(29), 2010. doi:10.1088/0957-4484/21/29/295303.

[17] C. G. Schroer, M. Kuhlmann, U. T. Hunger, T. F. Gunzler, O. Kurapova, S. Feste, F. Frehse, B. Lengeler, M. Drakopoulos, A. Somogyi, A. S. Simionovici, A. Snigirev, I. Snigireva, C. Schug, and W. H. Schroder. *Appl Phys Lett*, 82(9): 1485–1487, 2003. doi:10.1063/1.1556960.

[18] A. P. Hammersley, S. O. Svensson, M. Hanfland, A. N. Fitch, and D. Häusermann. *High Pressure Res*, 14:235–248, 1996.

[19] J. Keckes. *J Appl Crystallogr*, 38(2):311–318, 2005. doi:10.1107/S0021889805001044.

[20] P.-O. Renault, E. Le Bourhis, P. Villain, P. Goudeau, K. Badawi, and D. Faurie. *Appl Phys Lett*, 83(3):473–475, 2003. doi:10.1063/1.1594280.

[21] P. Scardi and Y. H. Dong. *J Mater Res*, 16:233–242, 2001. doi:10.1557/JMR.2001.0036.

[22] C. Genzel. *Phys Status Solidi A*, 159(2):283–296, 1997.

[23] H. Dölle. *J Appl Crystallogr*, 12(6):489–501, 1979. doi:10.1107/s0021889879013169.

[24] P. V. Houtte and L. D. Buyser. *Acta Metallurgica et Materialia*, 41(2):323–336, 1993. doi:10.1016/0956-7151(93)90063-X.

[25] W. Kress, P. Roedhammer, H. Bilz, W. D. Teuchert, and A. N. Christensen. *Phys Rev B*, 17(1):111–113, 1978. doi:10.1103/PhysRevB.17.111.

[26] C. Genzel. *Mater Sci Technol*, 21(1):10–18, 2005. doi:10.1179/174328405X14100.

[27] T. Hong, J. Y. Ooi, and B. Shaw. *Eng Fail Anal*, 15(8):1097–1110, December 2008. doi:10.1016/j.engfailanal.2007.11.017.

[28] C. Krywka, H. Neubauer, M. Priebe, T. Salditt, J. Keckes, A. Buffet, S. V. Roth, R. Doehrmann, and M. Mueller. *J Appl Crystallogr*, 45:85–92, February 2012. doi:10.1107/S0021889811049132.

[29] C. Krywka, J. Keckes, S. Storm, A. Buffet, S. Roth, R. Döhrmann, and M. Müller. *J Phys Conf Ser*, 425(072021), 2013. doi:10.1088/1742-6596/425/7/072021.

B

X-ray Nanodiffraction reveals Stress Distribution across an Indented Multilayered CrN-Cr Thin Film

M. Stefenelli[a], R. Daniel[b], W. Ecker[a], D. Kiener c, J. Todt[e], A. Zeilinger[a], C. Mitterer[b], M. Burghammer[d] and J. Keckes[c]

[a]Materials Center Leoben Forschung GmbH, Leoben, Austria

[b]Department of Physical Metallurgy and Materials Testing , Montanuniversität Leoben, Austria

[c]Department of Materials Physics, Montanuniversität Leoben, Austria

[d]ESRF, Grenoble, France

Abstract

In order to understand the indentation response of thin films with nonhomogeneous microstructures, it is necessary to characterize local deformation fields and microstructural changes around the indenter imprint. In this work, residual stress fields across a wedge-indented nanocrystalline CrN-Cr thin film with a respective sublayer thickness of 500 and 250 nm and an overall thickness of 3 µm on a steel substrate are characterized ex-situ using cross-sectional synchrotron X-ray nanodiffraction with

a spatial resolution of 100 nm. In the as-deposited multilayer, residual stresses of about -3.5 and -1 GPa in the CrN and Cr sublayers, respectively, are found. After the indentation, a complex stress distribution across the film cross-section with stress peaks in the range from -10 to 2 GPa was observed. In agreement with the results from a finite element model, the formation of the residual stresses can be interpreted by the plastic deformation of the Cr sublayers and the steel substrate in conjunction with a linear elastic response of CrN. During the indenter unloading, the plastically deformed materials hinder the full relaxation of the indentation-induced high compressive and tensile stresses in linear elastic deformed brittle regions and the stresses remain partly conserved. The ductile Cr sublayers serve as a fundamental stabilizing component which ensures that the stress peaks do not cause the film rupture or delamination but the damage remains arrested between the plastically deformed Cr sublayers and the substrate. The encapsulation of the highly stressed and damaged regions, enhanced by the excellent sublayer adhesion, serves as the decisive and stabilizing component to the multilayer mechanical integrity during and after the indentation.

B.1. Introduction

Physical properties of nanocrystalline thin films are decisively influenced by their small crystallite size, typically below 100 nm, giving rise to a variety of size effects [1, 2], a high volume fraction of grain boundaries [3] and complex microstructure [4] which originate (i) from the gradual film evolution during growth [5–7] and/or (ii) from nanoscale modulations (e.g. multilayers) achieved by applying dedicated deposition recipes [8, 9]. By performing microstructural design, mechanical properties such as hardness, fracture toughness and Young's modulus can be effectively controlled in the films [10].

Indentation has become a common technique to investigate mechanical properties of thin films and near-surface regions. Hardness values and force-displacement dependencies can serve as a valuable indicator of the global material mechanical behaviour. In the case of nanocrystalline thin films with non-homogeneous microstructure, it is however not trivial to understand how the integral values of hardness and reduced modulus relate to the distinct microstructural features embedded in the film, such as soft and hard sublayers, precipitates and grain boundaries. The main challenge here is the missing information on the local deformation behaviour of those microstructural features. Despite numerous modelling approaches developed to analyse deformation and rotation fields, plastic flow and material displacement during the indentation process [11], most of the models suffer from the poor knowledge of size-dependent material properties like flow stress or crack propagation behaviour at interfaces. Therefore in order to understand deformation behaviour of nanomaterials with complex microstructures, it is necessary to understand microstructural changes, deformation fields and crack behaviour accompanying the indentation at sub-micrometre scale.

There exist already a limited number of experimental studies of rotation and deformation fields on indented samples performed using electron microscopy, X-ray diffraction and Raman spectroscopy [12–15]. Local orientation changes in Cu single crystals were studied using electron backscatter diffraction documenting that the observed flow stresses correlate well with the crystal misorientation maps, which further scale with the indent size [14, 15]. Numerous Laue X-ray micro-diffraction experiments [12, 16, 17] were used to analyse deformation behaviour in small crystalline domains with the focus especially on the determination of elasto-plastic interactions e.g. in copper single crystals, coarse-grained Inconel and in micro-lamellae NiAl-Cr eutectic alloys with strain resolution down to $0.3 \times 0.4\,\mu m$. Additionally, X-ray topography and Raman spectroscopy studies [18] have been performed to characterize

strains in monocrystalline silicon with a resolution of about 1 µm. Using a spatial resolution of 100 µm, monochromatic high-energy X-ray diffraction [19] was used to characterize the deformation field of a scratch introduced into a steel sample.

Recently, a novel cross-sectional X-ray nanodiffraction technique [20] providing a spatial resolution of about 100 nm was introduced. The unique approach has been used to characterize microstructure and strain fields position-resolved across cross-sections of thin films and coatings and possesses also a potential to analyse local indentation-induced changes across thin films.

The aim of this work is to perform a position-resolved characterization of deformation fields in a wedge-indented nanocrystalline multi-layered CrN-Cr thin film on a steel substrate by measuring the X-ray elastic strain distribution over the cross-section using X-ray nanodiffraction with a beam size of 100 nm. The motivation is to evaluate residual elastic strain and residual stress distributions in soft Cr and hard CrN sublayers after the indentation and to correlate the experimental data with a finite-element model (FEM).

B.2. Materials and Experimental Details

B.2.1. Thin Film Deposition

For this study, a CrN-Cr multilayer thin film comprising 8 sublayers with respective thicknesses of 500 and 250 nm on a steel substrate was prepared. The film was sputtered using a 145 mm Cr target produced by means of powder metallurgy. Before starting the deposition process, the chamber was evacuated to 10^{-3} Pa, the substrate heated to 350 °C and plasma etched. The film was then deposited at 350 °C using a constant target power of 6 kW and a total pressure of 1 Pa. The Cr sublayers were deposited in a pure Ar atmosphere and an applied bias voltage of −40 V, whereas the CrN layers were grown in an $Ar + N_2$ atmosphere applying a bias voltage of −120 V. The N_2 partial pressure was adjusted to 0.25 Pa with a capacitive gauge. The resulting over-all thickness of the film was 3 µm.

B.2.2. Sample Indentation

From the thin film sample, a lamella with a width of $L = 50$ µm was fabricated using focused ion beam milling (Fig. B.1). The lamella was then indented using an ASMEC nano-indentation system implemented in a scanning electron microscope LEO-1525 (SEM) applying a maximal force of 220 mN [21]. The indenter was equipped with a wedge-shaped diamond tip having an opening angle of 60° and

a wedge length of 60 µm provided by Synton, Switzerland. The wedge shape was chosen to introduce a notch ranging over the entire lamella width to a depth of about 1.4 µm. During the indentation, the whole lamella deflected elastically under the indenter load and therefore the indenter displacement and force data recorded by the nano-indentation system are unfortunately not directly interpretable. The video of the indentation experiment and the force-displacement data are provided as a supplementary material.

B.2.3. X-ray Nanodiffraction Analysis of Strains

The wedge indentation into the CrN-Cr film resulted in the formation of complex triaxial residual strain and stress fields $\varepsilon_{ij}(x, y, z)$ and $\sigma_{ij}(x, y, z)$ (Fig. B.1). Due to the specific experimental conditions and the sample nature, diffraction data obtained from the nanodiffraction experiment were used to quantify only volume-averaged and selected residual strain and stress tensor components applying some assumptions and simplifications. The residual strain in the film before the indentation was supposed to be triaxial with negligible shear strain components

$$\varepsilon_{ii}(x, y, z) \neq 0, \varepsilon_{ij}(x, y, z) \simeq 0 \tag{B.1}$$

and the stress state was supposed to be equi-biaxial with

$$\sigma_{11}(x, y, z) = \sigma_{22}(x, y, z), \sigma_{ij}(x, y, z) \simeq 0 \text{ and } \sigma_{33}(x, y, z) \simeq 0. \tag{B.2}$$

After the indentation, the dedicated lamella geometry with the notch spanning across the whole lamella width allowed determining volume-averaged local residual strain fields $\varepsilon_{22}(y, z)$ and $\varepsilon_{33}(y, z)$ in y-z-plane, which were relatively homogeneous along the x axis, using the X-ray beam oriented parallel to the wedge imprint Fig. B.1). This means the strain relaxations at the lamella borders [22] as well as the strain variation along the x axis were neglected for simplicity. The experimental values of $\varepsilon_{22}(y, z)$ and $\varepsilon_{33}(y, z)$ were then used to calculate the in-plane stress component $\sigma_{22}(y, z)$ acting along the y axis. It should be noted that the $\sigma_{22}(y, z)$ is valid only for negligible values of $\sigma_{33}(y, z) \simeq 0$ and $\sigma_{ij}(y, z) \simeq 0$.

The experiment was conducted at the nanofocus extension of the ID13 beamline of the European Synchrotron Radiation Facility (ESRF) in Grenoble, France, using the energy of $E = 14.9$ keV and the setup described in Refs. [20, 22]. The mesh-scan at the thin film cross-section with an area of 10×7 µm was performed by moving the sample in y- and z-directions with a step size of 100 nm using a synchrotron beam of

100 nm in diameter Fig. B.1). 7171 two-dimensional (2D) diffraction datasets with a resolution of 2048 × 2048 pixels each were collected by a CCD detector located at a distance of 69 mm from the sample.

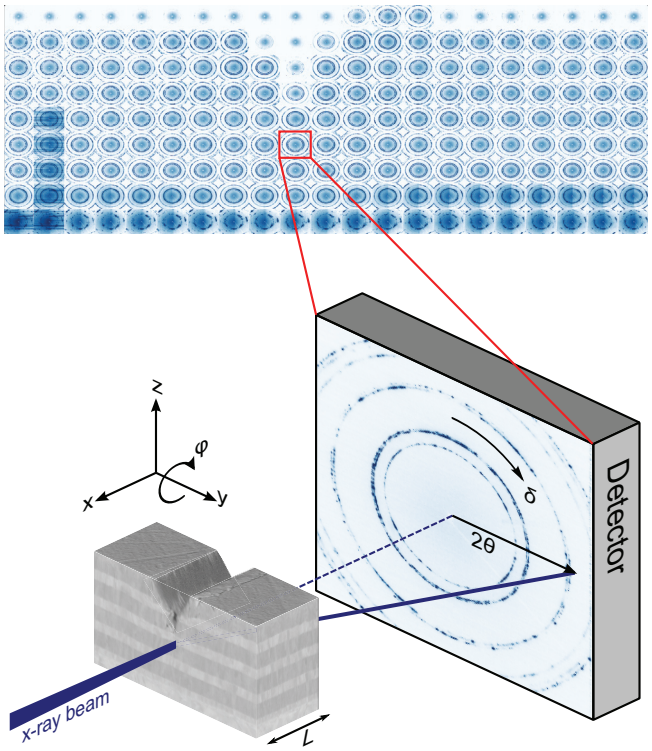

Figure B.1.: A schematic setup of the cross-sectional X-ray nanodiffraction experiment. By moving the lamella along y and z-direction with a step of 100 nm, 7171 two-dimensional diffraction data were recorded by a 2D detector from an area of 10×7 µm using a X-ray beam of 100 nm in diameter. The composite image shows the 2D data where the number of frames was reduced by a factor of about five.

The diffraction data were processed using PyFAI [23, 24] by evaluating the Bragg's angles 2θ of CrN 111 and the Cr 200 reflections as a function of the azimuthal angle δ of the Debye-Scherrer rings. The lattice parameter dependence on the strain components $\varepsilon_{ii}(y,z)$ can be expressed as follows

$$\begin{aligned} \frac{a(y,z) - a_0(y,z)}{a_0(y,z)} &= \sin^2\theta\,\varepsilon_{11}(y,z) + \cos^2\theta\sin^2\delta\,\varepsilon_{22}(y,z) \\ &\quad + \cos^2\theta\cos^2\delta\varepsilon_{33}(y,z) \end{aligned} \tag{B.3}$$

where $a_0(y,z)$ represents the unstressed lattice parameter averaged along the

lamella width and θ is the Bragg angle (Fig. B.1). Since $a_0(y,z)$ is usually not known [22], the dependence of the lattice parameter a on δ, written as $a(y,z,\delta)/\sin^2\delta$, representing the Debye-Scherrer ring ellipticity at the sample position y and z, can be expressed as follows

$$\frac{\partial a(y,z,\delta)}{\partial \sin^2\delta} = a_0(y,z)\cos^2\theta\left(\varepsilon_{22}(y,z) - \varepsilon_{33}(y,z)\right) \tag{B.4}$$

where $\varepsilon_{22}(y,z)$ and $\varepsilon_{33}(y,z)$ are in-plane and out-of-plane strain components. Eq. (B.4) thus indicates that the in-plane strain component $\varepsilon_{11}(y,z)$ does not affect the ellipticity of the Debye-Scherrer ring. Under the assumption of $\sigma_{33}(y,z) \simeq 0$ and $\sigma_{ij}(y,z) \simeq 0$, the measured elastic strains can be used to calculate the in-plane residual stress $\sigma_{22}(y,z)$ in the film according to [22],

$$\frac{\partial a(y,z,\delta)}{\partial \sin^2\delta} = a_0(y,z)\cos^2\theta\,\frac{1}{2}S_2^{hkl}\,\sigma_{22}(y,z) \tag{B.5}$$

where $\frac{1}{2}S_2^{hkl}$ represents the actual X-ray elastic constant of the material. In the present case, the $\frac{1}{2}S_2^{hkl}$ values of 4.446×10^{-6} MPa-1 [25] and 3.910×10^{-6} MPa-1 [26] were used for the CrN 111 and Cr 200 reflections, respectively. The stress values of $\sigma_{22}(y,z)$ were determined with an accuracy better than 15 %. Again also Eq. (B.5) indicates that the ellipticity of Debye-Scherrer ring is independent of the stress component $\sigma_{11}(y,z)$.

B.3. Modelling of the Deformation Field

In order to better understand the local deformation resulting in the residual stresses in the structure, a 2D FEM model was set up. The model consisted of the previously described CrN-Cr multilayer thin film and the steel substrate. In order to avoid influences from the boundary conditions in the region of interest, the width of the model was set to 20 µm and the height of the steel substrate was set to 37 µm. The displacement at the left and right boundary perpendicular to the thin film was fixed in the y-direction and the displacement at the bottom of the substrate parallel to the thin film was fixed in the z-direction. In the out-of-plane direction, generalised plane strain conditions were assumed. The indenter was modelled as a rigid surface. The wedge of the indenter had, as in the experiment, an opening angle of 60° and for the sake of numerical stability a radius of 0.3 µm at its tip was modelled. The contact between the indenter and the sample was simulated using a node-to-surface contact condition provided by the commercial software package ABAQUS. The contact was assumed to be frictionless. The total number of elements in the model was about

8000 and the element size in the area of interest containing the thin film layers and the first 1.5 µm of the substrate is 0.05 µm in height with an aspect ratio of 2. The elements in the substrate were coarsened with increasing distance from the film. Elements with quadratic shape functions and reduced integration (CPEG8R) were used. The initial residual stresses state was set to the values obtained from the nanodiffraction experiment. The Young's modulus and the Poisson's ratio for CrN were 320 GPa and 0.25, respectively [9, 27]. For Cr the Young's modulus was 300 GPa and the Poisson's ratio was 0.2 [9, 27]. The yield limit of Cr was assumed to be 3000 MPa with a linear hardening up to 8900 MPa at 10 % plastic deformation. The elastic constants of the ferritic steel were 210 GPa for Young's modulus and 0.28 for Poisson's ratio. The flow curve used for the ferritic steel was starting at 180 MPa with a nonlinear hardening up to 450 MPa at 10 % plastic strain. For both Cr and ferritic steel J2 plasticity was used. Since the indenter displacement recorded by the nano-indenter system was not representative due to the high compliance of the sample and the mounting system, a maximal indenter displacement of 2 µm was used. After loading the indenter was moved back to its initial position in order to unload the sample. For the sake of simplicity, the crack formation in CrN was neglected in the model.

B.4. Results and Discussion

A scanning electron micrograph (SEM) of the indented lamella is presented in Fig. B.2. The lamella was plastically deformed with the notch tip ending approximately in the second Cr sublayer from the top and there was a material pile-up on the right side of the indent . The asymmetric pile-up and the imprint indicate that the indentation was not performed in a symmetric mode and the indenter tip was slightly tilted with respect to the film normal (Fig. B.2). There are no cracks visible at the film cross-section and in the substrate region after the indentation. The crack propagation in the brittle CrN [28] was obviously hindered by the presence of ductile Cr sublayers which decisively influenced the failure mechanism in the ductile-brittle system and absorbed the excessive plastic deformation.

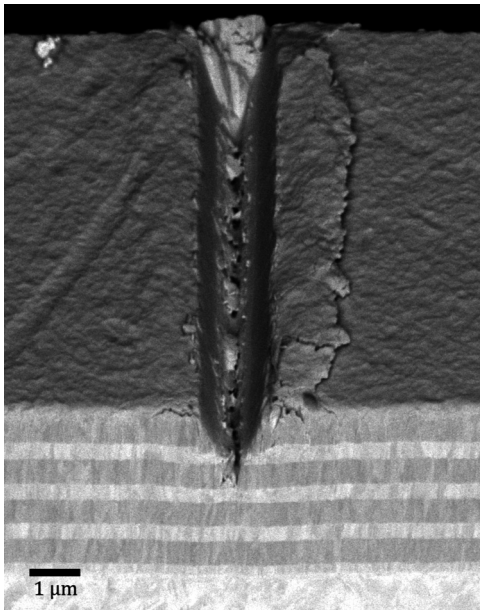

Figure B.2.: A scanning electron micrograph of the indented multi-layered CrN-Cr film on a polycrystalline steel substrate. The indent is 0.9 µm deep and the crack extends another 0.55 µm. CrN and Cr sublayers thickness was 0.5 and 0.25 µm and the lamella width was 50 µm. The imprint asymmetry was caused by a slight left tilt of the indenter tip with respect to the film normal.

Before the nano-diffraction data were collected, the X-ray beam was aligned parallel to the multilayer structure by performing a set of absorption scans, whereby a maximal contrast between the signal from the CrN and Cr sublayers was achieved using a sample tilt φ around the y-axis (Fig. B.1). For this purpose, a point detector was used to monitor the intensity of the primary beam behind the sample. In the two dimensional absorption scan of the indented film in Fig. B.3, the bending of bright and dark CrN and Cr sublayers, respectively, indicates that a considerable portion of the plastic deformation was absorbed by producing sublayers waviness and the material pile up. Complementary to the SEM micrograph in Fig. B.2, also the absorption data suggest that the cracking at the notch tip and/or delamination effects between the film and the substrate or between the Cr and CrN sublayers were negligible, as observed by others [29–31]. One can expect that small cracks were formed in the film volume[29, 31] but did not penetrate through the whole film width. One reason for the missing cracks is also a relatively small substrate curvature under the indent which was reported to be the main driving force for the cracking in indented multilayered thin films [31, 32].

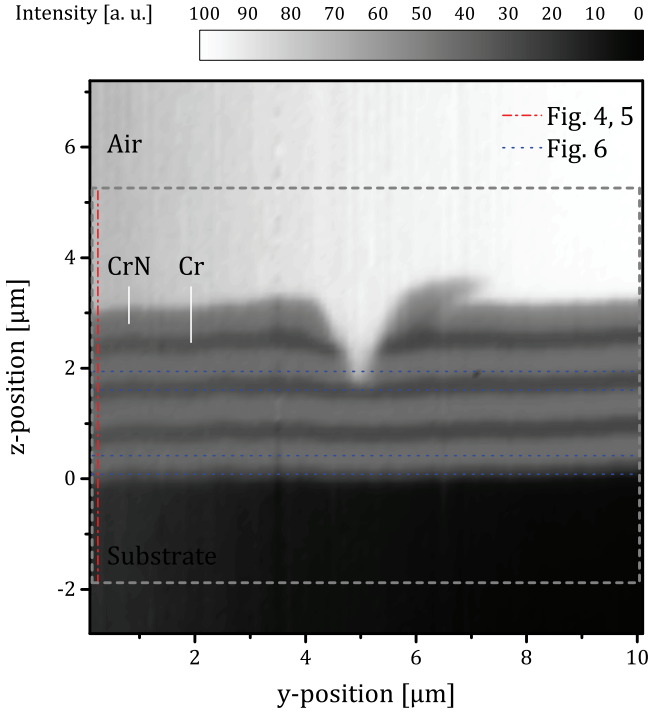

Figure B.3.: A two dimensional X-ray absorption scan of the indented film on an area of $10 \times 10\,\mu m^2$ indicating the presence of CrN and Cr sublayers on the steel substrate. The absorption contrast was used to align the beam parallel to the CrN-Cr interfaces. The diffraction data for 2D stress analysis (in Fig. B.7) were collected from the dashed area. The data from a vertical scan used for the phase (in Fig. B.4) as well as the residual stress (in Fig. B.5) analysis in an unreformed area and lateral scans (in Fig. B.6) across the imprint were collected along the dash-dotted and the dotted lines.

After the sample interfaces were aligned parallel to the beam axis, diffraction data were collected by moving the sample along y- and z-axis as indicated in Fig. B.3. The data were used to extract diffraction scans, i.e. diffraction intensity as a function of the Bragg's angle 2θ, for different orientations of the diffraction vector. In a representative phase-depth plot in Fig. B.4, CrN and Cr diffraction peaks collected from an undeformed sample region show the phase distribution across the film cross-section and substrate indicating the excellent sample alignment.

The diffraction data collected from the undeformed sample region (along the dash-dotted line in Fig. B.3) were used to evaluate in-plane stresses $\sigma_{22}\,(y = 0, z)$ in CrN and Cr sublayers, representing actually the equi-biaxial stress state in the as-deposited thin film using Eq. (B.5). The compressive stresses observed in both CrN and Cr can be attributed to the intensive ion-bombardment during film growth resulting in compressive intrinsic stresses [9] and to the specific mismatches of the

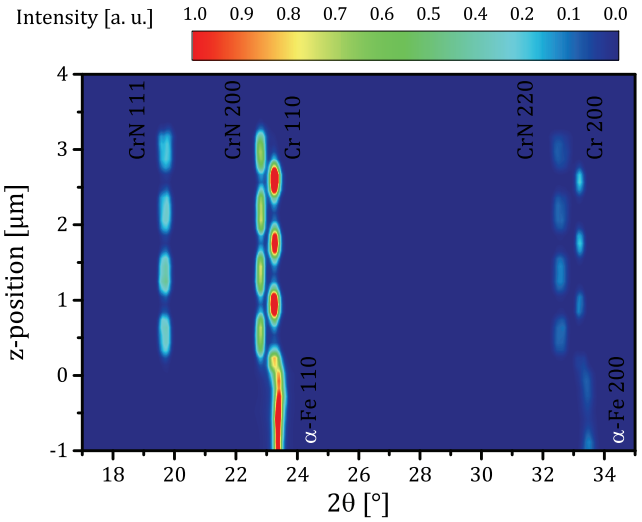

Figure B.4.: An exemplary phase-depth plot with CrN, Cr and substrate (α-Fe) peaks indicate the separation of the phases in the film/substrate system. The data were obtained by 2θ integration of the Debye-Scherrer rings (in the range from 0 to 360 degrees) and were collected along the dash-dotted line at the very left side of the scanned area ($y = 0$ in Fig. B.3), about 5 µm from the wedge centre in the undeformed region.

coefficients of thermal expansion of CrN, Cr and substrate with $\alpha_{\text{substrate}} > \alpha_{\text{Cr}} > \alpha_{\text{CrN}}$ which result in the formation of compressive thermal stresses after the sample cooling down from the deposition temperature as extensively discussed in Ref. [33].

The results in Fig. B.5 document that the compressive stresses in the Cr sublayers decrease as a function of the distance from the substrate. This effect can be interpreted by the crystallite size increase across the Cr sublayers towards the surface in the sublayers with columnar grain morphology [9], as indicated also by a (not-presented) simultaneous decrease of full width of half maximum (FWHM) of Cr 200 peaks towards the surface. In the top CrN sublayer, the compressive stress is about 1 GPa larger than in the CrN layer close to the interface what proportionally correlated with the changes in FWHM of CrN 111 peaks. Though the ion bombardment was kept constant during the film growth, the flux of incoming accelerated particles from the plasma discharge may result in strong microstructural effects and the crystallites can re-align, deform, split up and decrease in size. A varying fraction of grain boundaries result usually in a non-homogeneous ion-induced defect generation and subsequently in a development of pronounced stress gradients across the film. Residual stress decrease and increase in CrN and Cr sublayers (Fig. B.5) can be interpreted by such processes and was discussed elsewhere [9].

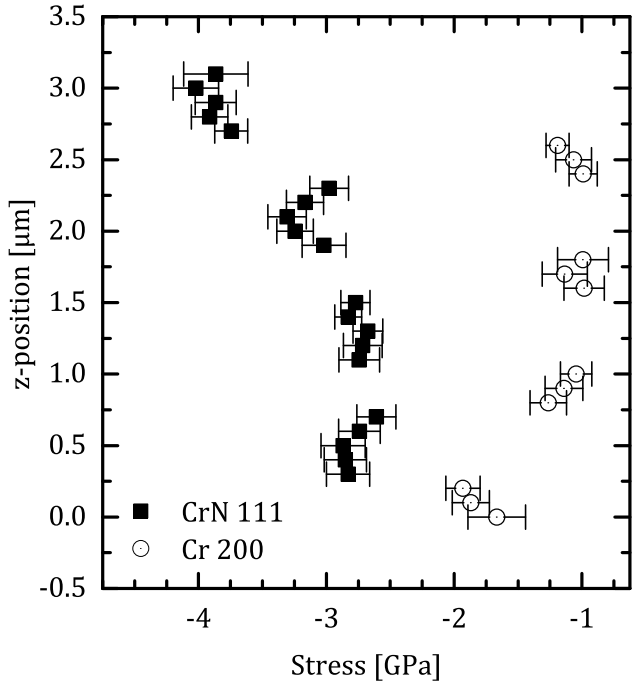

Figure B.5.: Residual stresses $\sigma_{22}(y = 0, z)$ in CrN and Cr sublayers determined with a resolution of 100 nm in the sample region not influenced by the indentation (at $y = 0$ in Fig. B.3). The decrease and increase of the compressive stresses in the top Cr and CrN sublayers could be correlated with a decreasing and increasing FWHM of Cr 200 and CrN 111 reflections.

Due to the film and substrate plastic deformation during indentation (Fig. B.2), complex strain gradients were formed in the film along the y and z directions. This can be qualitatively documented by the variations of the positions of CrN and Cr reflections at the film cross-section. In Fig. B.6, representative evolutions of Bragg's angles 2θ of CrN 111 and Cr 200 reflections along the y-axis recorded at different film depths z (*cf.* Fig. B.3) are presented. The data represent the diffraction on crystallographic planes oriented approximately perpendicular to the substrate surface. The 2θ values increase and decrease correspond to the increase of in-plane compressive and tensile strains, respectively, at the given sample position. The smooth changes of the 2θ angles document the presence of complex stress fields which span across a few µm from the indent tip.

Diffraction data collected from the dashed area in Fig. B.3 were used to evaluate residual stress fields $\sigma_{22}(y, z)$ across the CrN and Cr sublayers using Eq. (B.5). Three dominant effects can be identified in Fig. B.7, namely

1. the two top CrN sublayers, approximately 2 µm from the imprint, possess high compressive stresses up to -10 GPa (cf. Fig. B.7 a). The top most Cr sublayer in the same regions shows compressive and tensile stresses right and left to the imprint (Fig. B.7 b).

2. CrN regions right to the imprint and under the imprint exhibit high tensile stresses up to 2 GPa (Fig. B.7 a).

3. the high tensile stress fields in CrN are asymmetric with respect to the imprint vertical axis (Fig. B.7 a).

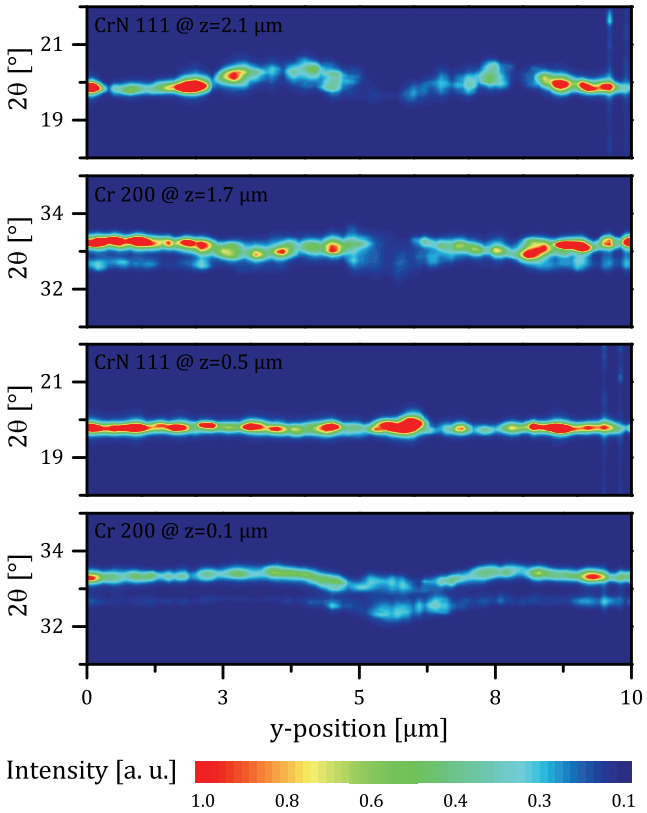

Figure B.6.: Lateral variation of 2θ positions of CrN 111 and Cr 200 reflections (along y-axis) at the film depths z of 2.1, 1.7, 0.5 and 0.1 µm. The 2θ values were obtained by integrating the respective Debye-Scherrer rings in an azimuthal range of $\delta = [80°, 100°]$. An upward shift (higher 2θ angle) corresponds to compression; a downward shift reflects tension. The data thus qualitatively indicate the presence of residual stresses in the individual sublayers which, however, change as a function of the film depth z and lateral position y.

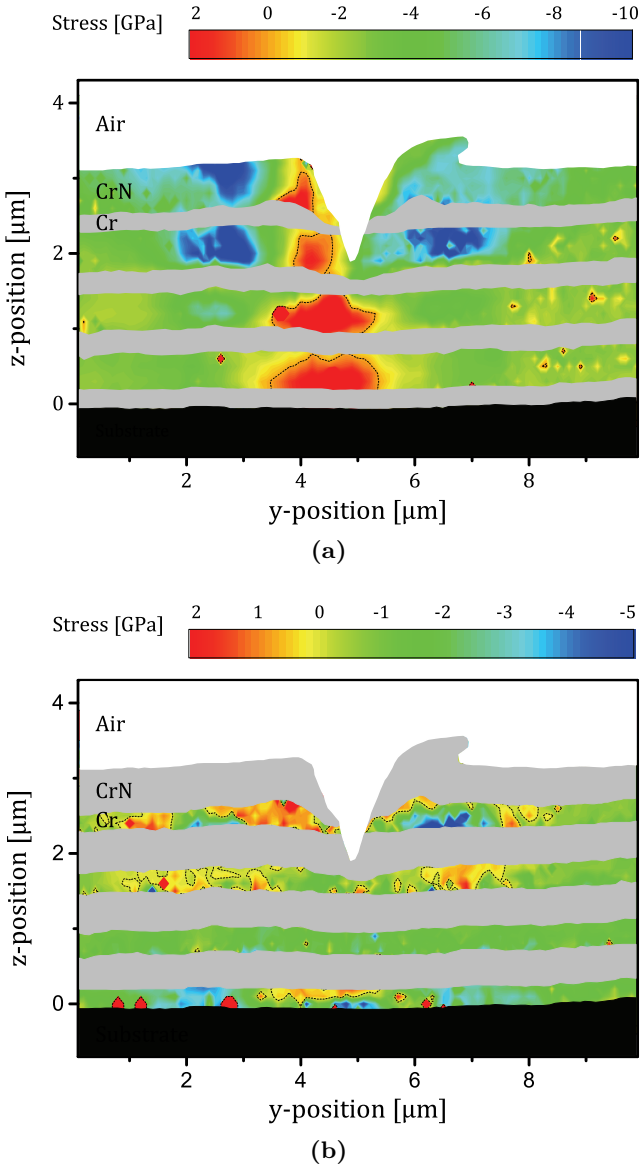

Figure B.7.: Residual stress distribution $\sigma_{22}(y, z)$ in CrN (Fig. B.7a) and Cr sublayers (Fig. B.7 b) after the wedge indentation as determined ex-situ by nanodiffraction on the indented sample with a spatial resolution of 100 nm. Besides some minor stress peaks (caused by the data scattering), three main effects can be recognized, namely (a) compressive stresses in the two top CrN sublayers, (b) tensile stresses in CrN under the imprint and (c) a strong asymmetry of the tensile stresses in CrN under the imprint.

Qualitatively, the observed high residual stresses in CrN (Fig. B.7) can be interpreted by a linear-elastic deformation in CrN sublayers and by a plastic deformation of Cr and the substrate during the indentation. After the unloading, the plastically deformed materials hindered the full relaxation of indentation-induced compressive and tensile stresses in the adjacent CrN regions. The asymmetry of the CrN tensile stress distribution under the imprint was caused by a tilt of the indenter with respect to the sample normal which resulted also in the material pile-up visible in Fig. B.2.

In the CrN two top sublayers, approximately 2 µm from the wedge vertical axis (in Fig. B.7 a), the indentation resulted in a formation of a high in-plane compressive stress which caused a plastic deformation in the two top most Cr sublayers and elastic deformation in the ceramic CrN. Upon unloading, the plastically deformed Cr sublayers constrained the in-plane stress relaxation of the CrN sublayers and caused the conservation of the compressive residual stresses in the CrN. In the top most Cr sublayer, the same process resulted in the formation of tensile and compressive residual stresses on the imprint left and right sides (Fig. B.7 b), respectively. The tensile stress in Cr top sublayer (left to the imprint) obviously balances the compressive stresses in the neighbouring CrN sublayers. The compressive stress in Cr top sublayer (right to the imprint) could be interpreted by the "tilted" indentation and CrN pile-up, which caused at first tensile plastic stresses in Cr which turned into compressive stresses after the unloading.

The formation of tensile residual stresses under the indent in the CrN sublayers (in Fig. B.7 a) can be explained in a similar manner. During the indentation, the plastically deformed Cr sublayers extended and slightly bended resulting in a sublayer necking or even ruptures. Upon unloading, the in-plane elastic relaxation of the CrN sublayers was inhibited by plastically deformed Cr sublayers and the substrate what resulted in the conservation of the tensile residual stress up to about 2 GPa in CrN.

In order to better understand the development of the stresses during and after the film indentation, the stress distributions across CrN and Cr sublayers (Fig. B.7) were analysed using FEM. The residual stress data in Fig. B.8 indicate the presence of two distinct regions with different characteristics. In the film upper part, the indentation-induced plastic deformation of the top most Cr sublayer (Fig. B.8 b) resulted in the development of a localized region with tensile residual stresses of about 2 GPa in the top CrN sublayer (Fig. B.8 a). Left and right to that region (at the y-positions of 4 µm and 6 µm, respectively), compressive residual stresses of about -8 GPa were formed in CrN (Fig. B.8 a). Both central tensile and sidewise compressive stress regions in the top CrN sublayer (Fig. B.8 a) are qualitatively

in the agreement with the experimental data in Fig. B.7 a. The presence of high compressive stress up to −5 GPa in the top most Cr-sublayer (Fig. B.8 b) is however in contradiction with the experimental data in Fig. B.7 b. The discrepancy can be explained by the small indentation depths applied in the model what is also the reason for the very localised compressive stress regions in the top CrN sublayer (Fig. B.8 a) in comparison with the experimental data in Fig. B.7 a.

The second region covers the lower part of the film near the substrate (Fig. B.8). Here the tensile residual stresses in CrN and Cr sublayers were caused by the substrate plastic deformation leading to a bending mode in the multi-layer (Fig. B.8). The results are in agreement with the experimental findings from Fig. B.7, where in the CrN and Cr sublayers next to the substrate tensile residual stresses were found. The fact that the width of the zone with tensile residual stresses in the simulation is larger compared to the measurement could be again explained by the larger distance between the indenter and the substrate at the maximum loading in the simulation (Fig. B.8).

For the chosen loading situation in the simulation (Fig. B.8), the region dominated by the local deformation in the Cr-sublayers and the region dominated by the deformation in the substrate were slightly more separated compared to the experiment (Fig. B.7), but in general the simulation showed the same residual stress picture. Therefore, the assumptions and the simplifications with respect to the residual stress evaluation procedure from the measured elastic strains, especially the neglecting of out-of-plane and shear stress components $\sigma_{33}(y,z) \simeq 0$ and $\sigma_{ij}(y,z) \simeq 0$, appear justified.

Up to now the indentation-induced irreversible changes in ceramic (TiN, CrN, diamond like carbon (DLC) films) and multi-layered (TiN-Ti, CrN-Cr) thin films have been extensively studied primarily using transmission-electron microscopy (TEM) with the focus on the microstructural aspects of the deformation behaviour [29–31]. The TEM studies indicated that the plastic deformation of the substrate resulted in the formation of pronounced cracks at the boundaries of adjacent V-shaped grains in ceramic films. The deformation behaviour of monolithic films was dominated by intercolumnar shear sliding whose resistance, tuned e.g. by compressive stresses, predetermined the hardness. In the case of multi-layered films, it was, however, observed that the metallic sublayers in CrN-Cr and TiN-Ti modify the deformation behaviour of the films from brittle to ductile[29, 30]. The cracks formed in ceramic sublayers, as a consequence of the intergranular sliding, were arrested between two ductile sublayers and the crack propagation was hindered by crack splitting and deflection as well as by the plastic deformation of the ductile sublayer.

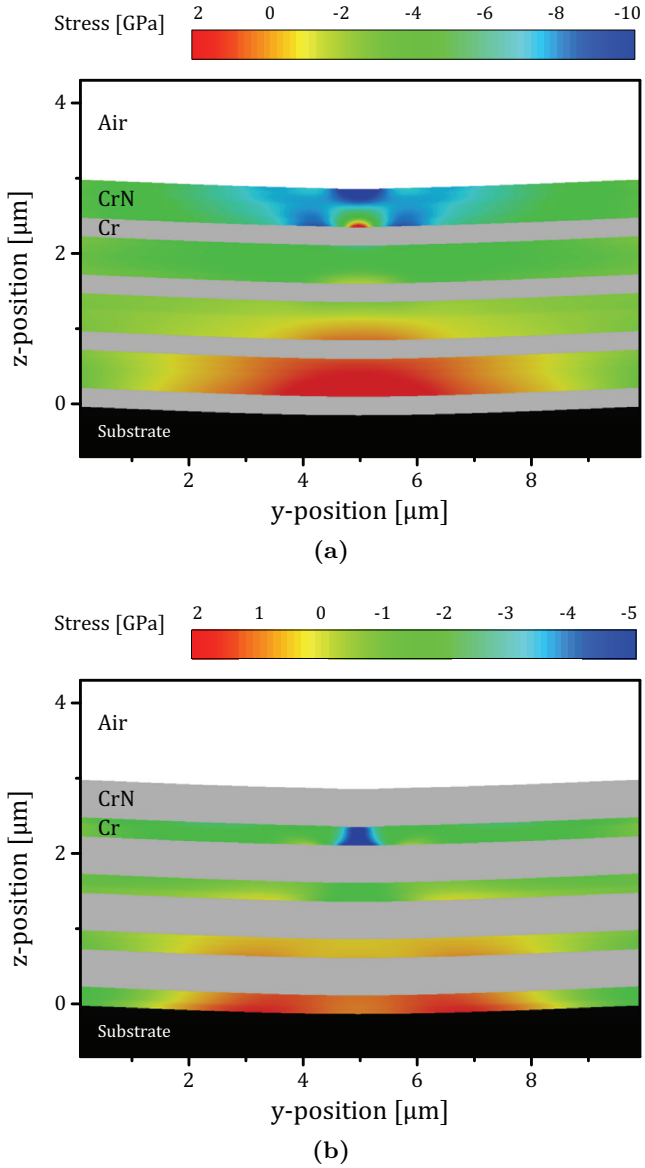

Figure B.8.: Residual stress distributions $\sigma_{22}(y, z)$ across CrN and Cr sublayers obtained from the FEM after the indentation applying the indenter displacement of 2 µm at the point of contact. Complex residual stress fields in the upper and lower part of the multi-layered film were induced by the plastic deformation of the Cr sublayers and the substrate as discussed in the text. For simplicity, the indenter was aligned perpendicular to the film interfaces and no penetration into the film was considered.

This mechanism can also be observed in biological materials such as nacre [30]. It should be however noted that the ex-situ TEM studies were performed mostly on the samples prepared using a spherical indenter and by applying relatively large penetration depths, thus causing more deformation of the substrates and bending of the thin films [29].

The present experimental data, which represent the first experimental mapping of strains and stresses in such complex multi-layered nano-system, extend the understanding of the deformation behaviour in ductile-brittle systems. The indentation resulted in the formation of pronounced stresses in CrN sublayers, very probably beyond the fracture limit, which relaxed only partly after the unloading. The tensile stresses of about 2 GPa in CrN at the indenter tip (Fig. B.7 a) would normally result in catastrophic damage of the film but the presence of ductile Cr sublayers arrested the micro-cracks formed in CrN which could therefore not penetrate through the whole film thickness. Another important feature is the good adhesion between the sublayers and the substrate, which ensured that the stress peaks and damage in the brittle CrN did not result in the film rupture or delamination. The CrN regions with large compressive and tensile stresses after indentation were arrested between the ductile Cr sublayers which actually secured the mechanical integrity of the thin-film-substrate composite.

It is obvious that the management of stress peaks in thin films during and after the indentation is an important prerequisite to optimize the film mechanical integrity and life time. In order to minimize the stress peaks, one strategy is to adjust the stress state in the as-deposited thin film [7]. Since the nature of the stress generation in the individual sublayers during the indentation depends however on the sublayer position at the cross-section and on its brittle or ductile nature, the tailored adjustment of the stress distribution at the thin film cross-section can serve as an important tool to optimize the deformation behaviour of thin films, especially the resistance to fracture.

B.5. Conclusions

Cross-sectional X-ray nanodiffraction analysis was used to characterize residual stresses at the cross-section of a wedge-indented brittle-ductile CrN-Cr thin film. For the first time, the results revealed a complex residual stress distribution with compressive and tensile stress peaks especially in the brittle CrN with 100 nm spatial resolution. The pronounced residual stresses in CrN are consequence of Cr and substrate plastic deformation during the indentation. During the indenter un-

loading, the plastically deformed materials hinder the full relaxation of indentation-induced compressive and tensile stresses in linear elastic deformed CrN regions and the stresses remain partly conserved in CrN.

The results demonstrate that the ductile Cr sublayers serve as a stabilizing component which secures the mechanical integrity for the multilayer. Though the indentation resulted in the formation of tensile and compressive stresses in GPa range and very probably also in the generation of micro-cracks, the overall film mechanical integrity was not affected. This is also to due to the excellent adhesion between the sublayers and the substrate, which ensured that the stress peaks and damage did not result in the film rupture or delamination whereas the damage in CrN remained arrested between the ductile Cr sublayers and the substrate.

Methodologically, it can be expected that the novel ex-situ X-ray nanodiffraction approach of the detailed residual stress analysis at the cross-section of multilayered thin films with will serve as an important tool to quantify indentation-induced microstructural and residual stress changes in around indenter imprint. The approach will be used especially for the optimization of fracture resistance in complex microstructured thin films.

B.6. Acknowledgement

Financial support by the Austrian Federal Government (in particular from Bundesministerium für Verkehr, Innovation und Technologie and Bundesministerium für Wirtschaft, Familie und Jugend) represented by Österreichische Forschungsförderungsgesellschaft mbH and the Styrian and the Tyrolean Provincial Government, represented by Steirische Wirtschaftsförderungsgesellschaft mbH and Standortagentur Tirol, within the framework of the COMET Funding Programme is gratefully acknowledged.

Bibliography to paper B

[1] E. Arzt. *Acta Mater*, 46(16):5611–5626, 10/9 1998. doi:10.1016/S1359-6454(98)00231-6.

[2] K. S. Kumar, H. Van Swygenhoven, and S. Suresh. *Acta Mater*, 51(19):5743–5774, 2003. doi:10.1016/j.actamat.2003.08.032.

[3] H. Gleiter. *Prog Mater Sci*, 33(4):223–315, 1989. doi:10.1016/0079-6425(89)90001-7.

[4] P. H. Mayrhofer, C. Mitterer, L. Hultman, and H. Clemens. *Prog Mater Sci*, 51(8):1032–1114, 2006. doi:10.1016/j.pmatsci.2006.02.002.

[5] I. Petrov, L. Hultman, J.-E. Sundgren, and J. E. Greene. *J Vac Sci Technol A*, 10(2):265–272, 1992. doi:10.1116/1.578074.

[6] R. Daniel, K. Martinschitz, J. Keckes, and C. Mitterer. *J. Phys. D: Appl. Phys.*, 42(7):075401, 2009. doi:10.1088/0022-3727/42/7/075401.

[7] R. Daniel, J. Keckes, I. Matko, M. Burghammer, and C. Mitterer. *Acta Mater*, 61(16):6255–6266, 2013. doi:10.1016/j.actamat.2013.07.009.

[8] A. Misra, J. P. Hirth, and R. G. Hoagland. *Acta Mater*, 53(18):4817–4824, Oct 2005. doi:10.1016/j.actamat.2005.06.025.

[9] R. Daniel, K. Martinschitz, J. Keckes, and C. Mitterer. *Acta Mater*, 58(7):2621–2633, 2010. doi:10.1016/j.actamat.2009.12.048.

[10] O. Kolednik, J. Predan, F. D. Fischer, and P. Fratzl. *Adv Funct Mater*, 21(19):3634–3641, Oct 2011. doi:10.1002/adfm.201100443.

[11] G. M. Pharr, E. G. Herbert, and Y. Gao. *Annu Rev Mater Res*, 40(1):271–292, 2010. doi:10.1146/annurev-matsci-070909-104456.

[12] R. I. Barabash, W. Liu, J. Z. Tischler, H. Bei, and J. D. Budai. *Acta Mater*, 60(8):3279–3286, May 2012. doi:10.1016/j.actamat.2012.02.052.

[13] D. Kiener, K. Durst, M. Rester, and A. M. Minor. *J Mater*, 61(3):14–23, 2009. doi:10.1007/s11837-009-0036-4.

[14] K. K. McLaughlin and W. J. Clegg. *J. Phys. D: Appl. Phys.*, 41(7):1–5, 2008. doi:10.1088/0022-3727/41/7/074007.

[15] M. Rester, C. Motz, and R. Pippan. *Acta Mater*, 55:6427–6435, 2007. doi:10.1016/j.actamat.2007.08.001.

[16] G. Feng, A. S. Budiman, W. D. Nix, N. Tamura, and J. R. Patel. *J Appl Phys*, 104(4):043501, August 2008. doi:10.1063/1.2966297.

[17] M. S. Fuller, R. Barabash, S. Mcintyre, S. Ramamurthy, and W. Liu. *Metall Mater Trans A*, 44A(1):17–21, January 2013. doi:10.1007/s11661-012-1219-0.

[18] D. Allen, J. Wittge, A. Zlotos, E. Gorostegui-Colinas, J. Garagorri, P. J. McNally, A. N. Danilewsky, and M. R. Elizalde. *Nucl Instrum Meth B*, 268 (3-4):383–387, February 2010. doi:10.1016/j.nimb.2009.10.174.

[19] M. K. Khan, M. E. Fitzpatrick, S. V. Hainsworth, A. D. Evans, and L. Edwards. *Acta Mater*, 59(20):7508–7520, 2011. doi:10.1016/j.actamat.2011.08.034.

[20] J. Keckes, M. Bartosik, R. Daniel, C. Mitterer, G. Maier, W. Ecker, J. Vila-Comamala, C. David, S. Schoeder, and M. Burghammer. *Scripta Mater*, 67(9): 748–751, 2012. doi:10.1016/j.scriptamat.2012.07.034.

[21] D. Kiener, C. Motz, G. Dehm, and R. Pippan. *Int J Mater Res*, 100(8):1074–1087, August 2009. doi:10.3139/146.110149.

[22] M. Stefenelli, J. Todt, A. Riedl, W. Ecker, T. Müller, R. Daniel, M. Burghammer, and J. Keckes. *J Appl Crystallogr*, 46(5):1378–1385, 2013. doi:10.1107/S0021889813019535.

[23] J. Kieffer and D. Karkoulis. *J Phys Conf Ser*, 425(202012), 2013. doi:10.1088/1742-6596/425/20/202012.

[24] J. Kieffer and J. P. Wright. *Powder Diffr*, 28:339–350, September 2013. doi:10.1017/S0885715613000924.

[25] J. Almer, U. Lienert, R. L. Peng, C. Schlauer, and M. Oden. *J Appl Phys*, 94 (1):697–702, 2003. doi:10.1063/1.1582351.

[26] J. Pina, A. Dias, M. François, and J. Lebrun. *Surf. Coat. Technol.*, 96(2-3): 148–162, 1997. doi:10.1016/S0257-8972(97)00075-3.

[27] A. Riedl, R. Daniel, M. Stefenelli, T. Schöberl, O. Kolednik, C. Mitterer, and J. Keckes. *Scr. Mater.*, 67(7-8):708–711, 2012. doi:10.1016/j.scriptamat.2012.06.034.

[28] O. Kolednik, J. Predan, F. Fischer, and P. Fratzl. *Acta Mater*, 68:279–294, 2014. doi:10.1016/j.actamat.2014.01.034.

[29] P. Wieciński, J. Smolik, H. Garbacz, and K. Kurzydlowski. *Surf. Coat. Technol.*, 240(0):23–31, 2014. doi:10.1016/j.surfcoat.2013.12.006.

[30] J. Lackner, W. Waldhauser, B. Major, L. Major, and M. Kot. *Thin Solid Films*, 534:417–425, 2013. doi:10.1016/j.tsf.2013.03.025.

[31] Z. H. Xie, M. Hoffman, P. Munroe, A. Bendavid, and P. J. Martin. *Acta Mater*, 56(4):852–861, February 2008. doi:10.1016/j.actamat.2007.10.047.

[32] N. J. M. Carvalho and J. T. M. De Hosson. *Acta Mater*, 54(7):1857–1862, April 2006. doi:10.1016/j.actamat.2005.12.010.

[33] K. Martinschitz, R. Daniel, C. Mitterer, and J. Keckes. *Thin Solid Films*, 516 (8):1972–1976, 2008. doi:10.1016/j.tsf.2007.10.106.

C

Macroscopic Fracture Behaviour of CrN Hard Coatings Evaluated by X-Ray Diffraction Coupled with Four-Point Bending

Mario Stefenelli[a], Angelika Riedl[a], Juraj Todt[b,c], Matthias Bartosik[b,c], Rostislav Daniel[d], Christian Mitterer[d], Jozef Keckes[b,c]

[a]Materials Center Leoben Forschung GmbH, Leoben, Austria

[b]Department of Materials Physics, Montanuniversität Leoben, Austria

[c]Erich Schmid Institute of Materials Science, Austrian Academy of Sciences, Leoben, Austria

[d]Department of Physical Metallurgy and Materials Testing, Montanuniversität Leoben, Austria

Abstract

Fracture behaviour of hard nanocrystalline coatings decisively influences the lifetime and performance of coated tools. In this work, residual stresses in as-deposited and annealed CrN coatings deposited at 350 °C using bias voltages of 40 V and 120 V

were evaluated using synchrotron X-ray diffraction coupled with four-point bending. The stress development during the bending experiments was used to analyse fracture properties of the coatings. The results indicate that an annealing at 550 °C does not deteriorate the fracture behaviour of the coatings prepared using −40 V bias. In the case of −120 V bias coatings, the residual stress relaxation after the thermal treatment is accompanied by a fracture strain decrease and a fracture stress increase. The as-deposited and annealed CrN coatings deposited using −120 V bias exhibit significantly large fracture strains in comparison with −40 V samples. Finally the results document that the fracture stress may not be the only relevant parameter when comparing different coating systems. Also the strain at fracture can be considered as significant indicator of the coating fracture response. Methodologically, the results indicate that in-situ X-ray diffraction coupled with four point bending can be effectively used to evaluate macroscopic fracture behaviour of hard coatings.

C.1. Introduction

C.1.1. Thermo-Mechanical Properties of Hard Coatings.

Protective nanocrystalline hard coatings are extensively used in various machining applications like dry or high speed cutting in order to enhance working tool lifetime and performance. During service, the coatings have to withstand extreme mechanical and thermal loads with peak temperatures of more than 1000 °C reached within milliseconds [1]. Generally, the coatings are expected to exhibit high hardness, fracture toughness and oxidation resistance which, if possible, do not deteriorate during the service.

Magnetron sputtering represents a common technique to produce nanocrystalline hard coatings. During sputtering, moderate bias voltage is often applied in order to accelerate ions from the plasma discharge to the substrates to enhance atom mobility on the surface of growing deposits. A high bias voltage results typically in an intensive ion peening of the growing coating surface and in the formation of pronounced compressive residual stresses [2, 3]. By selecting dedicated bias voltages, it is thus possible to controllably tune the properties of coatings like crystallite size, crystallographic texture, density of growth defects and residual stresses [4, 5].

Magnetron sputtered CrN coatings usually exhibit compressive residual stresses [3, 6]. Generally, the residual stress in an as-deposited coating originates from the growth process (accompanied by the ion peening) as well as from the cooling

down from deposition to room temperature. The cooling results in the formation of thermal stresses, where their sign and magnitude depend on the mismatch of coefficients of thermal expansion (CTE) of coating α_c and substrate α_s. Thus, the thermal stress formation can result in an increase or a release of compressive growth stress for $\alpha_c < \alpha_s$ and $\alpha_c > \alpha_s$, respectively.

In the case of magnetron sputtered hard coatings, however, heat treatment above the deposition temperature results in the relaxation of compressive residual stresses and in softening of the coating [6, 7]. This effect is caused by recovery effects in the lattice which occur as a result of migration and recombination of point defects, rearrangement and annihilation of dislocations and growth and coalescence of subgrains [8, 9]. Hardness measurements on as-deposited and annealed coatings indicate a decrease of coating hardness after thermal treatment [6].

Up to now, the influence of bias voltage and post-deposition thermal treatment on the mechanical properties of hard coatings was studied predominantly locally by performing hardness measurements. For the determination of representative volume-averaged fracture properties of hard coatings, however, it is necessary to apply techniques which can be used to reveal (i) intrinsic volume-averaged fracture behaviour of the hard coating material and (ii) fracture properties of the coating-substrate composite with its unique interface mechanical response.

Recently, we have demonstrated that bending experiments of chemically etched and focused ion beam shaped free-standing coating cantilevers can be used to determine fracture behaviour of hard coatings at the µm *scale*. The approach was used to analyse intrinsic fracture properties of as-deposited and annealed sputtered CrN coatings [10].

The aim of this contribution is to evaluate the *macroscopic* fracture behaviour of CrN coatings on flexible steel substrates by analysing residual stresses during four-point bending in as-deposited and in thermally cycled coatings prepared by magnetron sputtering at bias voltages of $-40\,\mathrm{V}$ and $-120\,\mathrm{V}$.

C.2. Experimental

C.2.1. Coating Deposition.

CrN coatings with a thickness of 3 µm were deposited by reactive magnetron sputtering from a Cr target in an argon/nitrogen atmosphere at 350 °C applying bias voltages of $-40\,\mathrm{V}$ and $-120\,\mathrm{V}$ on austenitic steel substrates (DIN 1.4301, X5CrNi18-10) with thickness of 1.5 mm and dimensions of $32 \times 8\,\mathrm{mm}^2$ [4].

C.2.2. High-Temperature X-ray diffraction (HT-XRD).

HT-XRD was used to analyse residual stress relaxation in selected CrN/steel samples during thermal cycling in the range of 25 °C to 550 °C using steps of 50 °C and by applying constant heating and cooling rates of 0.3 °C s^{-1}. Characterization was performed using a Seifert PTS 3000 four-circle diffractometer applying Cr-K$_\alpha$ radiation. The samples were thermally cycled in a DHS1100 heating attachment (Anton Paar GmbH) in a non-reactive N_2 atmosphere. The lattice spacing d_ψ^T of CrN 111 reflections measured at the temperature T and the sample tilt angle ϕ was used to refine in-plane isotropic biaxial residual stress σ_T according to

$$d_\psi^T = d_0^T \left[1 + \sigma^T \left(2s_1 + \frac{1}{2}s_2 \sin^2\psi\right)\right] \tag{C.1}$$

where s_1 and $\frac{1}{2}s_2$ are the X-ray elastic constants (XECs) [11]. It was supposed that the residual stresses in the coatings are in-plane isotropic, i. e. $\sigma^T = \sigma_{11}^T = \sigma_{22}^T$ [12]. XECs for the CrN coating were calculated from the single-crystal elastic constants (SECs) assuming the Hill model [12].

C.2.3. Thermal Treatment.

Selected CrN/steel samples were thermally treated in a high-temperature chamber (without XRD characterization) at the conditions similar to those from HT-XRD cycle (with maximal temperature of 550 °C) in order to induce recovery and compressive stress relaxation.

C.2.4. In-situ Four-Point Bending Characterization.

In-situ energy dispersive XRD experiments coupled with four-point bending were conducted at the EDDI beam line of the BESSY synchrotron source in Berlin. The rectangular samples were loaded using a Kammrath&Weiss four-point bending stage. The loading was done way-controlled in steps of 50 µm deflection with a speed of 5 µm s^{-1}. The samples were bent until the stresses in the film saturated and the final measurement was done at a deflection of 1500 µm for all samples in order to compare the fracture behaviour. The in-situ development of the biaxial stresses σ_{11} and σ_{22} during bending was evaluated from the lattice spacing $d_{\phi,\psi}$ of CrN 111 reflections according to

$$d_{\phi,\psi} = d_0 \left[1 + (\sigma_{11} + \sigma_{22})\, s_1 + \frac{1}{2} s_2 \sigma_\phi \sin^2 \psi\right] \qquad \text{(C.2)}$$
$$\text{with } \sigma_\phi = \sigma_{11} \sin^2 \phi + \sigma_{22} \cos^2 \phi$$

where ϕ represents sample azimuthal angle [12]. The measurements were performed at a constant 2θ angle of 12° in symmetric $\theta/2\theta$ geometry. The stress components σ_{11} and σ_{22} were parallel to the longer and shorter sample sides and represent thus the primary stress directions influenced by the bending experiment.

C.2.5. Analysis of Fracture Surfaces.

The fracture behaviour of the coatings was analysed using a LEO1525 scanning electron microscope (SEM). The images were taken ex-situ after the bending measurements. From the images, the average crack spacing $\overline{\lambda}$ was determined by measuring the distance between the intersection points with a line perpendicular to the cracks.

C.3. Results

C.3.1. Thermal Behaviour of Stresses.

In order to analyse the degree of the temperature-controlled recovery processes in CrN coatings deposited at −40 V and −120 V bias voltages, HT-XRD was used to characterize the stress development during thermal cycling in the range of 25 °C to 550 °C (Fig. C.1).

The HT-XRD experiments revealed a significant difference between the coatings. In the−40 V coating only thermoelastic stress change without any hysteresis was observed. When heated up, the compressive residual stress in the coating decreased (*cf.* A in Fig. C.1) due to the mismatch in the CTE with $\alpha_c < \alpha_s$. Upon cooling down, the effect is reversed without affecting the residual stress at room temperature after the cooling (B). The −120 V coating showed thermoelastic relaxation until the deposition temperature was reached (C). When heating continued, recovery of growth defects was observed accompanied by the decrease of the compressive stress (D). During cooling down the compressive stress increased thermoelastically (E) as a consequence of the CTE mismatch (similarly as in the sample with −40 V).

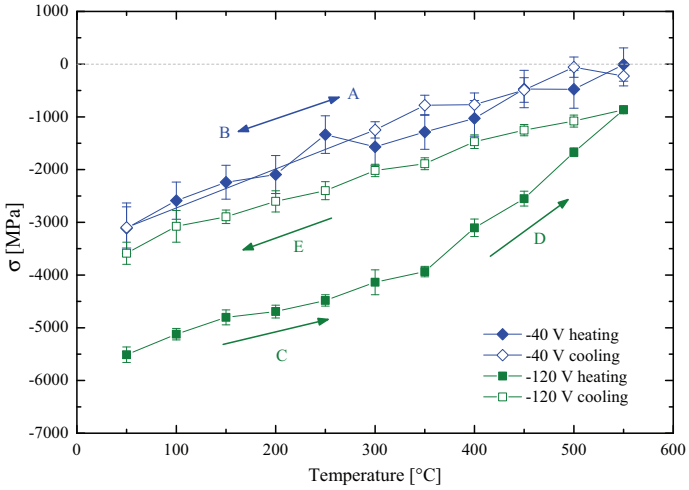

Figure C.1.: Temperature dependence of in-plane residual stresses in CrN coatings deposited using bias voltages of −40 V and −120 V. In the −120 V coating, the heating above the deposition temperature (350 °C) results in defect recovery and in the subsequent relaxation of compressive stress.

The observed defect recovery resulted in a decrease of the compressive residual stress from about −5.5 GPa to −3.6 GPa. The stress-temperature dependence in the −120 V sample during cooling down is approximately parallel with that from the −40 V sample. This suggests that the annealing of the −120 V coating modified the coatings properties towards the −40 V sample.

C.3.2. In-situ Four-Point Bending Experiments.

Macroscopic residual stresses in as-deposited and annealed CrN/steel samples prepared using bias voltages of −40 V and −120 V were characterized in-situ during four-point bending by XRD (Fig. C.2) using a X-ray beam with a diameter of 0.5 mm. As already mentioned in the experimental part, the annealed samples for the four-point bending experiments were prepared using a dedicated high-temperature chamber (without in-situ XRD characterization). Though the thermal conditions were similar to those used for HT-XRD, the final residual stresses after the annealing were not identical with the stresses observed after the thermocycles (Fig. C.1). This can be explained by small differences in the temperature history, by a very strong dependence of the recovery processes on the actual heating and cooling rates and by possible structural changes in the substrates during annealing.

Qualitatively, the specimens showed the same type of response when subjected to mechanical loads. At first, the compressive stresses decreased linearly until frac-

ture, after which the macroscopic stress level in the coatings remained constant (Fig. C.2 a). As-deposited and annealed −40 V samples exhibit similar behaviour with very similar initial and final residual stress states. This correlates well with their thermal behaviour (*cf.* Fig. C.1) and indicates that the thermal treatment of the coatings prepared using a relatively low bias voltage does not influence significantly their (macroscopic) mechanical properties, which are primarily dependent on the microstructure and residual stress state. The different initial residual stresses in as-deposited and annealed −40 V samples (Fig. C.2 a) indicate that the thermal annealing in the heating chamber (*cf.* Experimental) was not absolutely identical with the thermal treatment performed during the in-situ HT-XRD experiment (Fig. C.1)

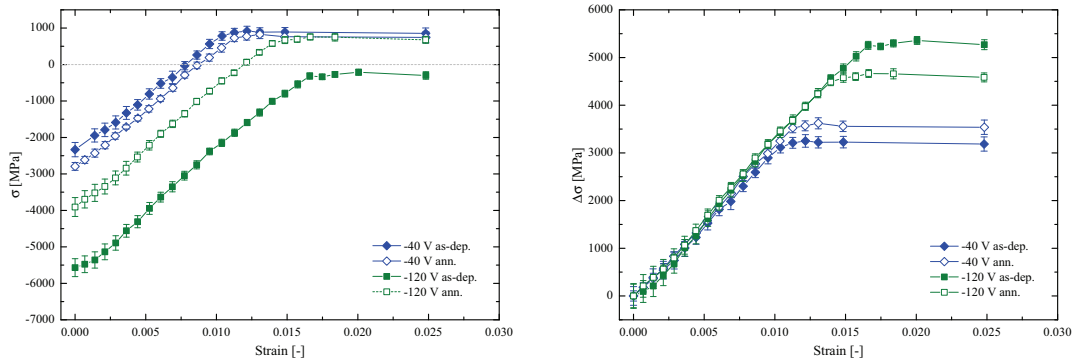

(a) **(b)**

Figure C.2.: Evolution of the macroscopic residual stresses in as-deposited and annealed CrN coatings deposited at −40 V and −120 V bias voltage during in-situ bending experiment (a). All coatings show at first a linear elastic stress reduction followed by fracture, resulting in the saturation of the stress level. In (b) the relative stress changes as the function of macroscopic strain indicates large fracture strains in both −120 V coatings.

Upon loading of the as-deposited −120 V sample, one can observe the stress saturation at relatively high strains and a surprisingly slightly compressive final stress level of −250 MPa. This suggests that the observed average stress in the coating is lower than the maximal stress leading to the fracture, which is expected to be positive. In the annealed −120 V sample, the final stress level after the fracture is in the same stress region as for the −40 V samples. This finding indicates that the thermal treatment connected with the recovery caused an apparent increase of the macroscopic fracture stress (Fig. C.2a).

In Fig. C.2 b, relative stress changes as a function of the applied strain are shown. The dependencies indicate that the both −120 V samples exhibit a significantly

higher fracture strain and also large relative stress changes till fracture. The comparison of the dependencies from Figs. C.2 a and C.2 b documents that for practical applications the fracture stress may not be the only relevant parameter when comparing different coating systems. Also the strain at fracture can be considered as significant indicator of the fracture response of a coating system.

C.3.3. Coating Cracking Behaviour.

Surface topography of the as-deposited and annealed coatings after the four-point bending experiments was characterized using SEM. In Fig. C.3, representative SEM images of the coating surfaces are presented. The images indicate the presence of mostly parallel cracks which are, however, not equidistant as predicted by the shear-lag model [13–15]. There is a small difference in the average crack spacing $\overline{\lambda}$ between the -40 and the $-120\,\mathrm{V}$ coating, whereby $\overline{\lambda}$ for $-40\,\mathrm{V}$ coatings is smaller than for $-120\,\mathrm{V}$ coatings.

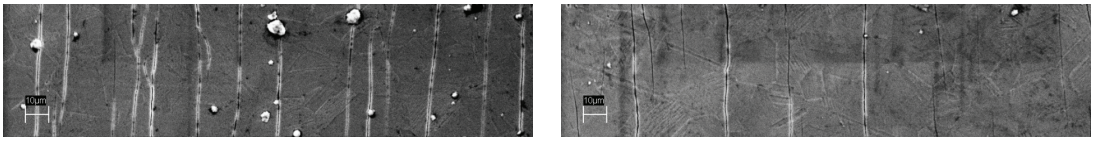

(a) $-40\,\mathrm{V}$ as-dep., $\overline{\lambda} = 15\,\mu\mathrm{m}$ **(b)** $-40\,\mathrm{V}$ ann., $\overline{\lambda} = 18\,\mu\mathrm{m}$

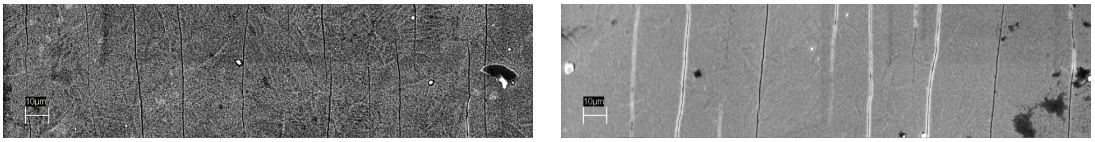

(c) $-120\,\mathrm{V}$ as-dep., $\overline{\lambda} = 28\,\mu\mathrm{m}$ **(d)** $-120\,\mathrm{V}$ as-dep., $\overline{\lambda} = 28\,\mu\mathrm{m}$

Figure C.3.: SEM micrographs show the topography of as-deposited and annealed CrN/steel samples after the four-point bending experiments.

C.3.4. Results Interpretation.

The aim of the present study is to correlate the fracture behaviour of CrN coatings with their stress state after the deposition and after the post-deposition annealing treatment. It is obvious that the macroscopic residual stress dependencies from Fig. C.2 express the average stress state in the coatings. The SEM images in Fig. 3 indicate, however, a periodic stress variation $\sigma(x)$ along the surface axis x (Fig. C.4), which can be generally expressed using the modified shear-lag model for soft plastically deformed substrates [13] as follows:

$$\sigma(x) = \left[\frac{E_f \varepsilon_{el}}{1-\nu_f^2}\left(1-\nu_f\nu_s\right)\right] \cdot \left[1 - \frac{\cosh\left(\beta x\right)}{\cosh\left(\frac{\beta\lambda}{2}\right)}\right] + \sigma_{res,pl}. \tag{C.3}$$

E_s, E_f, ν_f and ν_s are the Young's moduli and Poisson's ratios of the coating and the substrate, respectively. ε_{el} is the substrate elastic strain and β is a dimensionless parameter which depends on the thickness of the coating and the substrate. It expresses the shear stress transfer across the interface [14, 16]. The term $\sigma_{res,pl}$ is dependent on the initial residual stress and the applied strain.

Ahmed [13] has showed that when the maximum stress in a coating segment reaches the fracture stress σ_f, a new crack develops in the middle of the segment causing the stress in the adjacent segments to drop by $\Delta\sigma$ because at the same strain the stress in a smaller segment is lower than in a larger one. The stress drop can be mathematically described by

$$\begin{aligned}\Delta\sigma &= \sigma(x=0,\lambda) - \sigma\left(x=0,\tfrac{\lambda}{2}\right) \\ &= -\left[\frac{E_f \varepsilon_{el}}{1-\nu_f^2}\left(1-\nu_f\nu_s\right)\right] \cdot \left[1/\cosh\left(\frac{\beta\lambda}{2}\right) - 1/\cosh\left(\frac{\beta\lambda}{4}\right)\right].\end{aligned} \tag{C.4}$$

Thus at a microscopic level, the crack development in the film is accompanied by a sequence of stress drops until the stresses in the coating saturate. Mathematically this is governed by

$$\lim_{\lambda\to 0} \Delta\sigma = 0 \tag{C.5}$$

Therefore, at a certain point of the bending experiment one can observe a saturation of crack spacing and stresses in the coating and no further cracks will develop. Further straining will cause the segments to move apart, rather than the development of new cracks or an increase in stress. Consequently, the stress saturation in the stress-bending dependencies in Fig. C.2 indicates that the final stresses are lying slightly below the actual fracture stress of the coatings and close to the $\sigma_{res,pl}$ level.

Since the stresses in the coating were characterized using XRD with a relatively large gauge volume (in comparison to $\overline{\lambda}$), the obtained coating volume-averaged stresses (Fig. C.2) represent only average values over a large coating area. Generally, the average stress along one segment can be calculated by forming the integral average of Eq. (C.3).

$$\begin{aligned}\sigma_{avg} &= \frac{1}{\lambda}\int_{-\lambda/2}^{\lambda/2}\sigma(x)dx \\ &= \frac{E_f\varepsilon_a\cdot(1-\nu_f\nu_s)\cdot\left[\beta\lambda-2\tanh\left(\frac{\beta\lambda}{2}\right)\right]}{\beta\lambda\left(1-\nu_f^2\right)}+\sigma_{res,pl}\end{aligned} \tag{C.6}$$

Since $\overline{\lambda}$ for all four CrN coatings (Fig. C.3) is in the same range 15 µm to 28 µm, one can conclude that the final stress level in the fractured coatings is decisively influenced by the term $\sigma_{res,pl}$, which is mainly dependent on the initial residual stresses and the applied stress. In other words, the analysis showed that the σ_{avg} at the final stage of the bending experiments can be very effectively tuned by the magnitude of the initial stresses and by the thermal treatment. Unfortunately, the exact $\sigma(x)$ distribution along the surface (Fig. C.4) was not accessible at this stage.

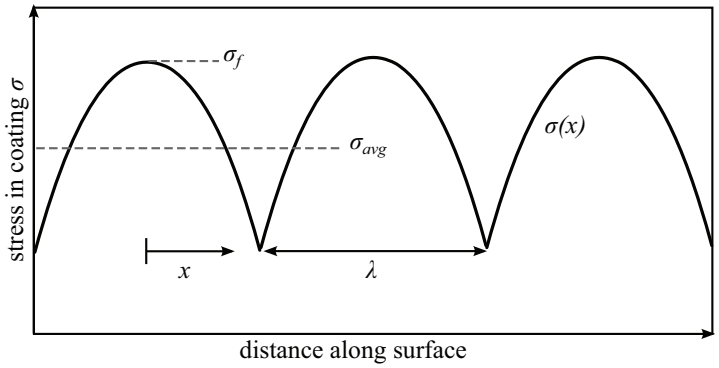

Figure C.4.: Scheme of theoretic stress distribution according to $\sigma(x)$ for multiple cracks.

C.4. Conclusions

Fracture behaviour of CrN coatings on steel substrates was assessed using in-situ XRD coupled with four-point bending. The fracture properties like macroscopic fracture stress and strains were evaluated from the in-situ experiments on as-deposited and annealed samples. The results indicate that the stress level at the final stages of the bending experiments depend on the residual stress state and sample thermal history. While the fracture behaviour of the CrN coating deposited at −40 V is only slightly affected by the annealing above the deposition temperature, it is very pronounced in the case of highly compressively stressed −120 V sample. Here, the annealing caused not only a relaxation of the residual stress but also a decrease of

the fracture strain and increase of the fracture stress. The as-deposited and annealed CrN coatings deposited using −120 V exhibit significantly large fracture strains in comparison with −40 V samples.

Methodologically, the results indicate that in-situ XRD coupled with four-point bending can be effectively used to roughly evaluate fracture properties of hard coatings.

C.5. Acknowledgement

Financial support by the Austrian Federal Government (in particular from the Bundesministerium für Verkehr, Innovation und Technologie and the Bundesministerium für Wirtschaft, Familie und Jugend) and the Styrian Provincial Government represented by Österreichische Forschungsförderungsgesellschaft mbH and by Steirische Wirtschaftsförderungsgesellschaft mbH, within the research activities of the K2 Competence Centre on "Integrated Research in Materials, Processing and Product Engineering" operated by the Materials Center Leoben Forschung GmbH in the framework of the Austrian COMET Competence Centre Programme, is gratefully acknowledged. We thank Helmholtz Zentrum Berlin for the allocation of synchrotron radiation beamtime and also Prof. Christoph Genzel and Manuela Klaus for the assistance. The research leading to these results has received funding from the European Community's Seventh Framework Programme (FP7/2007-2013) under grant agreement № 226716.

Bibliography to paper C

[1] J. Kopac, M. Sokovic, and S. Dolinsek. *J Mater Process Tech*, 118:377–384, 2001. doi:10.1016/S0924-0136(01)00974-8.

[2] D. M. Mattox. *J Vac Sci Technol A*, 7(3):1105–1114, 1989. doi:10.1116/1.576238.

[3] R. Daniel, K. Martinschitz, J. Keckes, and C. Mitterer. *Acta Mater*, 58(7): 2621–2633, 2010. doi:10.1016/j.actamat.2009.12.048.

[4] R. Daniel, K. Martinschitz, J. Keckes, and C. Mitterer. *J. Phys. D: Appl. Phys.*, 42(7):075401, 2009. doi:10.1088/0022-3727/42/7/075401.

[5] I. Petrov, L. Hultman, J.-E. Sundgren, and J. E. Greene. *J Vac Sci Technol A*, 10(2):265–272, 1992. doi:10.1116/1.578074.

[6] P. H. Mayrhofer, C. Mitterer, L. Hultman, and H. Clemens. *Prog Mater Sci*, 51(8):1032–1114, 2006. doi:10.1016/j.pmatsci.2006.02.002.

[7] K. Martinschitz, R. Daniel, C. Mitterer, and J. Keckes. *Thin Solid Films*, 516 (8):1972–1976, 2008. doi:10.1016/j.tsf.2007.10.106.

[8] J. D. Verhoeven. *Fundamentals of physical metallurgy*. Wiley, 1975.

[9] R. Daniel, D. Holec, M. Bartosik, J. Keckes, and C. Mitterer. *Acta Mater*, 59 (17):6631–6645, 2011. doi:10.1016/j.actamat.2011.07.018.

[10] A. Riedl, R. Daniel, M. Stefenelli, T. Schöberl, O. Kolednik, C. Mitterer, and J. Keckes. *Scr. Mater.*, 67(7-8):708–711, 2012. doi:10.1016/j.scriptamat.2012.06.034.

[11] J. Almer, U. Lienert, R. L. Peng, C. Schlauer, and M. Oden. *J Appl Phys*, 94 (1):697–702, 2003. doi:10.1063/1.1582351.

[12] I. C. Noyan and J. B. Cohen. *Measurement by Diffraction and Interpretation*. Springer, 1987.

[13] F. Ahmed, K. Bayerlein, S. Rosiwal, M. Göken, and K. Durst. *Acta Mater.*, 59 (14):5422–5433, 2011. doi:10.1016/j.actamat.2011.05.015.

[14] S. Frank, U. A. Handge, S. Olliges, and R. Spolenak. *Acta Mater*, 57(5):1442–1453, 2009. doi:10.1016/j.actamat.2008.11.023.

[15] H. Cox. *British Journal of Applied Physics*, 3(3):72–79, 1952. doi:10.1088/0508-3443/3/3/302.

[16] C. Hsueh and M. Yanaka. *J Mater Sci*, 38(8):1809–1817, 2003. doi:10.1023/A:1023200415364.

D

Experimental Characterization and Modelling of Triaxial Residual Stresses in Straightened Railway Rails

Robert Kaiser[a], Mario Stefenelli[b], Thomas Hatzenbichler[a], Thomas Antretter[d], Michael Hofmann[e], Jozef Keckes[c], Bruno Buchmayr[a]

[a]Chair of Metal Forming, Montanuniversität Leoben, Austria
[b]Materials Center Leoben Forschung GmbH, Leoben, Austria
[c]Chair of Materials Physics, Montanuniversität Leoben, Austria
[d]Institute of Mechanics, Montanuniversität Leoben, Austria
[e]FRM II, TU München, Garching, Germany

Abstract

Residual stresses in railway rails have a significant influence on the rail functional properties and reliability in service life. Already during the production, the roller straightening as the final production step removing the rail curvature causes the formation of complex stress fields. In this work, a complementary experimental characterization of longitudinal, transversal and normal residual stresses in an uncut

straightened rail with a length of 0.5 m is performed using neutron diffraction and a newly developed extended-contour method. Additionally, the residual stresses are validated numerically by means of an extensive three-dimensional finite element simulation taking into account the cyclic elastic-plastic material behaviour of the rail including combined kinematic-isotropic hardening. The very good agreement between the experimental and numerical data provides a basis for the understanding and predicting how the straightening procedure, i.e. the positioning of the individual rollers and forces applied by the rollers, influences the triaxial stress fields at the rail cross section.

D.1. Introduction

Roller straightening is the final step in the production of a railway rail. It follows the cooling to room temperature after the hot rolling performed at about 1000°C and results in the formation of a rail curvature and relatively small residual stresses [1–3] caused by the specific rail profile geometry and negligible mechanical constrains on the cooling bed. Since most of the rail mass is concentrated in the rails head the cooling is slower in the head than in the foot. The colder foot and the web exert a longitudinal force on the hot head which leads to a plastic deformation and consequently to a reduction of the rail´s length in the head zone. Upon continuing the cooling process the head cools down and the dimensional mismatch between the foot and the web results in a curvature of the rail whose neutral axis lies in the rail head.

In order to obtain a straight rail the cooling must be followed by a complex roller straightening process which is performed by alternating bending about the cold rails axes of inertia using a set of rollers (Fig. D.1). The roller pitch can be regular, like at the horizontal bending machine (HM), or irregular, at the vertical bending machine (VM). Since the straightening step is the final step in the production route, it has a significant influence on the final properties of the rail. As a consequence the rail should not only be straight but residual stresses should be minimal after this process [4]. According to a draft standard elaborated by European Committee for Standardization (CEN), the longitudinal residual stresses in the middle of the rail foot must not exceed 250 MPa [5].

In order to quantify residual stresses in rails numerous experimental and computational works have been performed in the past [3, 4, 6–21]. Pioneering studies appeared already in 1937 by Meier [3] where the typical C-shaped residual stress distribution for straightened rails characterized by sectioning methods was recog-

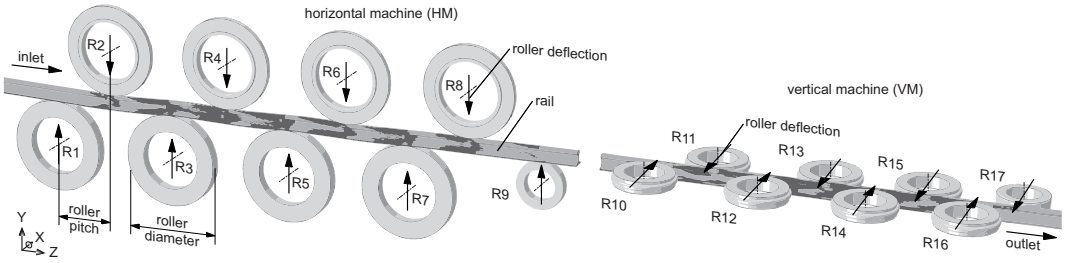

Figure D.1.: A schematic sketch of the straightening process performed by the horizontal (HM) and vertical (VM) machines. The arrows indicate deflection of selected rollers. The dark grey regions on the rail indicate the plastic deformation zone.

nized. More recent publications [6–11, 14–16, 22] were devoted to non-destructive volume-sensitive stress characterization using neutrons and synchrotron radiation. Sasaki et al. [10] used neutron diffraction to evaluate residual stresses in small sections of 10 mm of a rail head. Similar Jun et al. [11] performed neutron diffraction measurements on a 16 mm thick transverse slice through the entire profile of a rail which has been in service. In order to eliminate the effect of the sectioning, Luzin et al. [12, 22] characterized residual stresses in a 10 mm thick rail section and in a 0.5 m long rail. The results documented that the sectioning results in the significant modification of the original residual stresses in the rail where especially longitudinal stress components were affected.

Another approach to evaluate longitudinal residual stresses in rail long sections is the contour method proposed by Prime et al. [23–25]. The specimen is cut in two pieces normal to the profile axis, which leads to an elastic recovery of the longitudinal stresses. The stresses can be calculated from the relaxation strains by a variation of Bueckner´s superposition principle [26] or by finite-element modelling (FEM). Prime [23, 24] shows, based on the example of a bent beam specimen, that this method can measure a full 2D map of the residual stress component normal to the cross section. Knowing that the longitudinal residual stress is the most critical component for railway rails makes this method an interesting alternative even though only one stress component can be evaluated.

Residual stresses in railway rails have been characterized primarily in used rail sections in order to evaluate the influence of the service on the stress development [7, 8, 11, 12, 15, 16]. The experimental stress characterization in “as-produced” rails with preserved longitudinal components, i.e. in an unsectioned rail, has not been performed yet. There have been however a few approaches to determine the stress state in straightened rails using FEM. One approach is based on the classical Euler-

Bernoulli assumptions for bending in combination of the theory of Hertz to model the stress evolution in the rails cross-sections during straightening influenced by the roller contact [17, 18]. In other models, 2D or 3D modelled sections of the rail are driven by boundary conditions calculated from the bending line analytically or by a beam model. In that case, the influence of the contact situation was also modelled supposing elastic or rigid rollers [4, 19, 20, 27, 28].

The objectives of this work are (i) to perform an experimental characterization of residual stresses in an uncut straightened rail (with unrelaxed longitudinal residual stresses) using neutron diffraction and the contour method and (ii) to correlate the results with a finite element simulation of the straightening process. Finally, the combination of experimental and numerical approaches allows (i) a validation of the model and (ii) finally also the understanding and the optimization of the straightening procedure. Methodologically, the approach should also evaluate the advantages and disadvantages of stress characterization using neutrons and the contour method in large engineering components.

D.2. Experimental

D.2.1. Neutron Diffraction Characterization

Residual stress characterization was performed in a straightened 0.5 m long rail with the preserved original stress state at the Stress-Spec neutron diffractometer [29] of the FRMII facility in Garching, Germany. For the measurements a neutron wavelength of 1.664 Å and a gauge volume of $5 \times 5 \times 5$ mm3 were used. The gauge volume was defined by a slit in the incoming beam and a radial collimator before the detector to leave enough space for the large sample. The reason for the relatively large gauge volume was the low neutron transmission of about 1–2% for points in the head, that resulted in low diffraction statistics and long coating times of up to 2 hours per one acquisition [22]. The diffraction signal was recorded using a two dimensional detector with an active area of 300×300 mm2 and a pixel size of about 1.4 mm.

For the position-resolved characterization of diffraction elastic strains $\varepsilon_i^{hkl}(x, y, z)$ in the rail at the positions (x, y, z), α-Fe hkl reflections 211 or 110 were scanned with diffraction vectors oriented parallel to the transverse, normal and longitudinal rail axes. The 110 reflections were used to measure the points in the head, as the lower Bragg angle of 48° and additional tilting of the sample would allow shorter pathways. Most of the measurement points were located along the rail vertical

symmetry axis. The measured diffraction angles were used to calculate the lattice spacing $d_i^{hkl}(x,y,z)$ using Bragg's law. The unstressed lattice parameters d_0^{hkl} were determined experimentally by measuring $4 \times 4 \times 4\,\mathrm{mm3}$ steel cubes extracted from the rail. The diffraction elastic strain in three directions was determined according to

$$\varepsilon_i^{hkl}(x,y,z) = \frac{d_i^{hkl}(x,y,z) - d_0^{hkl}(x,y,z)}{d_0^{hkl}(x,y,z)} \tag{D.1}$$

where i represents transverse (x), normal (y) and longitudinal (z) orientations of the diffraction vector. The triaxial residual stresses at the positions (x,y,z) were determined using

$$\begin{aligned} \sigma_i(x,y,z) &= \frac{E^{hkl}}{(1+\nu^{hkl})}\left(\varepsilon_i^{hkl}(x,y,z) + \frac{\nu^{hkl}}{(1-2\nu^{hkl})}\sum_j \varepsilon_j^{hkl}(x,y,z)\right) \\ &\text{with} \quad j = x,y,z \end{aligned} \tag{D.2}$$

where a Young's modulus of $E^{hkl} = 216\,\mathrm{GPa}$ and a Poisson's ratio of $\nu^{hkl} = 0.286$ were used for both reflections [30].

D.2.2. Contour Method

The contour method [23, 24, 31] was applied to characterise residual stresses in an as-produced roller straightened rail, having a length of 0.5 m. The cut was carried out by a conventional industrial wire electric discharge machining (WEDM) machine approximately in the rail centre and perpendicular to the rail longitudinal axis. After the cutting both cutting surfaces were scanned using a coordinate measuring machine (CMM), applying a grid of $1 \times 1\,\mathrm{mm2}$. In order to obtain accurate results the measured contour was corrected to compensate errors from the cutting process. According to [31] there are anti-symmetric and symmetric errors. The first group derives from the effects such as shifting of the parts due to bad clamping or a crooked cut, and can be corrected by averaging the contours of both cutting surfaces. The latter group comprises local variations in the cutting surfaces due to the cutting itself, such as changes in the cut width [32–34]. These errors can be corrected by subtracting the contour obtained from a stress free reference [31, 35].

To determine the unknown two dimensional (2D) residual stress distribution across the as-produced rail from the known measured and corrected 2D contour data, an elastic finite-element model (FEM) was used applying Young's modulus $E =$

205 GPa and the Poisson´s ratio $\nu = 0.3$. In the model, numerical contour data equivalent to those from the experiment were generated on a 0.25 m long rail segment and then the curved rail cross-section was displaced to the plane state. The 2D stress generated in the rail using the later step was considered as the searched residual stress in the uncut as-produced rail.

D.2.3. FEM analysis of the Straightening Process

The roller straightening process of the rail was modelled with FEM using ABAQUS/Standard [36]. For the cyclic elastic-plastic material behaviour of the rail steel, the already implemented Chaboche model was used [36–38].

To reduce the numbers of elements in the 3D model of the straightening process a sub-modelling technique was used. This entails performing the numerical analysis in two steps: (i) a global analysis, where a simple beam element model of the rail is generated and pulled through the roller straightener and where the history of the displacements and rotations of each node is monitored, (ii) the subsequent submodel analysis, where a designated section of interest is finely meshed using 3D solid elements whose bounding plane positions are subjected to the nodal displacement and rotation history calculated in the global analysis.

To prevent shear locking of the elements during bending the three dimensional solid eight node linear brick element with reduced integration (C3D8R) were used. The rollers were modelled as rigid. For the contact model Coulomb friction ($\mu = 0.15$) was assumed. The compliance of the roller surface was accounted for by a so-called “softened” contact relationship. For this purpose the pressure-overclosure relationship was defined by the contact stiffness derived from the Hertz theory [39, 40]. The calculation time for the 170,000 elements containing submodel was about 240 hours on 12 processors.

D.3. Results and Discussion

D.3.1. Contour Data

The characterization of the two dimensional distribution of the longitudinal stresses across the annealed rail with a grid of $1 \times 1\,\mathrm{mm}2$ was performed using the contour method. In Fig. D.2, the experimental data obtained from a coordinate measuring machine are presented. The displacement values in the range from -0.045 to 0.035 mm indicate the presence of compressive and tensile stresses at the rail cross-section.

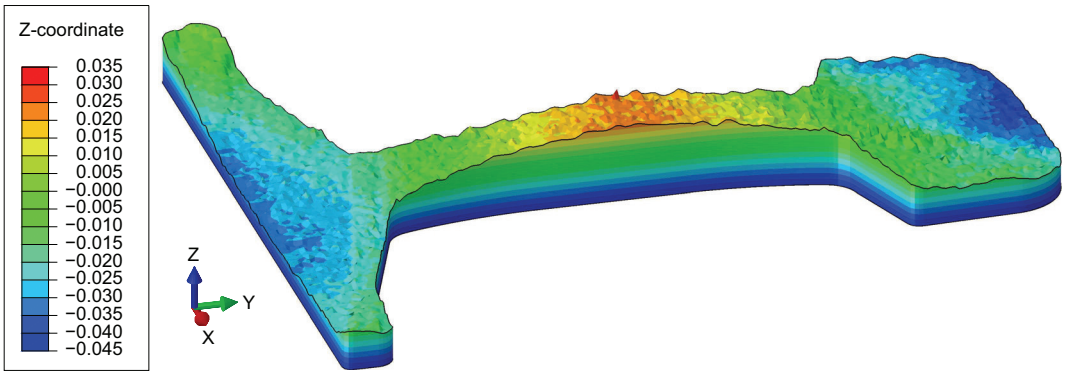

Figure D.2.: Displacement data in mm obtained using the contour method indicate the local material relaxation across the rail cross-section after the cutting. Positive and negative values correspond to compressive and tensile longitudinal stresses.

The contour data from Fig. D.2 were used to evaluate longitudinal stresses using the FEM model (*cf.* Sec. D.2.2). The results in Fig. D.3 indicate the presence of a C-like longitudinal stress profile across the rail cross-section with about 160 and 130 MPa at the foot and head, respectively, and −125 MPa in the web. The tensile stresses obtained from the contour approach are significantly smaller than the strength of the material and lie obviously also within the limit defined by the CEN draft standard of 250 MPa. The measurement errors of the contour method are about ±15 %.

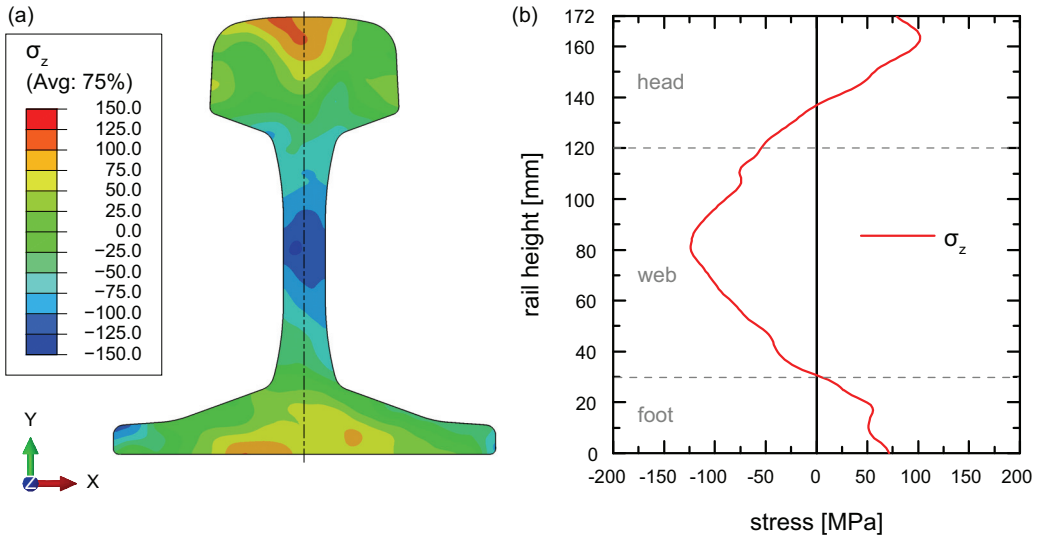

Figure D.3.: 2D distribution of longitudinal residual stresses σ_z across the straightened rail (a) determined by means of the contour method and the stress profile across the rail vertical axis (b).

D.3.2. Neutron Residual Stress Characterization

Neutron diffraction allows characterizing all three stress components in the rail. Due to the long pathways in the material and the resulting long measurement times, the triaxial stresses were determined only in selected volume elements with the size of $5 \times 5 \times 5\,\mathrm{mm}3$. Longitudinal residual stresses for selected probe positions are presented in Fig. D.4.

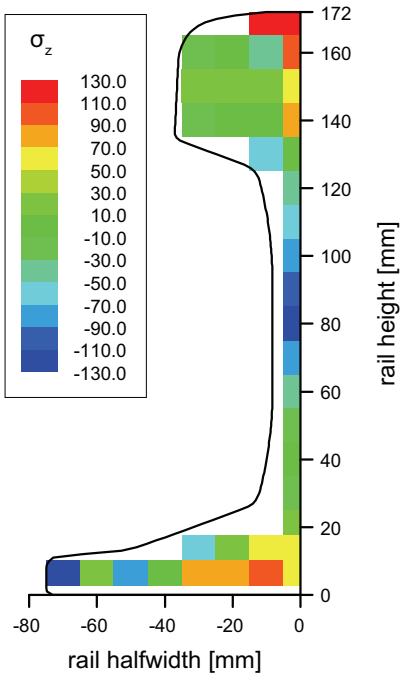

Figure D.4.: Longitudinal residual stresses in MPa across the straightened rail determined using neutron diffraction.

Additionally, triaxial residual stresses along the rail symmetry axis are shown in Fig. D.5.

Also in the case of neutron characterization, longitudinal tensile stresses of 160 and 130 MPa were observed in the foot and head whereas a stress of −125 MPa was determined in the web centre. The magnitudes of the stresses determined in the head are comparable with the results of Jun et al. [11] where actually stress reconstruction from measurements on thin rail slices was used. The relatively large measurement errors from about 20 MPa in the web centre to about 80 MPa in the rail head were caused especially by the long pathways of the neutrons which resulted in relatively weak diffraction statistics. The last measurement points in the foot (at 3 mm) and in the head (at 170 mm) show an abrupt change in stress, which also

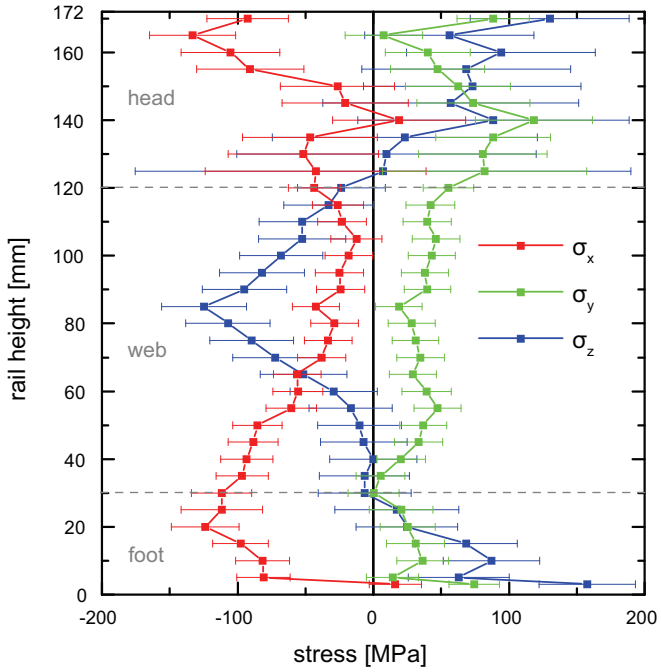

Figure D.5.: Distribution of triaxial stresses in the straightened rail across the rail symmetry vertical axis determined by neutron diffraction.

violates the boundary condition of σ_y being zero at the surface. These stresses can be considered artefacts due to surface effects, as at these points the gauge volume was not full immersed into the material [41].

D.3.3. FEM Modelling

The FEM model was used to determine the distribution of triaxial stresses at the rail cross-section after the straightening (Fig. D.6). The results indicate again a C-like shape of the longitudinal stresses (Fig. D.6 c,d) with the stress profile varying in the range of about -75 to 100 MPa. The medium transversal and normal compressive stresses of about -60 MPa in the rail head near the surface were formed during an unloading of the rollers after the roller contact was removed. The region of transversal tensile stresses in the head is caused by the higher compressive deformation by the rollers of the VM in contrast to the lateral region (Fig. D.6 a). The same effect, however in normal direction is caused by the upper role of the HM (Fig. D.6 b).

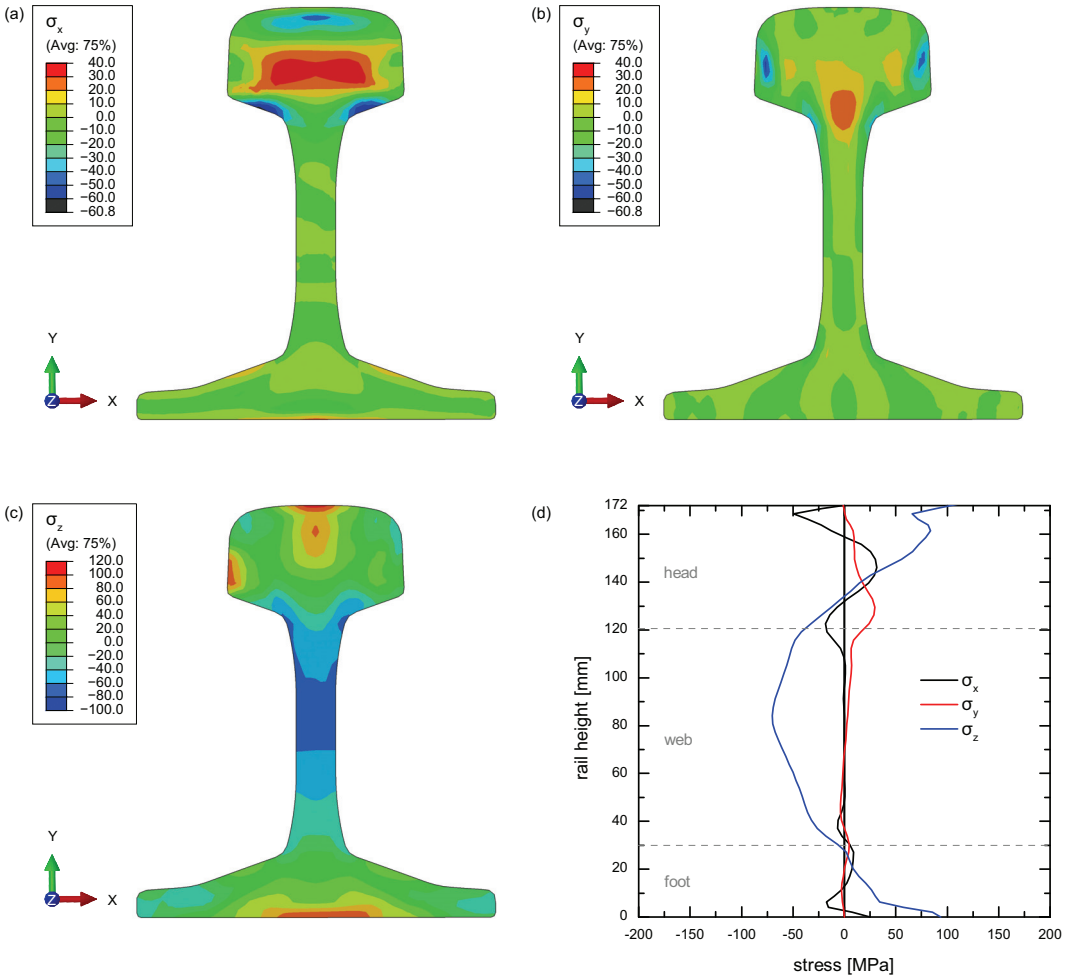

Figure D.6.: Spatial distribution of transversal σ_x (a), normal σ_y (b) and longitudinal σ_z (c) stresses across the rail cross-section, as obtained from the FEM model. Distribution of triaxial stresses along the rail symmetry axis is in (d).

The C-profile can easily be interpreted by analysing the individual modelling steps of the straightening process. During the first rail bending under the roll number R2 (*cf.* Fig. D.1) longitudinal compressive stresses form in the head and tensile stresses in the foot large enough that plastification occurs leaving residual stresses with an opposite sign after unloading between R2 and R3. This means that before entering R3 the head is exposed to tensile and the foot to compressive residual stresses. Bending about R3 basically reverses the situation, however to a lesser extent as the positioning of the rolls is chosen in such a way that the rail's curvature radii decay as the rail progresses towards the end of the roller straightener. At this point it is important to note the intricate contact situation between the roll and the rail introduces a significant amount of plasticity in the outer fibre of the rail that can

only be accommodated by a widening of the rail (i.e. a material flow in x-direction, cf. Fig. D.1) due to the kinematic constraints in the other directions. The Poisson effect then generates tensile stresses in z-direction that add to the stresses due to bending. This is repeated every time the rail is bent upwards or downwards. These additional tensile stresses are equilibrated by compressive stresses in the web of the rail giving rise to the characteristic C-shaped longitudinal stress distribution that is commonly observed in roller-straightened beams. Speaking in terms of strains this phenomenon can also be explained by a steady reduction of the beam length with every bending. This reduction can actually be measured amounting to about 100 mm for a 60 m rail after leaving the roller straightener. The formation of the C-profile is an inevitable consequence of the additional plasticity underneath the rolls and hence the entire straightening process. Changing process parameters will only shift or flatten this C-shaped stress distribution. The finite element model offers a cost-effective method to adjust the process parameters such as to minimize the magnitudes of the tensile stresses at the head and at the foot.

D.3.4. Results Comparison

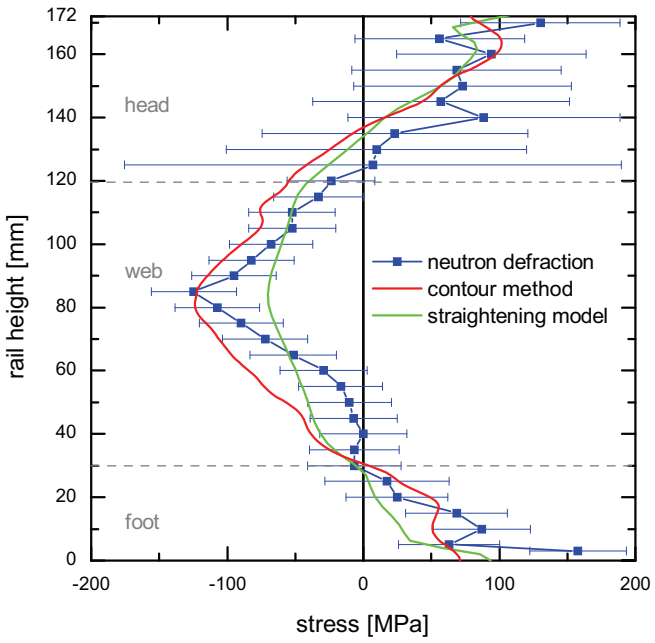

Figure D.7.: Comparison of the longitudinal residual stress σ_z distribution along the vertical symmetry axis evaluated by the contour method, neutron diffraction and FEM approach.

One of the main objectives of this work was to analyse longitudinal residual

stresses in the as-produced straightened rail. The longitudinal residual stress from the contour method, neutron diffraction and FEM approach are presented in Fig. D.7. As already documented in Sections D.3.1–D.3.4, the stress distributions exhibit always a C-like profile which was confirmed by all three methods. Though the magnitudes of the stress dependencies differ by about 50 MPa, the common trend of compressive stresses in the web and tensile stresses in the head and foot is obvious.

D.4. Discussion

The combination of two experimental techniques and the FEM modelling procedure demonstrated that all three approaches provide qualitatively the same profile of the longitudinal stresses across the rail vertical axis with a typical "C" shape. The tensile longitudinal residual stresses in Fig. D.7 are significantly smaller than the strength of the material and lie obviously also within the limit defined by the CEN draft standard of 250 MPa. The aim of this paragraph is to discuss the individual approaches.

The contour method provided representative data on the longitudinal stresses which agree very well with the values obtained from other techniques (Fig. D.7). The whole procedure including sample preparation, surface mapping and data processing takes about 20 hours. The main advantages of the technique are the relatively cost-effectiveness and the fact that the method provides 2D distribution of the stresses across the rail cross-section with a mesh of 1×1 mm (Fig. D.2). As drawbacks, one should mention that a contour of a stress-free reference must be measured additionally in order to correct for measurement errors and a linear elastic 3D finite element model must be built in order to reconstruct the residual stress fields from the measurement displacement fields.

In the case of neutron characterization, the measurements can be performed on an as-delivered rail of 0.5 m in length without the need of cutting. Due to the long pathways resulting in a bad diffraction statistics and acquisition times up to 2 hours a relatively large probing volume of $5 \times 5 \times 5$ mm3 was used. This allowed to reduce the measurement time to as low as 3 days. This demonstrates that this type of analysis is restricted to dedicated samples only, because it is expensive and must be planned in advance. Similar as in the case of contour method, also for the neutron characterization stress free samples must be provided in order to determine unstressed lattice parameters of the crystal. The rail length of 0.5 m proved to be long enough in order to preserve the longitudinal stress components.

The FEM analysis provided very detailed data on the stress distribution across

the rail. The predictive quality of such an approach relies however on the accuracy of the material model which has to be able to account for cyclic plasticity including the hardening mechanisms that are relevant within the first loading cycles. Determining the pertaining material parameters requires cyclic tension-compression tests at strain amplitudes similar to the actual straightening process. Particular attention has also to be paid to the details of the contact between the rail and the roll as this has a significant influence on the stress situation especially in the outer fibres. Once a reliable model is set up sufficiently large computational resources must be provided. In the present case the two-step simulation (global model and submodel) of the process took two weeks on 12 standard x86 3 GHz cores. The main advantage of the FEM approach is naturally the fact that once the numerical method has been validated against the experimental evidence it may unfold its strength by providing full versatility with respect to parameter variations, such as different roller positions or forces applied by the individual rollers.

D.5. Conclusion

The longitudinal residual stress distribution across the vertical axis of the straightened rail was characterized using neutron diffraction, the contour method and a FEM model. All three approaches delivered the same stress profile with a typical "C" shape and the maximal tensile stresses below the limit of 250 MPa defined by the CEN draft standard. Methodologically, the work demonstrates that all three approaches provide actually equivalent results which were however achieved using absolutely different procedures and also under very different costs.

The validation and adjustment of the FEM approach with the experimental data represents an important step in understanding and control of the straightening process. The development of the FEM approach opens the way to produce rails with well-adjusted residual stress fields by varying roller positions or forces applied by the individual rollers.

D.6. Acknowledgement

Financial support by the Austrian Federal Government (in particular from Bundesministerium für Verkehr, Innovation und Technologie and Bundesministerium für Wissenschaft, Forschung und Wirtschaft) represented by Österreichische Forschungsförderungsgesellschaft mbH and the Styrian and the Tyrolean Provincial Government, represented by Steirische Wirtschaftsförderungsgesellschaft mbH and Standortagen-

tur Tirol, within the framework of the COMET Funding Programme is gratefully acknowledged.

This research project has been supported by the European Commission under the 7th Framework Programme through the "Research Infrastructures" action of the "Capacities" Programme, Contract No: CP-CSA_INFRA-2008-1.1.1 Number 226507-NMI3.

Bibliography to paper D

[1] E. Hinteregger. *Eigenspannungen und Verformungen in Schienen nach dem Walzen vor dem Richten*. PhD thesis, Montanuniversität Leoben, Österreich, 1990.

[2] E. Hinteregger, F. D. Fischer, F. G. Rammerstorfer, and A. Jöller. *BHM. Berg-Hüttenmänn. Monatsh.*, 135(11):437–442, 1990.

[3] H. Meier. *Z Ver Dtsch Ing*, 81(12):362–363, 1937.

[4] G. Schleinzer and F. D. Fischer. *Mat Sci Eng A*, 288(2):280–283, 2000. doi:10.1016/S0921-5093(00)00872-8.

[5] Bahnanwendungen – Oberbau - Schienen – teil 1: Vignolschienen ab 46 kg/m; Deutsche Fassung EN 13674-1:2003+a1:2007. Standard, 2008.

[6] O. H. F. H. Hirao, M. *Res Nondestruct Eval*, 5(3):211–223, 1994. doi:10.1007/BF01606409.

[7] P. Webster, D. Hughes, G. Mills, and G. Vaughan. *Mater Sci Forum*, 404 - 407: 767–772, 2002. doi:10.4028/www.scientific.net/MSF.404-407.767.

[8] D. J. Buttle, W. Dalzell, and P. J. Thayer. *Insight: Non-Destructive Testing and Condition Monitoring*, 44(6):364–368, 2002.

[9] J. Magiera. *Wear*, 253(1-2):228–240, 2002. doi:10.1016/S0043-1648(02)00106-0.

[10] T. Sasaki, S. Takahashi, Y. Kanematsu, Y. Satoh, K. Iwafuchi, M. Ishida, and Y. Morii. *Wear*, 265(9-10):1402–1407, 2008. doi:10.1016/j.wear.2008.04.047.

[11] T.-S. Jun, F. Hofmann, J. Belnoue, X. Song, M. Hofmann, and A. Korsunsky. *J Strain Anal Eng*, 44(7):563–568, 2009. doi:10.1243/03093247JSA545.

[12] V. Luzin, T. Gnaupel-Herold, J. E. Gordon, and H. J. Prask. In *Proceedings of IMECE 2004*, volume 28, pages 117–122, Anaheim, CA, 2004. ASME. doi:doi: 10.1115/IMECE2004-61754.

[13] P. Withers, M. Turski, L. Edwards, P. Bouchard, and D. Buttle. *Int J Pres Ves Pip*, 85(3):118–127, 2008. doi:10.1016/j.ijpvp.2007.10.007.

[14] G. Webster and A. Ezeilo. *Int J Fatigue*, 23(SUPPL. 1):375–383, 2001.

[15] J. Kelleher, M. B. Prime, P. M. Mummery, P. J. Webster, J. Shackleton, and P. J. Whiters. *J Neutron Res*, 11(4):187–193, 2003.

[16] J. F. Kelleher, D. J. Buttle, P. M. Mummery, and P. J. Withers. *Mater Sci Forum*, 490–491:165–170, 2005. doi:10.4028/www.scientific.net/MSF.490-491.165.

[17] W. Guericke. *Technische Mechanik*, 14(2):155–176, 1994.

[18] J. Weiser. *Analyse der Eigenspannungsentstehung beim Rollenrichten von Schienen*. PhD thesis, Otto-von-Guericke-Universität Magdeburg, Deutschland, 1997.

[19] G. Finstermann, F. D. Fischer, G. Shan, and G. Schleinzer. *Steel Res*, 69(7): 272–278, 1998.

[20] G. Schleinzer. *Residual stress formation during the roller straightening of rails*. PhD thesis, Montanuniversität Leoben, Österreich, 2000.

[21] G. Schleinzer and F. D. Fischer. *Int J Mech Sci*, 43(10):2281–2295, 2001. doi:10.1016/S0020-7403(01)00041-8.

[22] V. Luzin, H.-J. Prask, T. Gnaupel-Herold, J. Gordon, D. Wexler, C. Rathod, S. Pal, W. Daniel, and A. Atrens. *Neutron News*, 24(3):9–13, 2013. doi:10.1080/10448632.2013.804353.

[23] M. B. Prime. *American Society of Mechanical Engineers, Pressure Vessels and Piping Division (Publication) PVP*, 415:121–127, 2000.

[24] M. B. Prime. *J Eng Mater Tech*, 123(2):162–168, 2001. doi:10.1115/1.1345526.

[25] P. Pagliaro, M. Prime, H. Swenson, and B. Zuccarello. *Vdi Bericht*, 50:187–194, 2010. doi:10.1007/s11340-009-9280-3.

[26] H. Buenckner. *Trans ASME*, 80:1225–1230, 1958.

[27] B. E. Varney and T. N. Farris. In *39th Mechanical Working and Steel Processing Conference*, volume 35, pages 1111–1121, USA, 1998. Iron & Steel Society of AIME.

[28] C. Betegón Biempica, J. J. del Coz Díaz, P. J. García Nieto, and I. Peñuelas Sánchez. *Appl Math Model*, 33(1):34–53, 2009. doi:10.1016/j.apm.2007.10.015.

[29] M. Hofmann, R. Schneider, G. A. Seidl, J. Rebelo-Kornmeier, R. C. Wimpory, U. Garbe, and H.-G. Brokmeier. *Physica B*, 385–386(Part 2):1035–1037, 2006. doi:10.1016/j.physb.2006.05.331.

[30] S. A. Kim and W. L. Johnson. *Mat Sci Eng A*, 452–453(0):633–639, 2007. doi:10.1016/j.msea.2006.11.147.

[31] M. B. Prime and A. L. Kastengren. In T. Proulx, editor, *Experimental and Applied Mechanics, Volume 6*, Conference Proceedings of the Society for Experimental Mechanics Series, pages 233–250. Springer New York, 2011. doi:10.1007/978-1-4419-9792-0_40.

[32] N. Tosun, C. Cogun, and G. Tosun. *J Mater Process Tech*, 152(3):316–322, 2004. doi:10.1016/j.jmatprotec.2004.04.373.

[33] S. Di, X. Chu, D. Wei, Z. Wang, G. Chi, and Y. Liu. *International Journal of Machine Tools and Manufacture*, 49(10):788–792, 2009. doi:10.1016/j.ijmachtools.2009.04.006.

[34] A. Alias, B. Abdullah, and N. M. Abbas. *Procedia Engineering*, 41(0):1806–1811, 2012. doi:10.1016/j.proeng.2012.07.387.

[35] R. Kaiser. *Eigenspannungsoptimiertes Richten von Eisenbahnschienen*. PhD thesis, Montanuniversitaet Leoben, Austria, 2014. in press.

[36] *Abaqus 6.12 Documentation*. Dassault Systèmes Simulia Corp., Providence, RI, USA, 2012.

[37] J. L. Chaboche. *Int J Plasticity*, 5(3):247–302, 1989. doi:10.1016/0749-6419(89)90015-6.

[38] J. Lemaitre and J.-L. Chaboche. *Mechanics of solid materials*. Cambridge Univ. Press, 2000.

[39] R. Kaiser, T. Hatzenbichler, B. Buchmayr, and T. Antretter. *Mater Sci Forum*, 768–769:456–463, 2014. doi:10.4028/www.scientific.net/MSF.768-769.456.

[40] H. Hertz. *Journal für die reine und angewandte Mathematik*, 92:156–171, 1881.

[41] P. J. Webster, G. Mills, X. D. Wang, W. P. Kang, and T. M. Holden. *J Neutron Res*, 3(4):223–240, July 1996. doi:10.1080/10238169608200197.

E

Triaxial Residual Stresses in Thermomechanically Rolled Seamless Tubes Characterized by High-Energy Synchrotron X-ray Diffraction

Gerald Winter[a], Mario Stefenelli[b], Jürgen Klarner[a], Peter Staron[c], Torben Fischer[c], Jozef Keckes[d], Bruno Buchmayr[e]

[a]voestalpine Tubulars GmbH & Co KG, Department R&D, Kindberg, Austria

[b]Materials Center Leoben Forschung GmbH

[c]Helmholtz-Zentrum Geesthacht, Center for Materials and Coastal Research, Institute of Materials Research, Geesthacht, Germany

[d]Department Materials Physics, Montanuniversität Leoben and Erich Schmid Institute, Austrian Academy of Sciences, Leoben Austria

[e]Department Product Engineering, Chair of Metal Forming, Montanuniversität Leoben Austria

Abstract

Residual stresses in seamless steel tubes have a significant influence on the mechanical stability and reliability of industrial constructions. In this contribution, triaxial residual stresses in seamless rolled tubes with an outer diameter of 82 mm and a wall thickness of 9.8 mm were analysed at synchrotron source PETRA III at DESY in Hamburg using the HZG beamline HEMS (P07) with a photon energy of 75 keV. The position-resolved measurements were performed using a conical-slit measurement technique with a spatial resolution in the direction of the X-ray beam of 0.8 mm. The tubes were produced under dedicated thermal conditions resulting in complex microstructure and residual stress profiles across the tube walls. The (experimental) measurements allowed determining axial, tangential and radial residual stress profiles. The results reveal tensile stresses up to 150 MPa on the outer wall side and compressive stress of about −120 MPa on the inner wall side. The measurements document the importance of the cooling process control during the thermo-mechanical rolling, which represents a key factor for the design of dedicated microstructure and residual stress levels in the tubes.

E.1. Introduction

Non-destructive residual stress characterization in steel components at large penetration depths is a challenging task and can be nowadays performed using neutron diffraction and high-energy synchrotron X-ray diffraction [1]. The advantage of synchrotron X-rays with energies in the range of 50–300 keV is the high beam intensity enabling relatively fast measurements and in comparison with the neutron diffraction, better spatial resolution down to µm-range [2]. The possibility of fast measurements combined with a relatively small probe volume can be used for the characterization of large two and three-dimensional strain maps at depths down to a few cm.

The X-ray diffraction analysis of macroscopic residual stress fields is usually performed in two steps [3]. At first, lattice spacings $d^{hkl}(x, y, z)$ of hkl crystallographic planes are determined at different orientations of the diffraction vector Q and sample positions (x, y, z). Additionally, small pieces of the reference material (with relaxed macroscopic stresses) with the size of about $1 \times 1 \times 1\,\mathrm{mm}^3$ are measured using the same setup in order to determine unstressed lattice parameter d_0^{hkl} [3]. The X-ray elastic strain $\varepsilon^{hkl}(x, y, z)$ can then be evaluated according to

$$\varepsilon^{hkl}(x,y,z) = \frac{d^{hkl}(x,y,z) - d_0^{hkl}}{d_0^{hkl}} \tag{E.1}$$

As a second step, experimentally determined X-ray elastic strains $\varepsilon^{hkl}(x,y,z)$ are used to evaluate spatial distribution of triaxial residual stresses $\sigma_i(x,y,z)$ applying X-ray elastic constants E^{hkl} and ν^{hkl} of the material as follows [3]

$$\sigma_i(x,y,z) = \frac{E^{hkl}}{(1+\upsilon^{hkl})}\left(\varepsilon_i^{hkl}(x,y,z) + \frac{\upsilon^{hkl}}{(1-2\upsilon^{hkl})}\left(\varepsilon_A^{hkl} + \varepsilon_R^{hkl} + \varepsilon_T^{hkl}\right)\right) \tag{E.2}$$

Using the dedicated selection of the measurements directions, the stresses as well as the strains can be determined for radial (R), axial (A) and tangential (T) sample directions.

E^{hkl} and ν^{hkl} represent the elastic properties of the material and depend on the single crystal elastic constants of crystallites, crystallographic texture and grain interaction model.

The characterization of residual stress spatial distribution $\sigma_i(x,y,z)$ in bulk materials is still not trivial task, because the diffraction signal may originate from a relatively large sample volume. In the case of neutron diffraction, which works with the resolution down to $1 \times 1 \times 1\,\mathrm{mm}^3$, the gouge volume is usually defined by primary and secondary selection slits. In the case of X-ray diffraction analysis operating with smaller gauge volumes, the better spatial resolution can be achieved by using more advanced optical components. Recently, a conical slit cell (CSC) was proposed (Fig. E.1 a) to perform spatial resolved characterization of X-ray elastic strain in all directions $\varepsilon^{hkl}(x,y,z)$ [4]. The system is based on several concentric slits that are focused on a spot within the sample by their conical shape (Fig. E.1 b). The analysis of full diffraction rings enables the simultaneous determination of all strain components in the plane. Moreover, also basic information on the texture of the material can be obtained. To achieve depth resolutions well below 1.0 mm, the slit width as well as the beam cross-section has to be around 20 µm [4]; moreover, the depth resolution in x-direction also depends on the energy resolution given by the monochromator. Thus, a third-generation synchrotron source with high brilliance is required for the use of a CSC. So far, only few examples for the application of CSC for residual stress and texture analysis can be found in the literature [5]. A CSC produced by Institute für Mikromechanik Mainz is used for residual stress analysis at the HZG beamline HEMS at the PETRA III synchrotron source at DESY in Hamburg. While depth resolutions of a few 100 µm can be achieved with narrow

beams, the grain size of the studied material often prevents a conventional analysis of diffraction rings with such high resolutions; however, strategies for improving grain statistics can often be applied in such cases. In many cases, only moderate depth resolutions are required, and with a larger beam cross-section, the grain statistics can be improved.

In this contribution, spatial distribution of triaxial residual stresses across the wall of a thermo-mechanically treated seamless steel tube was characterized. The concept of thermo-mechanical treatment enables a control of microstructure in seamless steel tubes and allows the optimization of mechanical properties like high strength combined with excellent toughness and weldability. Conventional quenching and tempering in heating furnace and quenching device are substituted by the accelerated spray water cooling applied directly after the stretch reducing mill [6]. During the cooling, it is expected that complex residual stress and microstructure gradients connected with the formation of martensite are formed across the tube wall.

The aim of this work was to perform a position-resolved characterization of residual stresses across the walls of three tubes and evaluate the magnitude of radial, axial and tangential residual stress components in ferrite as a function of thermal treatment.

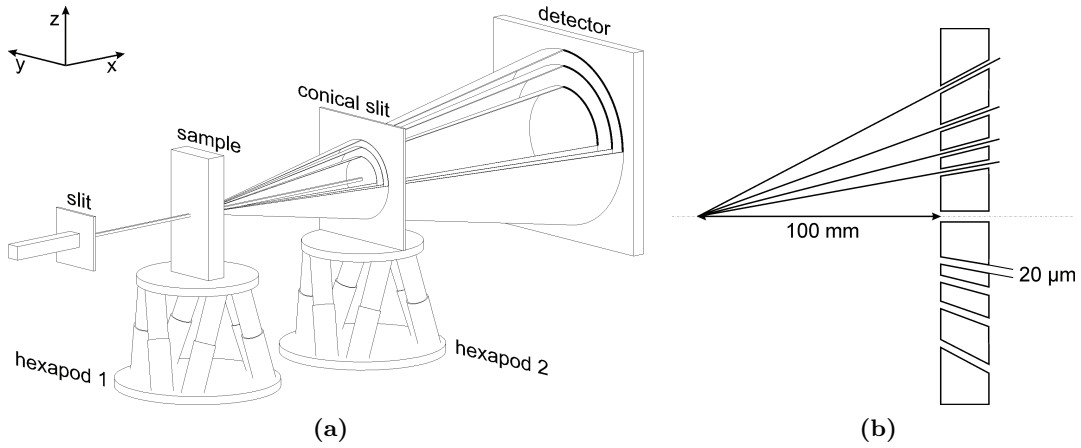

Figure E.1.: A schematic experimental setup using a conical slit cell which allows selecting a small sample volume (a) and a detail of the conical slit cell providing the spatial resolution of 0.8 mm (b).

E.2. Experiment

Thermo-mechanically treated seamless steel tubes are produced in a few steps. The piercing of a round solid billet is the first forming operation to make a seamless tube,

also known as the Mannesmann piercing procedure [7]. Two barrel-type rolls rotate in the same direction to feed the billet forward to the plug which is free to rotate. The rolling gap in the horizontal is closed by two Diescher discs. The push bench is the second forming device in the production for the elongation of the material using an internal tool. The mandrel bar pushes the pierced billet through several non-driven roller stands to produce the so-called pipe shell. In the reheating furnace the cold pipe shells get their required temperature for the last forming step the stretch-reducing mill. The heated pipe shells is stretched to achieve the final geometry by several driven roller stands. Directly after rolling, the tube surface is cooled down by spray water at high cooling rate to fix the ultrafine grained microstructure [8]. With respect to the achieved heat transfer and the tube cross-section, the tube consists of different microstructure layers. For high wall thickness tube surface section is martensitic followed by bainitic and ferritic/perlitic layer.

In this work, residual stresses in three types of seamless tubes were characterized. The tubes denoted further as A, B and C distinct by the cooling intensity and consequent microstructure gradient across their walls. Tube A was not water sprayed, tube B was moderately water sprayed and tube C was intensively cooled down after the stretch reducing mill. As a result of the different cooling rates, the tubes B and C exhibited an increased amount of martensite and bainite (Fig. E.2).

The A, B and C tubes were characterized at the HZG beamline HEMS (P07) at the PETRA III synchrotron source in Hamburg. For the experiment, the X-ray energy of 77.5 keV was used. The cross section of the X-ray beam was $50 \times 50\,\mu m$ and the depth resolution was about 0.8 mm. The grain size of the material was small enough to yield homogeneous diffraction rings with this gauge volume.

Strain measurements were carried out in two steps. At first the X-ray beam was oriented perpendicular to the tube axis and the tube wall was moved across the focus of the conical slits (Fig. E.1 b) in x-direction with a step of 0.5 mm. Simultaneously Debye-Scherrer rings were collected using the 2D detector. In the next step, the beam was directed parallel to the tube axis and rings cut from tubes (with a thickness of 15 mm) were scanned along the x-axis. At the end the unstressed lattice parameter was determined by scanning small pieces of the tube material.

From the first set of measurements, $d^{hkl}(x)$ dependence as a function of x and the angle δ (*cf.* Fig. E.3) was determined using the Bragg's law. Axial and tangential strain components $\varepsilon_A^{hkl}(x)$ and $\varepsilon_T^{hkl}(x)$ were quantified from $d^{hkl}(x)$ values (obtained for $\delta = 0$ and $\delta = 90$ degrees, respectively (Fig. E.3)) applying the unstressed lattice parameter d_o^{hkl} and Eq. (E.1). In a similar way tangential and radial strain components $\varepsilon_R^{hkl}(x)$ and $\varepsilon_T^{hkl}(x)$ were determined by analysing diffraction data in the

geometry with the X-ray beam oriented parallel to the tube axis.

Both X-ray elastic strains $\varepsilon_i^{hkl}(x)$ as well as residual stresses $\sigma_i(x)$ were determined with an error of 10 %.

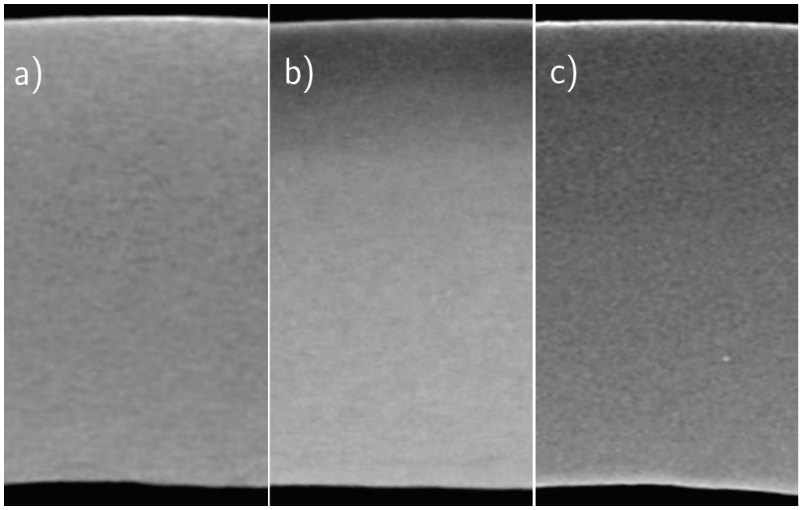

Figure E.2.: Microstructure (from outside to inside) across the tube walls A (a), B (b), C (c).

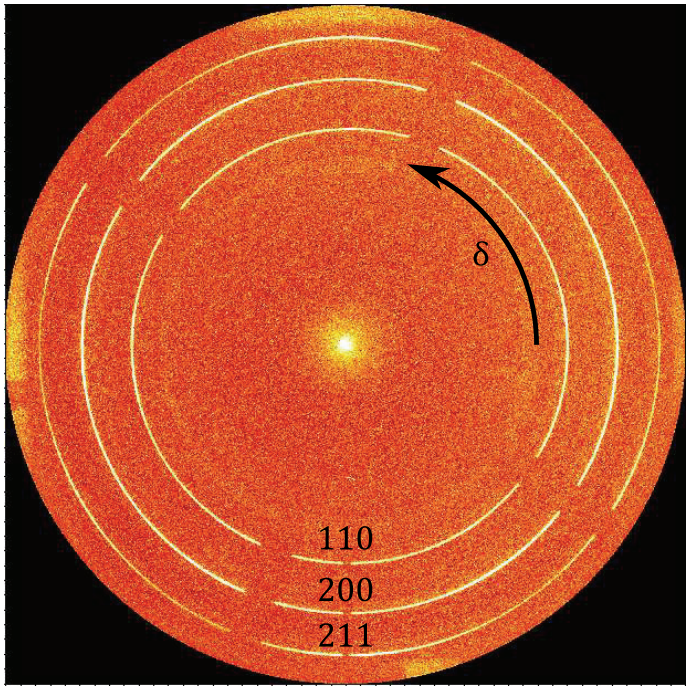

Figure E.3.: A representative X-ray diffraction pattern with ferrite 110, 200 and 211 Debye-Scherrer rings collected from a seamless steel tube using conical slits.

E.3. Results and Discussion

A representative X-ray diffraction pattern with typical Debye-Scherrer rings (collected from thermo-mechanically treated seamless steel tube B) is presented in Fig. E.3. One can identify 110, 200 and 211 diffraction rings originated from the ferrite phase. Similar patterns were collected from all three tubes and were used to evaluate distribution of X-ray strain $\varepsilon_i^{hkl}(x)$ across the walls.

In Fig. E.4, experimentally determined axial, tangential and radial X-ray elastic strain dependencies $\varepsilon_i^{hkl}(x)$ obtained from A, B and C tubes are presented. At this stage the results unambiguously demonstrate that the different cooling modes caused the formation of very specific strain profiles across the walls of A, B and C tubes.

The results from Fig. E.5 were used to quantify axial, tangential and radial residual stresses in ferrite using Eq. (E.2). Since the conical slits were aligned just for the ferrite reflections, the strains presented in Fig. E.4 represent the distortion in the ferrite crystallites and strains in the ferrite phase. The samples B and C differ in microstructure and phases because of different cooling intensity, the measured strains may differ from the tubes macroscopic strains. Due to above reasons, in order to evaluate stresses from the measured strains, ferrite X-ray elastic constants Young modulus of 225 GPa and Poisson number of 0.276 were applied for all three pipes. Similar as for strains, also in the case of residual stresses presented in Fig. E.5 very specific stress dependences $\sigma_i(x)$ can be observed.

In the tube A (produced without external cooling) one can observe relatively high axial, tangential and radial tensile stresses up to 120 MPa on both wall sides. This stress level may results in the limitation of the tube lifetime during cyclic mechanical loading because superimposed external stresses can promote the crack growth. In the wall centre low compressive stresses were detected.

In the tube B (produced using moderate water cooling), axial tensile stresses up to 150 MPa can be observed only on the outer wall side whereby the wall inner side is under compression.

In the tube C (produced using intensive water cooling), negligible residual stresses can be observed on the outer side and the inner side is under compression.

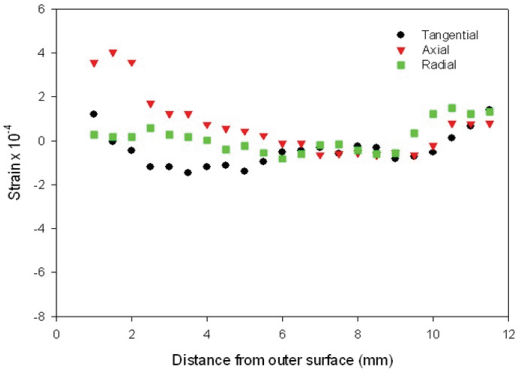

(a) Tube A

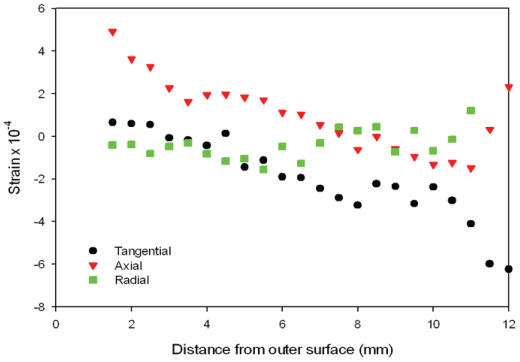

(b) Tube B

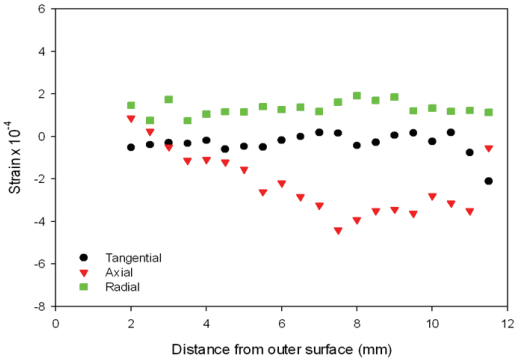

(c) Tube C

Figure E.4.: Distributions of axial, tangential and radial elastic strains (from outside to inside) across the walls of tube A (a), B (b), C (c).

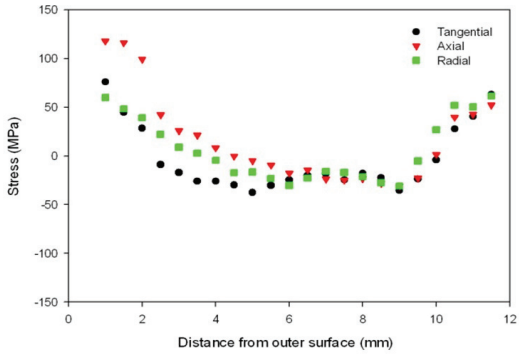

(a) Tube A

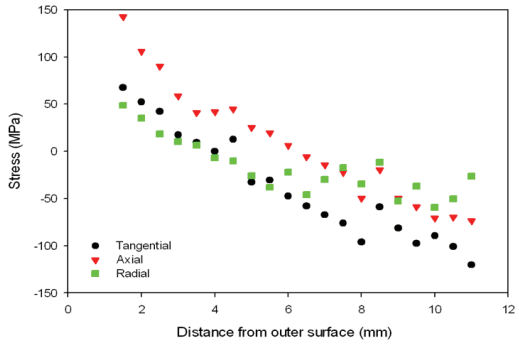

(b) Tube B

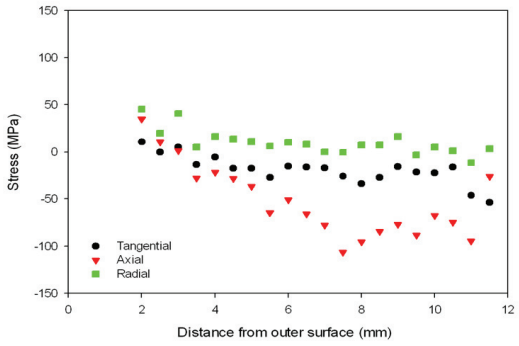

(c) Tube C

Figure E.5.: Distributions of axial, tangential and radial residual stresses (from outside to inside) across the walls of tube A (a), B (b), C (c).

E.4. Conclusions

Methodologically, the results document that conical slit cell can be effectively used to evaluate the magnitude of X-ray elastic strains and macroscopic residual stresses in steel tubes with a spatial resolution of 0.8 mm.

The residual stress data collected from A, B and C tubes (cooled under different conditions) document the importance of the cooling process control during the thermo-mechanical rolling of steel tubes. The tensile stresses detected in the outer wall side can represent a serious problem in the tube performance. By selecting dedicated cooling conditions, not only the microstructure but also residual stresses in the tubes can be tuned effectively.

E.5. Acknowledgements

Financial support by the Austrian Federal Government (in particular from the Bundesministerium für Verkehr, Innovation und Technologie and the Bundesministerium für Wirtschaft, Familie und Jugend) and the Styrian Provincial Government represented by Österreichische Forschungsförderungs-gesellschaft mbH and by Steirische Wirtschaftsförderungs-gesellschaft mbH, within the research activities of the K2 Competence Centre on "Integrated Research in Materials, Processing and Product Engineering" operated by the Materials Center Leoben Forschung GmbH in the framework of the Austrian COMET Competence Centre Programme, is gratefully acknowledged.

This project was supported by "Die Österreichische Forschungsförderungsgesellschaft" FFG Basisprogram and project "2655990 UHSTMRT". Portions of this research were carried out at the HZG beamline HEMS (P07) at the PETRA III synchrotron source at DESY in Hamburg, a member of the Helmholtz Association (HGF). We would like to thank Dr. Norbert Schell for assistance at the HZG beamline HEMS. We thank also to EU for the financial support to perform the experiment at DESY.

Bibliography to paper E

[1] M. Fitzpatrick and A. Lodini. *Analysis of Residual Stress by Diffraction Using Neutron and Synchrotron Radiation*. Taylor and Francis, London and New York, 2003.

[2] A. Pyzalla. *J Nondestruct Eval*, 19:21–32, 2000. doi:10.1023/A:1006664007726.

[3] I. C. Noyan and J. B. Cohen. *Measurement by Diffraction and Interpretation*. Springer, 1987.

[4] H. Poulsen, S. Garbe, T. Lorentzen, D. Jensen, F. Poulsen, N. Andersen, T. Frello, R. Feidenhans'l, and H. Graafsma. *J Synchrotron Radiat*, 4(3):147–154, 1997. doi:10.1107/S0909049597002021.

[5] R. Martins, U. Lienert, L. Margulies, and A. Pyzalla. *Mat Sci Eng A*, 402(1-2): 278–287, 2005. doi:10.1016/j.msea.2005.04.005.

[6] J. Klarner, B. Buchmayr, and W. Rainer. *BHM*, 156(5):168–174, 2011. doi:10.1007/s00501-011-0638-3.

[7] R. Pschera, J. Klarner, and C. Sommitsch. In *Proceedings Seminar Rohrherstellung und -verarbeitung*, pages 59–69, Leoben/Austria, 2007.

[8] B. Buchmayr and J. Klarner. *Aachener Stahlkolloquium*, 28, 2013.